The Dissertation Committee for Nedra Danielle Bonal Certifies that this is the approved version of the following dissertation:

Field Experiments for Fracture Characterization: Studies of Seismic Anisotropy and Tracer Imaging with GPR

Committee:

Clark R. Wilson, Supervisor

John M. Sharp, Jr.

Robert H. Tatham

Jeffrey G. Paine

Kenneth H. Stokoe, II

Field Experiments for Fracture Characterization: Studies of Seismic Anisotropy and Tracer Imaging with GPR

by

Nedra Danielle Bonal, B.S.

Dissertation

Presented to the Faculty of the Graduate School of

The University of Texas at Austin

in Partial Fulfillment

of the Requirements

for the Degree of

Doctor of Philosophy

The University of Texas at Austin

December, 2007

Dedication

This work is dedicated to my Papaw, Gerald Truman Alexander.

Acknowledgements

I would like to thank God for being all that I need. I appreciate my committee members, Clark Wilson, Jack Sharp, Robert Tatham, Jeffrey Paine, and Kenneth Stokoe for their valuable insight and effective suggestions for this work. Special thanks to my supervisor, Clark Wilson, for his assistance, especially these last few months and to Jack Sharp for his constant support. I would also like to thank my family for their love and support through all my journeys. I am especially grateful for my husband, David, for his continuous encouragement and devotion.

I would like to thank the Society of Exploration Geophysicists Foundation and the Jackson School of Geosciences Foundation for financial support of this research. The Vibroseis source and related recording equipment are part of the NEES@UTexas facility sponsored by the National Science Foundation, award number CMS-0086605. The survey at Stoneledge Quarry was one of the field trials of this equipment during the development portion of the NEES equipment grant. The support of the National Science Foundation is gratefully acknowledged. I am also grateful to The City of Austin for allowing me to use Stoneledge Quarry to collect the seismic data used in this research.

I would like to thank David Bonal for field assistance with the sledgehammer source and Christopher Stanton for field assistance using the Vibroseis source during acquisition of the seismic data. Special thanks to Terence T. Garner for multidisciplinary collaboration on the GPR experiment. Thanks to David Bonal, Susan Garner, Nicole

Pratt, Frank Roberts, Wendy Robertson, Don Slottke, and Brad Wolaver for field during acquisition of the GPR and tracer test data.

Field Experiments for Fracture Characterization: Studies of Seismic Anisotropy and Tracer Imaging with GPR

Publication No._____

Nedra Danielle Bonal, Ph.D.

The University of Texas at Austin, 2007

Supervisor: Clark R. Wilson

Knowledge of fracture orientation and density is significant for reservoir and aquifer characterization. In this study, field experiments are designed to estimate fracture parameters in situ from seismic and GPR (radar) data. The seismic experiment estimates parameters of orientation, density, and filling material. The GPR experiment estimates channel flow geometry and aperture.

In the seismic study, lines of 2D data are acquired in a vertically fractured limestone at three different azimuths to look for differences in seismic velocities. A sledgehammer, vertical source and a multicomponent, Vibroseis source are used with multicomponent receivers. Acquisition parameters of frequency, receiver spacing and source-to-receiver offset are varied. The entire suite of seismic body waves and Rayleigh waves is analyzed to characterize the subsurface. Alford rotations are used to determine fracture orientation and demonstrate good results when geophone orientation is taken into account. Results indicate that seismic anisotropy is caused by regional faulting. Average

fracture density of less than 5% and water table depth estimates are consistent with field observations. Groundwater flow direction has been observed by others to cross the fault trend and is subparallel to a secondary fracture set. In this study, seismic anisotropy appears unrelated to this secondary fracture set. Vp/Vs and Poisson's ratio values indicate a dolomite lithology. Sledgehammer and Vibroseis data provide consistent results.

In the GPR experiment, reflection profiles are acquired through common-offset profiling perpendicular to the dominant flow direction. High frequency waves are used to delineate fluid flow paths through a subhorizontal fracture and observe tracer channeling. Channeling of flow is expected to control solute transport. Changes in radar signal are quantitatively associated with changes in fracture filling material from an innovative method using correlation coefficients. Mapping these changes throughout the survey area reveals the geometry of the flow path of each injected liquid. The tracer is found to be concentrated in the center of the survey area where fracture apertures are large. This demonstrates that spatial variations in concentration are controlled by fluid channel geometry.

Table of Contents

List of Tables

List of Figures

Chapter 1: Introduction

An understanding of fractured rock is central to development of natural resources including petroleum, geothermal fluids, and drinking water. Fractures are described by parameters that include orientation, volume density, filling material, channeling, aperture and asperity (roughness). These parameters are of interest in both reservoir characterization for hydrocarbon production and in subsurface pathway description for groundwater flow and contaminant migration studies. Measurements of these and other fracture properties in situ have been problematic (Sharp, 1993). This study employs two types of field experiments designed to estimate fracture parameters. One, using multicomponent seismic data, has the goal of observing the influence of fractures on seismic wave speeds (seismic anisotropy) and relating observed effects to fracture orientation, density, and filling material. The second study employs ground penetrating radar (GPR) data to provide direct images of fractures and details of their aperture and fluid flow geometry.

1.1 Seismic Anisotropy Experiment

A field study to gather multicomponent seismic data was conducted over the fractured Edwards limestone south of Austin, Texas within an abandoned quarry. Vertical fractures were observed as the dominant type and although three sets were present, the main set paralleled the regional Balcones fault. Outcrop observations provided information on average fracture density, which was estimated from apertures and spacing along scan lines on quarry walls and floor. A scan line is a linear trace along which fracture parameters are measured. The presence of an observable water table below the elevation of the seismic survey lines allows seismic anisotropy effects to be measured for both dry and water filled fractures. The experiment allows a direct comparison between

observations of fracture parameters and azimuthal changes in velocity of seismic waves predictable from published theories.

Investigations of anisotropy have been documented on scales of laboratory (Ass'ad et al., 1992; Cheadle et al., 1991; Nur and Simmons, 1969; Rai and Hanson, 1988; Rathore et al., 1994, Tatham et al., 1992; and Vernik and Liu 1997); petroleum reservoir (Davis and Lewis, 1990; Lewis et al., 1991; Li et al., 1993; Mueller, 1991; Potters et al., 1999; Shuck et al., 1996), and crust and upper mantle (Bamford, 1977; Gledhill, 1993a and 1993b; Graham and Crampin, 1993; Liu et al., 1993a; Rowlands et al., 1993; Vlahovic et al., 2002; Xiong et al., 1993; Yao and Xiong, 1993; and Yao et al., 1993). There have been few studies, however, of anisotropy in the near surface. In most published studies, borehole seismic measurements have been employed [vertical seismic profiling (VSP) or crosswell techniques] (Beaty and Schmitt, 2003; Beckham, 1996; Corrigan et al., 1986; Douma et al., 1990; Liu et al., 1993b; Lynn, 1991; Ohanian and Beckham, 1992; Pratt et al., 1993; and Winterstein and Paulsson, 1990). This study and at least one other study in the published literature (Bamford and Nunn, 1979) are distinguished by the use of surface measurements, where direct observation of fractures in outcrop can be compared with seismic estimates of fracture parameters.

Three seismic lines were surveyed at varying azimuths using both sledgehammer and Vibroseis sources and 3 component (3C) geophones (one vertical and two orthogonal horizontal orientations). The hammer is a vertical component source that was used to produce a suite of seismograms commonly called a 3C data set. Traditional seismic data usually have only vertical receiver (1C) information. The Vibroseis provides 3 source components (one vertical and two horizontal), yielding a full 9-component (9C) data set when three receiver components are acquired for each source orientation. In principle, 9C data should provide information on the entire suite of seismic waves, including shear

waves of differing polarizations. Each seismic wave samples different aspects of the medium and may contain different or redundant information about fracture anisotropy. In addition to estimating fracture parameters of orientation, density, and filling-fluid, one of the goals of the study is to determine whether additional information about fracture properties can be obtained from 3C and 9C observations.

Fracture density has been defined multiple ways in the literature. Krasny and Sharp (2007) quantify fracture density as "… the number of fractures per unit length (along a scan line), in a unit area, or in a unit volume of rocks." However, seismic waves give estimates of the bulk properties of the rock rather than individual fractures. In the seismic literature, fracture density is proportional to anisotropy, which is expressed as a percentage (Bakulin et al., 2000; Lewis et al., 1991; Lynn and Thomsen, 1990, and Thomsen 1986 and 1988). In this research, I am adopting the seismic terminology for fracture density estimated from seismic data.

1.2 TRACER IMAGING WITH GPR

Fluid flow in fractures was the focus of a second study using GPR. The study was conducted in a single exfoliation crack in fractured granite in the Llano district west of Austin, Texas. The goal was to estimate channeling during flow and variations in fracture aperture. Channeling is the routing of fluid flow within a fracture. These parameters are important for understanding subsurface fluid transport.

Two different concentrations of saline tracer were used to observe flow and solute channeling through a subhorizontal fracture using GPR. Multiple parallel lines of 2D GPR images of the survey area were taken before fluid was pumped into the fracture, during pumping of water, and during pumping of water with a saline tracer. Flow was maintained at steady state during collection of GPR data. Signal variations between "dry" and "wet" images were correlated with variations on adjacent lines to produce a 3D

image of flow channeling within the fracture and deduce information regarding fracture aperture. Other goals of the GPR study were to determine saline concentration variations and effects of aperture variation on radar signal. Flow channel geometry results were related to observations of channel locations outside the survey boundary. Channel geometry and tracer concentration estimates were correlated with samples of tracer concentrations in three of the observed channels. Physical measurements of fracture depth and aperture in boreholes were used to provide ground-truth in confirming GPR results.

1.3 DISSERTATION ORGANIZATION

The dissertation is organized into seven chapters which first address the seismic experiments and then the GPR study. Several appendices are used to summarize published theory or present details of data analysis methods. Chapter 2 covers a description of the field area for the seismic surveys and describes the survey parameters. The field description includes fracture measurements made using non-seismic methods. Chapter 3 describes anisotropy theory and how seismic wave propagation velocity anisotropy is used to determine fracture density. Previous research on anisotropy and theoretical models such as Hudson's (1980, 1981) model are presented. An explanation of the synthetic modeling program used in this research is also given. Chapter 4 presents the seismic data collected from the 3C sledgehammer source and the results of velocity anisotropy. Fracture orientation, density, filling material by depth to the water table, and lithology are estimated from the data. Chapter 5 presents the seismic data collected from the 9C Vibroseis source and the results of velocity anisotropy. Fracture parameters of orientation, density, filling material, and lithology are also estimated from these data and comparisons are made to the sledgehammer data. Chapter 6 covers the entire GPR experiment including field description, methods, and results. Chapter 7 summarizes the

conclusions of both studies concerning the scientific questions presented in this introduction.

Chapter 2: Description of Field Site and Seismic Surveys

2.1 Seismic Field Experiment Overview

Three lines of multicomponent seismic data were collected at different azimuths with both sledgehammer and Vibroseis sources at a limestone quarry site south of Austin, Texas. Source-to-receiver offsets ranged from 10 m to 495 m, frequencies were between 25 Hz and 200 Hz, with wavelengths in the range of 20 m to 320 m. This chapter gives an overview of geologic setting, physical properties, and seismic field experimental setup for both source types.

2.2 Field Setting and Observations

The field site was the abandoned Stoneledge Quarry, which is in the Edwards Group and located at the northern edge of Hays County. Hill and Vaughan (1896) describe the Edwards Group as Cretaceous and primarily composed of calcium carbonate limestone with some dolomite. The group is characterized by massive bedding, homogeneous texture, and vugs. Solution-enlarged fractures create well-connected conduits for groundwater flow, making the Edwards Group a major karst aquifer. Figure 2.1 is a map showing the quarry location marked with a red star. The quarry is within the recharge zone of the Barton Springs segment of the Edward's aquifer in the dolomitic member of the Edward's Group (Hauwert, personal communication, 2004). A photograph of the strata from the quarry floor is shown in Figure 2.2.

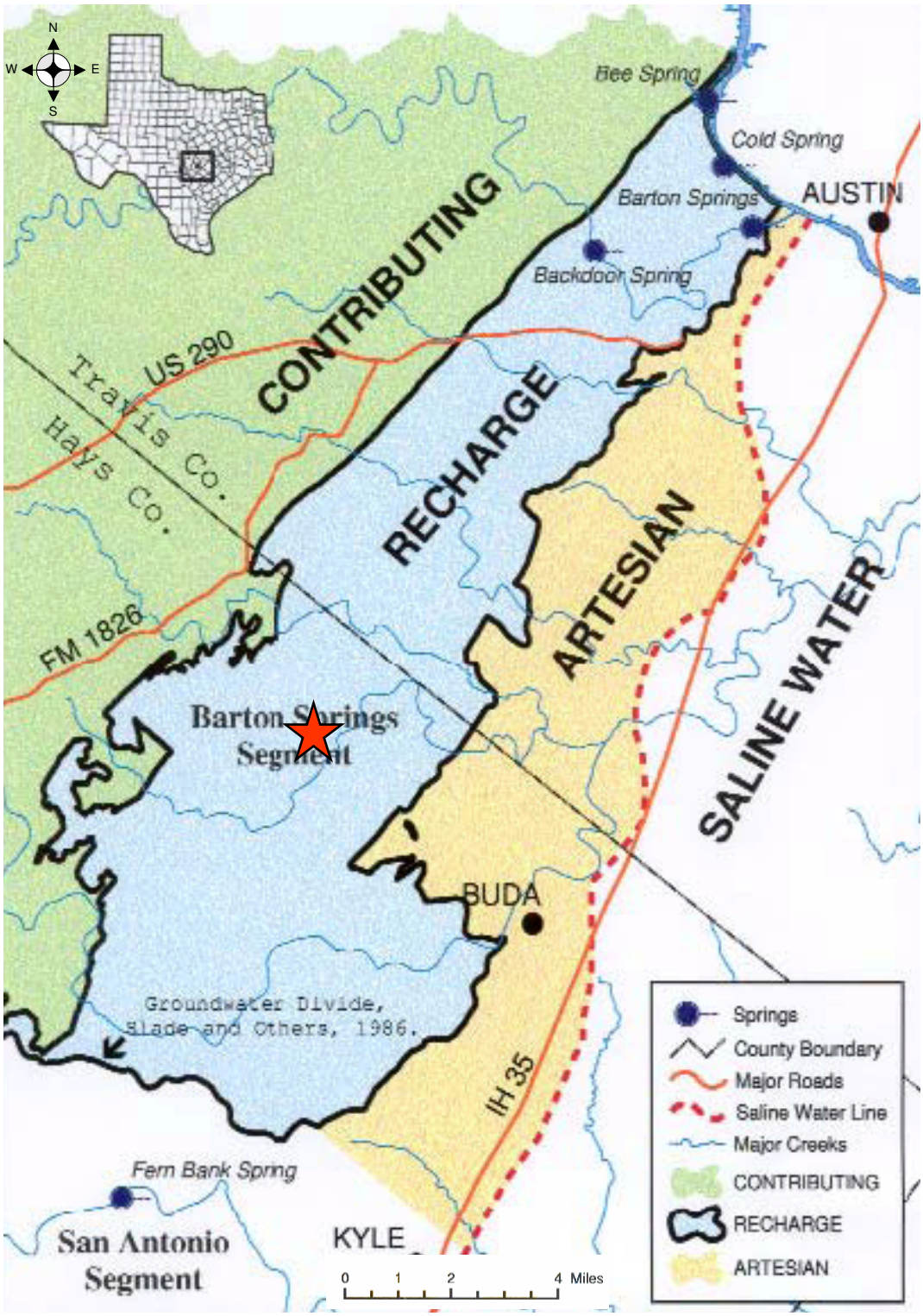

Figure 2.1 Map of Stoneledge Quarry located with a red star (from BSEACD, 2002).

Figure 2.2 Photograph of strata at Stoneledge Quarry. The person in this photograph is 1.8 m tall.

Fracturing and faulting near Stoneledge Quarry are described by Kolb (1981). The regional Balcones Fault trend at N35E is associated with Miocene tectonism. The major vertically dipping Mt. Bonnell Fault formed at this time trends at N40E and is located approximately 5 km from the site. I measured three fracture sets at Stoneledge Quarry. The majority of the measured fractures trend around N35E and are referred to as the primary set. The secondary set of fractures trend at N80E and the tertiary set trend at N4W. There is an apparent fault in the southeastern corner of the quarry trending northeast-southwest, aligned with the regional fault trend. Fracture dip for all sets was measured between 80° and 90° and is assumed vertical.

Previous hydrogeologic studies by the Barton Springs/Edwards Aquifer Conservation District (BSEACD, 2002) provided information about hydrologic properties of the subsurface, which may be related to fracture orientation. Dye tracer studies show that groundwater generally flows parallel to the regional fault orientation (N35E) in a northeasterly direction. However, at the Little Bear Creek injection site and at two other injection sites near Stoneledge Quarry, flow is easterly across the regional fault trend. Groundwater flow at these three areas are approximately parallel with the secondary fracture set (N80E) measured at Stoneledge Quarry. Dye tracing studies (BSEACD, 2002) show that groundwater from these three sites joins the primary flow system towards the northeast and exits the subsurface at Barton Springs (Figure 2.3). Fracture measurements (Appendix A) show that the primary set is dominant in outcrop, both in fracture aperture and number as shown in Figure 2.4 and Figure 2.5. The seismic measurements will determine whether seismic anisotropy is consistent with the primary set or perhaps affected by fractures that permit groundwater flow across the regional fault trend.

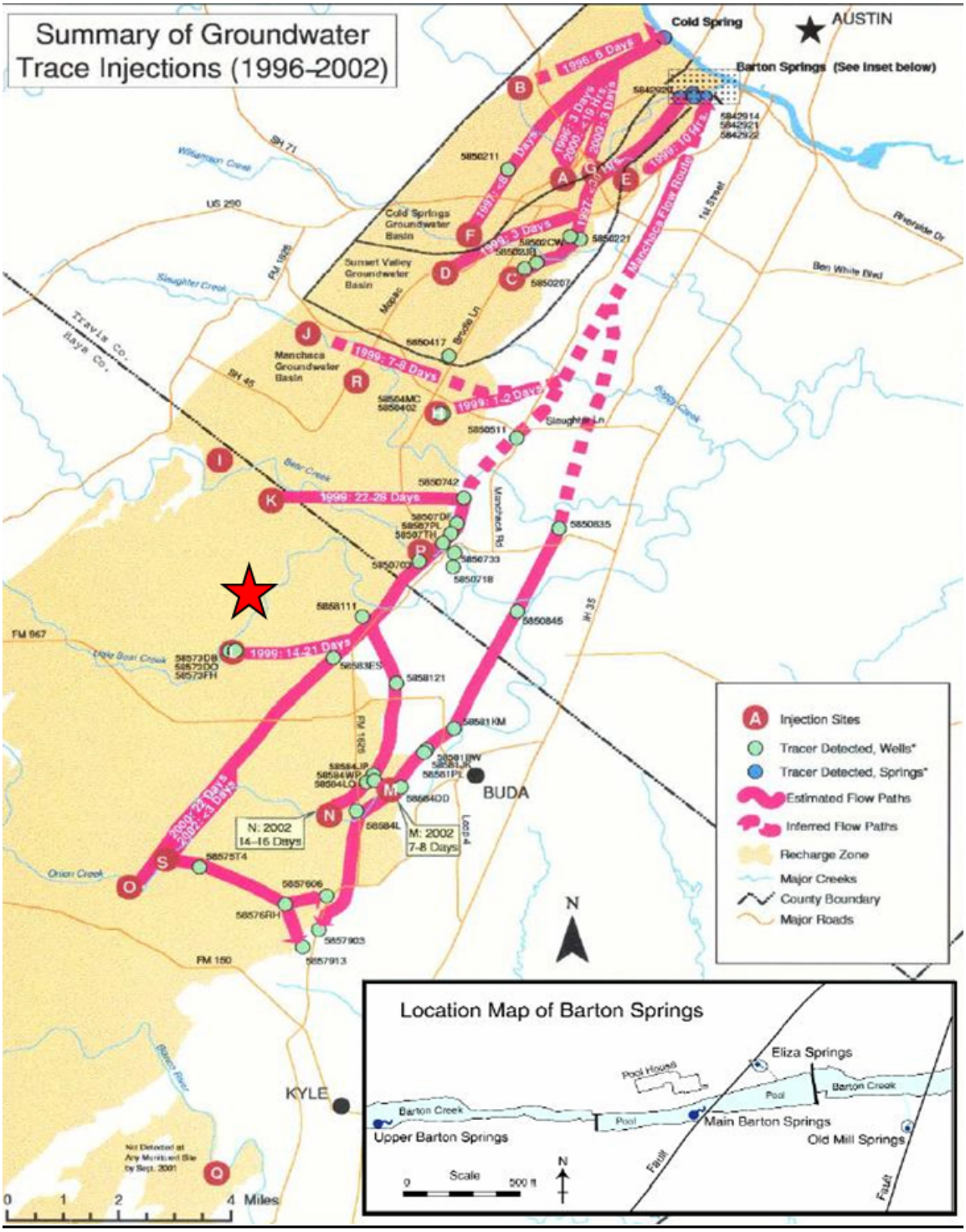

Figure 2.3 Groundwater flow system near Stoneledge Quarry (from BSEACD, 2002). The quarry location is marked with a red star.

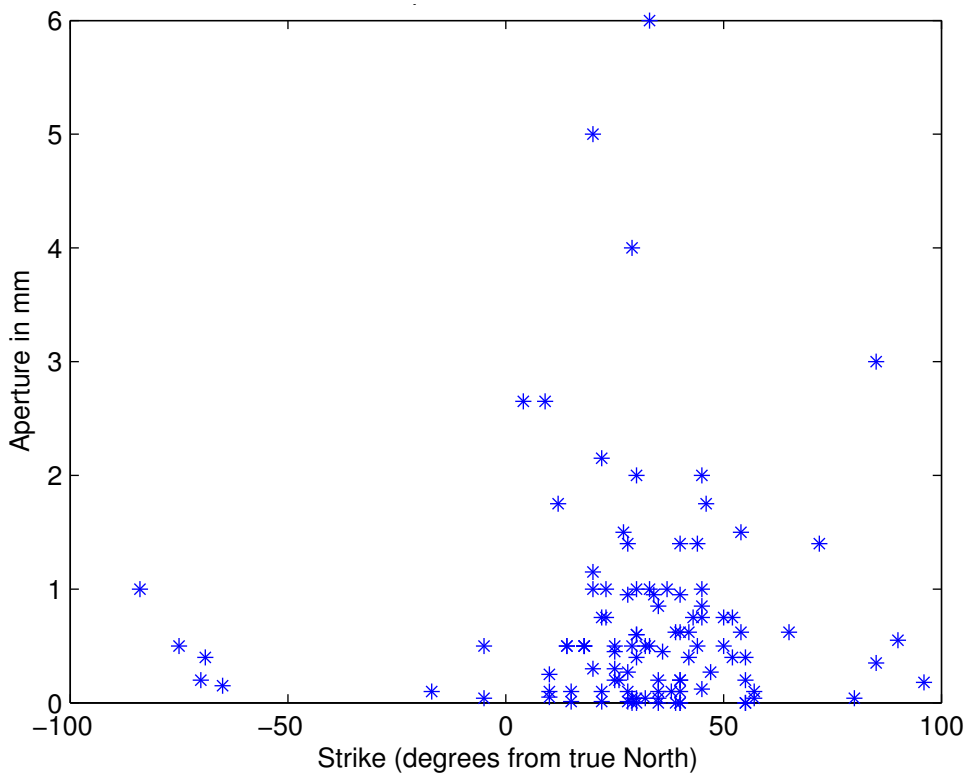

Figure 2.4 Graph of fracture strike versus fracture aperture from scan line data at Stoneledge Quarry.

Fracture density and aperture were measured using two scan lines on the quarry floor and one scan line on the quarry wall (Appendix A). Field measurement of fracture density is not a standardized technique. Additionally, there is a sampling bias due to the length and orientation of scan lines and only fractures large enough to be seen with a hand lens are measured. The fracture density is log-normally distributed (Figure 2.5). The mean fracture density (equivalent to fracture porosity) is estimated to be about 0.01 (around 1%). A one standard deviation confidence interval (containing about 2/3 of the total number of measurements) is estimated from the histogram to be approximately 0.2% to 5%. Additional details of fracture observations and calculations are given in Appendix A.

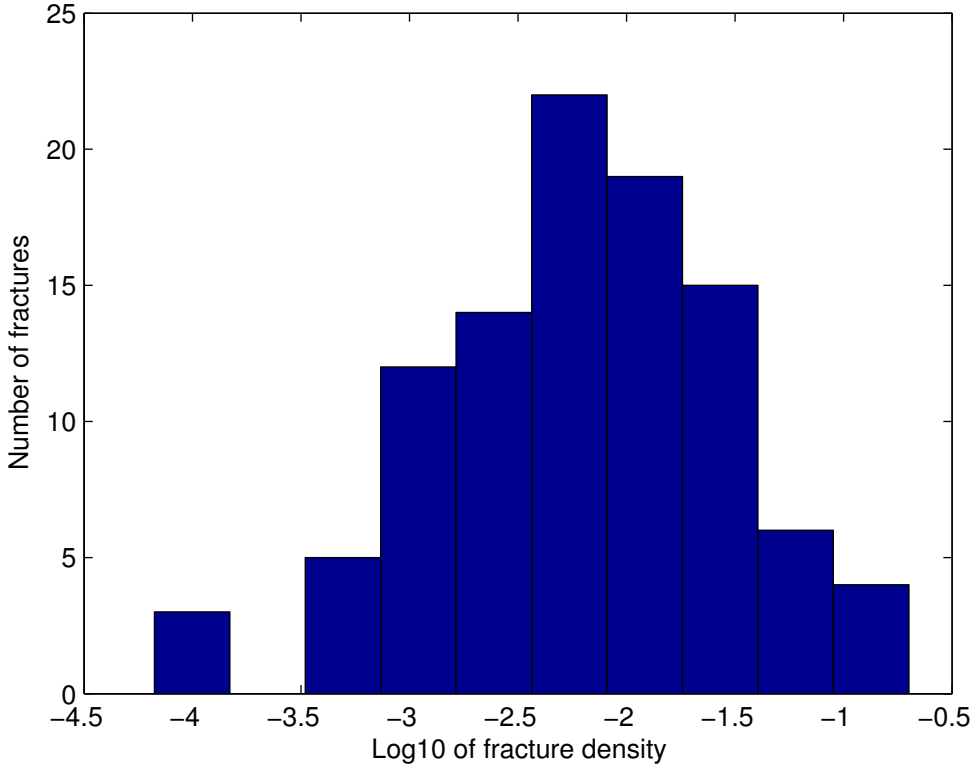

Figure 2.5 Fracture density distribution measured from three scan lines at Stoneledge Quarry.

The water table is at the surface in certain excavated areas of the quarry. From direct observations, it was about 17.2 m below the elevation of the seismic lines during Vibroseis data acquisition described in Chapter 5. Water table depth was noticeably lower during the period when the sledgehammer seismic source was used as described in Chapter 4. As a first approximation, the water table is expected to define the depth at which fractures become fluid-filled and would presumably be dry above this level. This is an important parameter in developing a seismic velocity model to interpret the observed seismograms.

2.3 SURVEY DESIGN AND IMPLEMENTATION

With a limited number of recording channels, walk-away surveys were conducted in which either receivers are fixed and source is moved or source is fixed and receivers are moved. Both variants were employed during field acquisition (Figure 2.6). A range of source-receiver offsets from 10 m to 495 m was possible and generally limited at the upper end by site conditions. Three survey lines were collected at different azimuths (Figure 2.7). Line 1 is oriented approximately at N13W and Line 2 at N88E. Line 3 is oriented at N30E, roughly parallel to the trend of the primary fracture set and regional faulting. The nearly orthogonal Lines 1 and 2 supply additional azimuths to determine anisotropic seismic properties and these orientations provided the largest offsets available at the site. Spacing between receivers is 5 m for all surveys, except on Line 3 of the Vibroseis source, spacing is 10 m. Source spacing was 35 meters. Due to site restrictions, the Vibroseis source was required to remain on quarry roads. Survey parameters for the hammer and Vibroseis source data are summarized in Table 2.1.

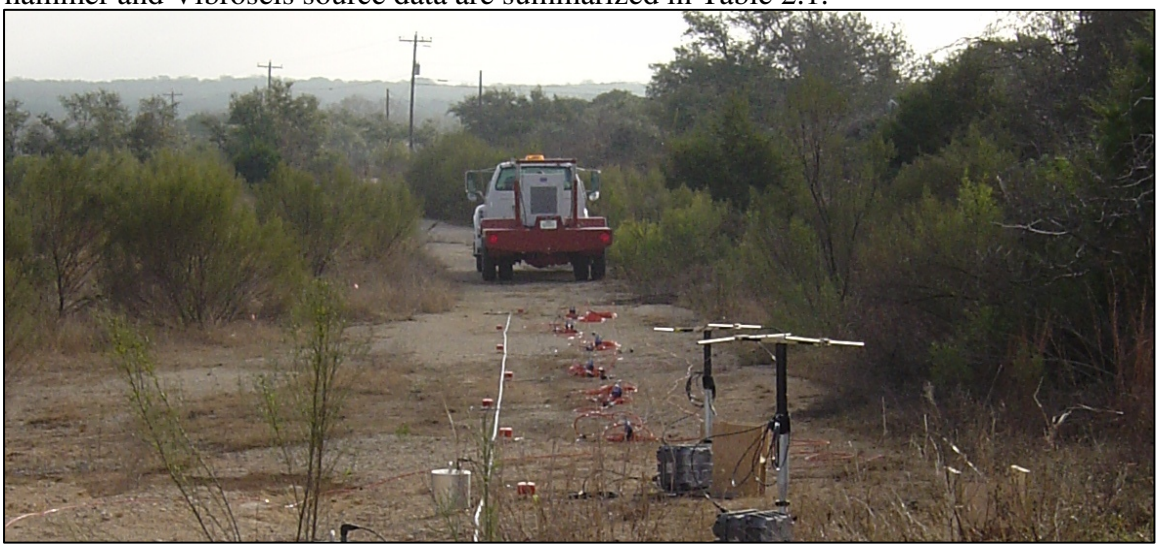

Figure 2.6 Photograph of seismic acquisition using the Vibroseis source. Receivers with both cable and wireless connection were used with the Sercel recording system. A separate vehicle contained recording equipment.

Figure 2.7 Aerial photograph of Stoneledge Quarry with approximate survey line orientations (Google, 2005). For scale, Line 2 is approximately 495 m long and there are two homes located south of Line 2.

Table 2.1 Summary of seismic survey parameters.

	9C Vibroseis Survey	3C Sledgehammer Survey
Recorder	Sercel 408XL System	Geometrics Inc. GEODE
Sample interval	1.0 ms	0.25 ms
Sample rate	1000 Hz	4000 Hz
Record Length	15 s	4 s
Source	IVI Minivib	Sledgehammer
Input sweep length	8 s	n/a
Chirp description	400 Hz down to 5 Hz	n/a
Force input direction	vert, horiz., inline & crossline	vertical
Offset	10 m to 1st receiver	10 m to 1st receiver
Receivers	Mark Products	Geometrics Inc.
Components	vertical, horizontal inline & crossline	vertical, horizontal inline & crossline
Natural frequencies	10 Hz	10 Hz vert., 8 Hz horiz.
Line 1	North-South N13W	North-South N13W
Line length	295 m	190 m
Receiver Spacing	5 m	5 m
# of receiver stations	9	9
Source Increment	35 m	35 m
Line 2	East-West N88E	East-West N88E
Line length	495 m	295 m
Receiver Spacing	5 m	5 m
# of receiver stations	9	9
Source Increment	35 m	35 m
Line 3	Parallel to fracture strike N30E	Parallel to fracture strike N30E
Line length	230 m	230 m
Receiver Spacing	10 m	5 m
# of receiver stations	23	9
Source Increment	0 m	35 m

Three-component (3C) seismic data are collected with the sledgehammer source. The 24 channel Geode recorder allowed eight, 3C geophones for each source location. Sledgehammer survey acquisition on Lines 1, 2, and 3 have fixed geophone locations and moving source locations. Nine-component (9C) seismic data are collected using the Vibroseis source. Vibroseis survey acquisition Lines 1 and 2 have fixed geophone

locations and moving source locations. Line 3 uses moving geophone locations and fixed source locations. The input signal from the Vibroseis source is an 8 second linear sweep. The data were recorded as uncorrelated seismograms. The ground force at each source location was recorded and used as the correlation operator in subsequent processing. Correlation compresses the 8 second Vibroseis wavelet so that the effective wavelet resembles a zero-phase band limited impulsive source.

The frequency content of the Vibroseis data is controlled by the sweep parameters but can also be obtained by computing a Fourier power spectrum for individual seismic traces. For the sledgehammer source, peak energy is typically between 30 Hz and 200 Hz, with an effective upper limit around 300 Hz (Figure 2.8). This is true for all three components on all three lines in the data set. For the Vibroseis data set, peak energy is typically between 20 Hz and 200 Hz, with an effective upper limit around 100 Hz (Figure 2.9). This is true for all nine components on all three lines in the data set.

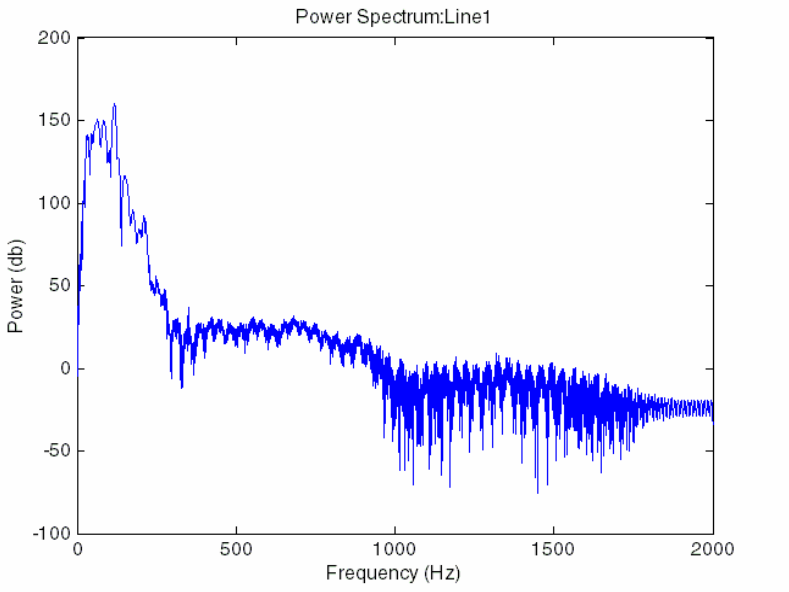

Figure 2.8 Power spectrum plot of typical seismic trace from the hammer data set. This trace is from Line 1 recorded on the inline horizontal geophone.

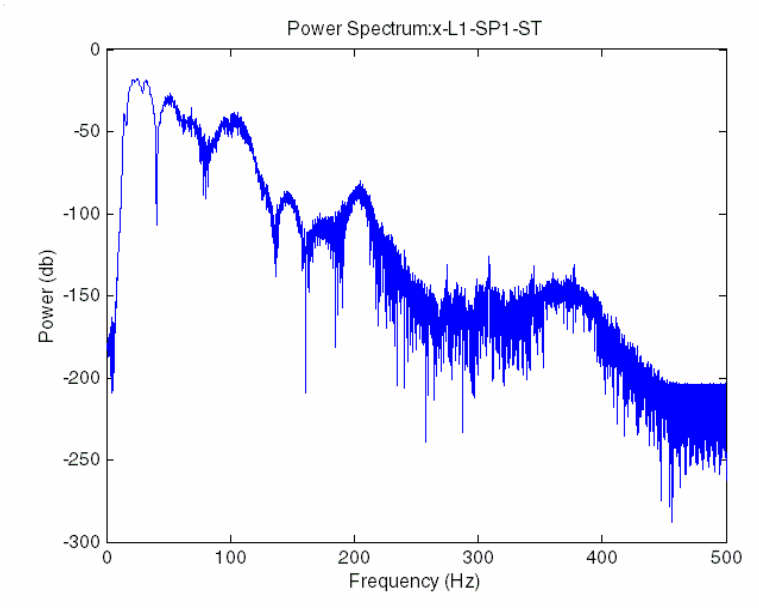

Figure 2.9 Power spectrum plot of typical seismic trace from the hammer data set. This trace is from Line 1, crossline source recorded on the inline horizontal geophone.

Chapter 3: Seismic Anisotropy Theory and Fracture Parameters

This chapter provides a summary of published theories and predictions related to elastic anisotropy in a fractured solid and shows examples of synthetic seismograms that implement this theory. The purpose is to develop the background for quantitative interpretation of observed seismograms presented in later chapters.

3.1 ANISOTROPY OVERVIEW

Anisotropy is the directional dependence of properties in a medium. Seismic wave anisotropy may arise from a number of causes including: preferred orientation of mineral grains and pores, microcracks, and fractures that are filled or unfilled. In addition, laminations due to sedimentary bedding and regional stress may produce anisotropy (Beckham, 1996; Cheadle et al., 1991; Tatham and McCormack, 1991). The field experiments in this study were conducted in an area where massive limestone contains near-vertical fractures that are dominantly aligned in one direction. Near surface fractures are observed to be mostly open and are presumed water-filled below the observed water table. Therefore, it is appropriate to present the predictions of theory for seismic wave anisotropy associated with vertical aligned fractures that are either air- or water-filled.

A qualitative understanding of effects of aligned fractures can be found in Figure 3.1. A first point is that wave types in isotropic media (P and S waves) are not precise descriptions in anisotropic media. However, in the field experiments, we expect weak anisotropy and continue to use the isotropic wave names for the observed waves. A P wave propagating parallel to fractures, for instance, will have a faster velocity (Vp) than a P wave propagating perpendicular. This velocity difference occurs because the wave propagating parallel to the fractures must, as a longitudinal wave, deform stiff, coherent material between the fractures. The wave propagating perpendicular to the fractures

experiences an average of more- and less-compliant material due to the presence of fractures, resulting in a lower velocity (Tatham and McCormack, 1991). Similar differences are expected for shear wave velocities. Shear and Rayleigh wave velocities depend on orientations of particle motion (polarization direction) relative to the fractures. As a result, shear waves may be split into two arrivals, depending on their polarization.

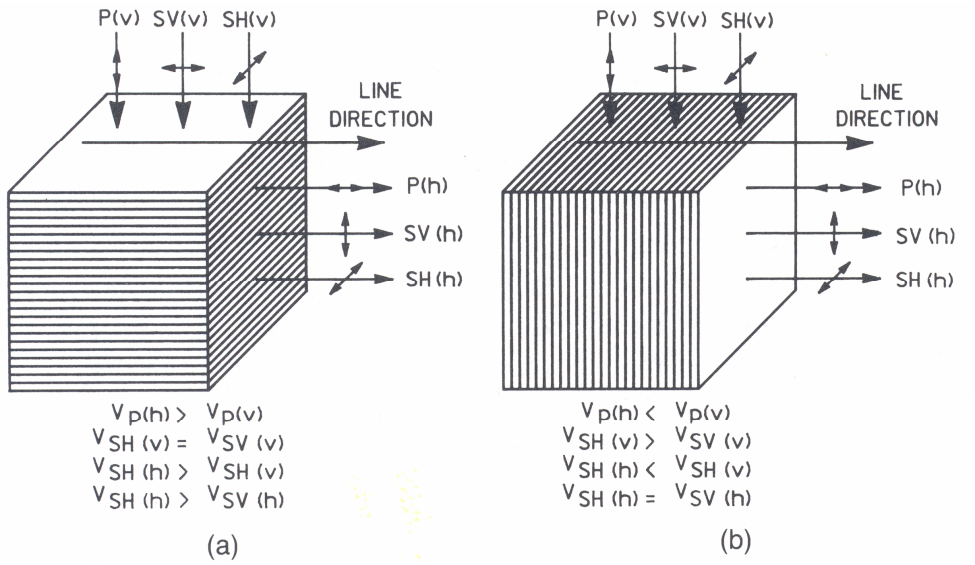

Figure 3.1 Effects of anisotropy on seismic body wave velocities (Tatham and McCormack, 1991).

Fracture density, e, in fracture anisotropy studies has two meanings: 1) a quantity estimated in field measurements and 2) a parameter in seismic anisotropy theory. In both cases, the quantity is dimensionless and equal to effective fracture porosity of the solid. A goal of this investigation is to attempt an observational comparison of the two.

The field value of e was estimated by two methods that use measured fracture spacing and aperture along linear traces along a flat surface. These linear traces are called scan lines. Measurement of spacing and aperture along scan lines is common practice in structural geology. One estimate of e is the product of mean spacing between fractures

(fractures/m) and mean aperture per fracture (m/fracture) for all scan lines. The second estimate is the quotient of the sum of all fracture apertures (m) divided by the sum of all scan line lengths (m) for all scan lines. These calculations are described in detail in Appendix A, which shows that e behaves as a random variable with a log-normal distribution and provides a method to assign a confidence interval. At the quarry site investigated in this study, the estimate of e is slightly below 0.01 (1% fracture porosity) and an approximate one standard error confidence interval includes the range from 0.2% to 5%.

Anisotropy is a scale dependent property of a medium. The long wavelength limit describes the case in which seismic wavelengths are much larger than the scale of features causing anisotropy, such as cracks or laminations. In this study, seismic wavelengths are much greater than fracture spacing and aperture. Experimental investigations of anisotropic properties in the long wavelength limit have been conducted at the laboratory scale [for example, Ass'ad et al. (1992), Tatham et al. (1992) and Rathore et al. (1994)]. Ass'ad et al. (1992) studied effects of aligned penny-shaped cracks on shear wave velocities based on Hudson's theory described in the section below. They used frequencies between 30 and 60 kHz (20 to 40 mm wavelengths). The experimental model was an epoxy resin with rubber disk inclusions to represent weak but filled fractures. Fracture density was varied from 1 to 10%. Results of variations in shear wave velocity with fracture density agreed with theory for densities below 10%. Above 10%, the shear wave velocity diverges from theoretical predictions due to crack-crack interactions. Predictions of velocity variations from theory are presented in the next section.

Tatham et al. (1992) experimentally studied effects of aligned vertical fractures of infinite height and length on shear wave velocity with varying fracture densities. They

used a dominant frequency of 50 kHz with an average wavelength near 25 mm. The experimental model consisted of multiple Plexiglass plates separated by thin layers of water to represent saturated fractures. Fracture density was varied from 2 to 32 fractures per wavelength. Results of variations in shear wave velocity with fracture density agreed with Hudson's theory and later formulations by Schoenberg and Douma (1988) and Thomsen (1986).

Rathore et al. (1994) studied the effects of aligned penny-shaped cracks on P and S wave velocities and compared observations with Hudson and Thomsen's (1995) theories. The experiment used a dominant frequency of 100 kHz with average wavelengths of about 22 mm and 14 mm for the P and S waves, respectively. The experimental model consisted of sand cemented with epoxy with embedded metallic disks. The disks were subsequently chemically removed to simulate matrix porosity and weak, air-filled fractures. Fracture density was 10%. S wave velocities varied with direction relative to fracture orientation and P and S velocities were found to vary in ways consistent with theory.

Experimental investigations have also been conducted at the exploration scale in the long wavelength case, with fractured material at reservoir depths. Examples include Lewis et al. (1991) and Lynn and Thomsen (1990). Lewis et al. (1991) studied P and S wave velocities to estimate anisotropy and infer vertical fracture orientation over a 25 m by 25 m area. This experiment used a dominant frequency of 250 Hz. Results of variations in S wave velocity with fracture density agreed with theories cited previously. Lynn and Thomsen (1990) studied anisotropy of P and SH wave velocities on two roughly orthogonal lines of seismic data spanning over 4000 m, with frequencies from 14 Hz to 56 Hz (P wavelengths between 76 and 305 m and SH wavelengths between 38 m

and 152 m). Results showed variations in velocities with azimuth up to 5% and are consistent with theories cited previously.

My research is distinguished from these other studies by the use of surface seismic measurements, where direct observation of fractures in outcrop can be compared with seismic effects. Depth of investigation for my research spans from the surface to a few hundred meters. At least one other study in the published literature (Bamford and Nunn, 1979) also compares surface measurements with direct observation of fractures in outcrop. The seismic refraction survey of Bamford and Nunn (1979) used a weight drop source and fan-style offset-shooting to observe P wave velocity anisotropy for azimuths spanning 180°. Three different Carboniferous limestone sites were studied covering areas about 50 m by 70 m at each site. This experiment used a dominant frequency of less than 400 Hz with minimum wavelengths around 10 m to 15 m for P waves. Velocity anisotropy of 15% to 29% was found with orientations roughly corresponding to natural and induced fractures previously mapped in the areas. P velocities were found to vary in ways consistent with theory.

3.2 THEORETICAL MODELS OF ANISOTROPY

As noted in the overview of experimental studies in the previous section, prominent theoretical models of anisotropy include those of Hudson (1980 and 1981), Schoenberg and Douma (1988), and Thomsen (1986). Hudson (1980, 1981) derived equations of wave motion through a solid containing penny-shaped cracks using a scattering wave model. Expressions for P, SV, and SH wave velocities were obtained for dry and saturated, aligned and randomly oriented cracks. Hudson et al. (1996) expanded upon earlier models to account for matrix porosity. Schoenberg and Douma (1988) used an equivalent medium to represent parallel fracture systems of any anisotropy (e.g., triclinic, monoclinic, orthorhombic, or transversely isotropic). Expressions describe

elastic wave propagation through anisotropic media in terms of familiar P, SV, and SH wave velocities. Thomsen (1986) derived simplifying equations for weak (10%-20%) anisotropy using combinations of elastic parameters that are related to P, SV, and SH wave velocities. Thomsen's model was revised in 1995 to account for matrix porosity. Porosity, ϕ, is the ratio of the volume of pores to the volume of rock. Therefore, porosity equals the fracture density plus matrix porosity, ϕ_m.

These theoretical models predict elastic wave velocities in anisotropic media and may be useful in estimating fracture parameters, including fracture density. Variations in P, SV, and SH wave phase velocities can be obtained for dry and saturated fractures and for azimuthal changes with respect to fracture orientation. Phase velocity is the wave velocity of a given phase (peak or trough) and is the velocity a wavefront appears to have along a line of geophones (Sheriff, 2002).

P, SV, and SH wave phase velocities as related to coefficients of the elasticity matrix were derived by Daley and Hron (1977) and presented in Thomsen (1986). The equations for these velocities are shown in Equations 3.1 through 3.3. Following the work of Schoenberg and Douma (1988), an effective elastic coefficient matrix for an isotropic medium containing fractures can be obtained. The effective elastic coefficient matrix will vary for dry and saturated conditions of the medium.

$$\rho V_p^2(\theta) = \frac{1}{2}\left[A\sin^2\theta + D(\theta)\right] \tag{3.1}$$

$$\rho V_{SV}^2(\theta) = \frac{1}{2}\left[A\sin^2\theta - D(\theta)\right] \tag{3.2}$$

$$\rho V_{SH}^2(\theta) = B\sin^2\theta + C\cos^2\theta \tag{3.3}$$

where ρ is lithologic density, θ is incidence angle, and A, B, C, and D are related to the elastic coefficients of the medium (Appendix B, Equation B.3 through Equation B.5).

Calculations of P, SV and SH velocity variations with azimuth from Equations 3.1 through 3.3 are shown in Figure 3.2 through Figure 3.5 for parameters described in

Appendix B. Saturated and unsaturated responses are shown for a homogeneous medium containing aligned vertical fractures at fracture densities of 0% (unfractured), 1%, and 10%.

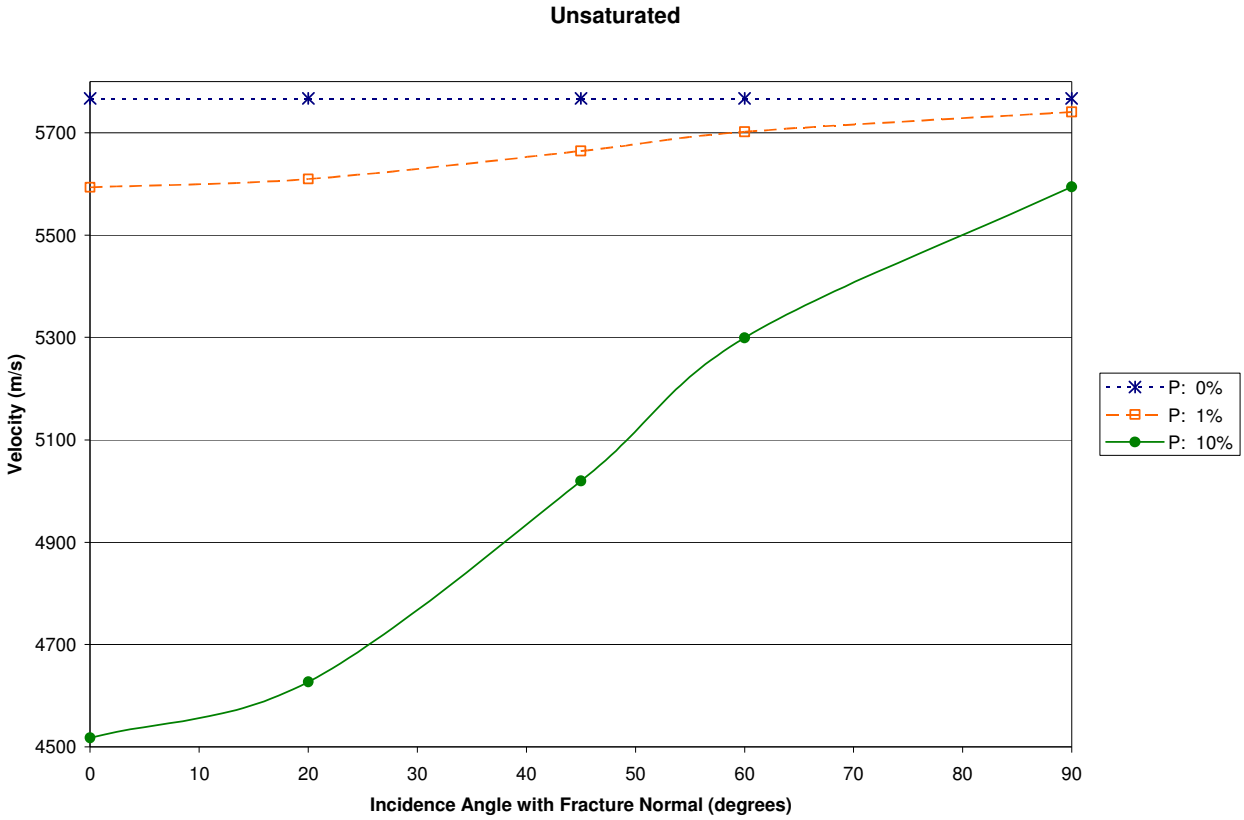

Figure 3.2 Plot of variations in P wave velocity versus azimuth for a homogeneous medium containing unsaturated, vertical fractures. Three fracture densities (0% = unfractured) are considered.

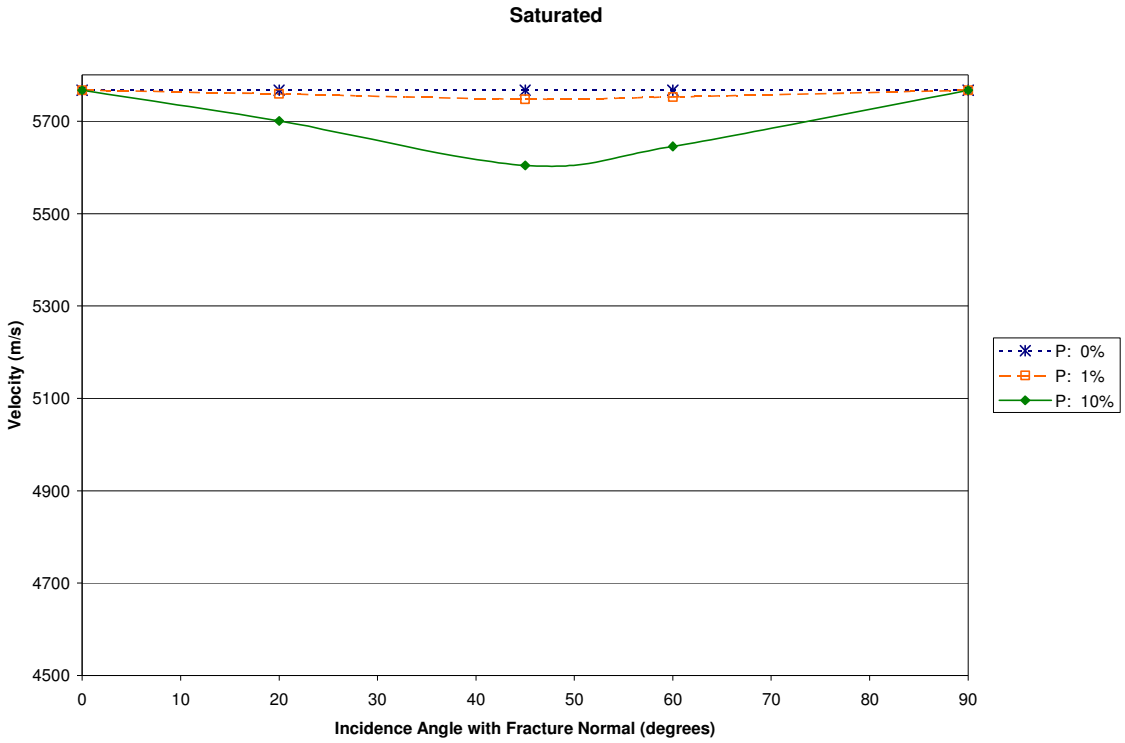

Figure 3.3 Plot of variations in P wave velocity versus azimuth for a homogeneous medium containing saturated, vertical fractures at three fracture densities.

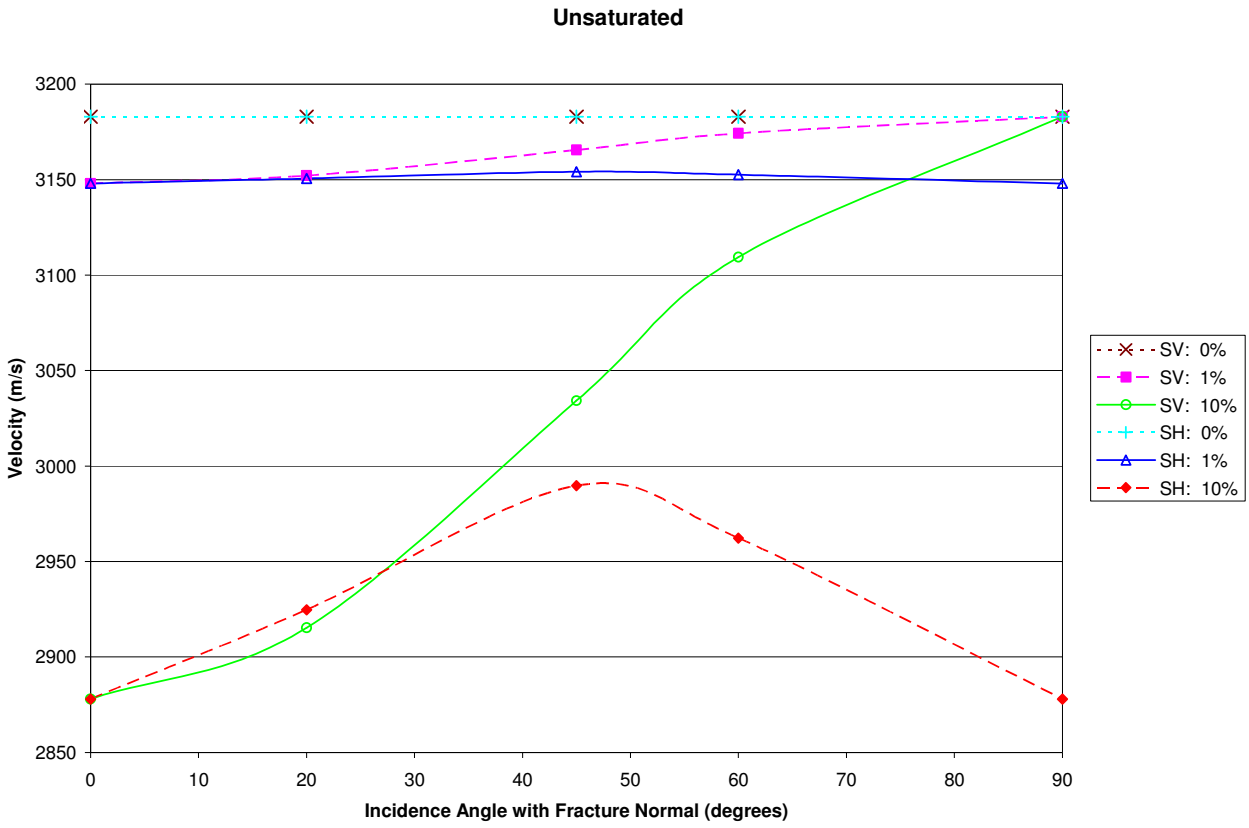

Figure 3.4 Plot of variations in S wave velocity versus azimuth for a homogeneous medium containing unsaturated, vertical fractures at three fracture densities.

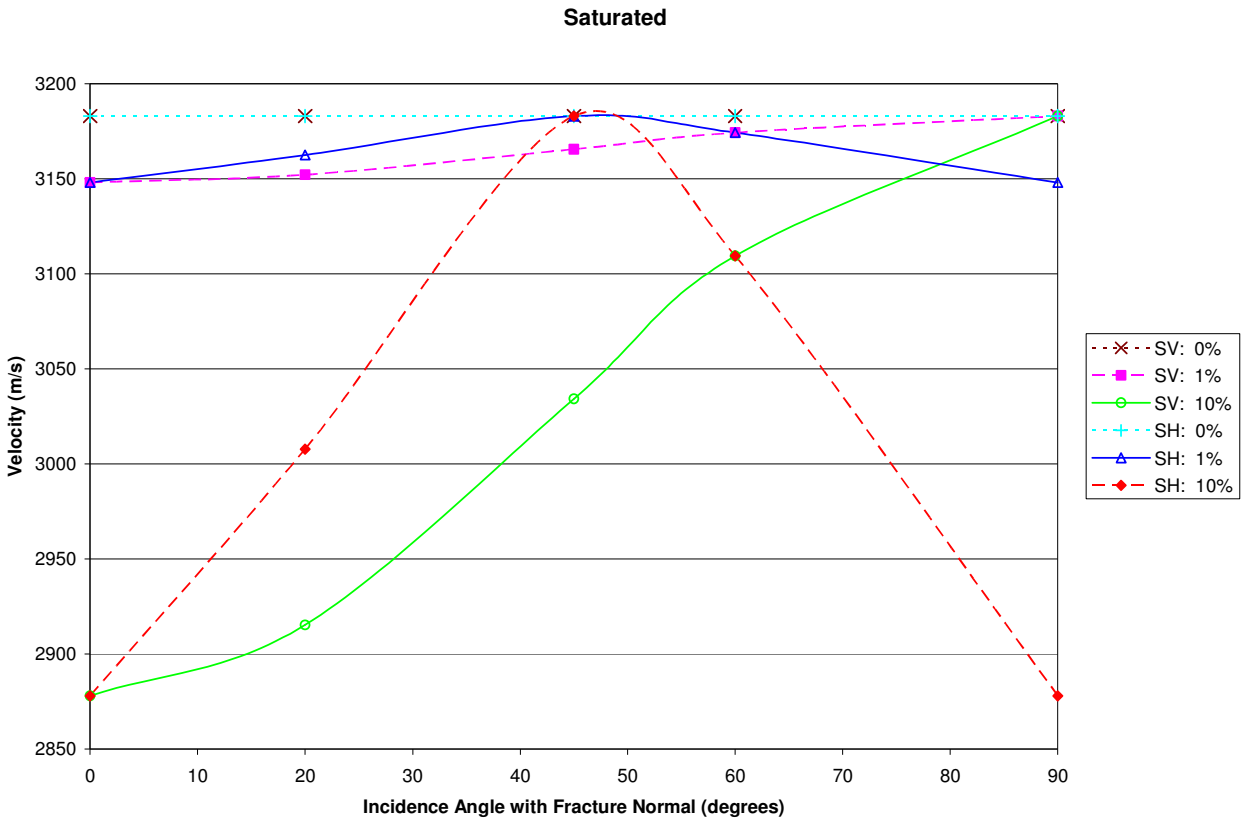

Figure 3.5 Plot of variations in S wave velocity versus azimuth for a homogeneous medium containing saturated, vertical fractures at three fracture densities.

Several observations can be made regarding wave type and azimuthal variations. P wave velocities for saturated fractures are greater than dry fractures for all incident angles with the fracture normal. Waves propagating parallel to fracture strike (incidence angle of 90°) have the fastest P wave velocity for dry fractures and the greatest difference in velocity between the SV and SH components for both dry and saturated fractures. Additionally, the P and SV velocities at this angle are equal to those velocities for the unfractured, saturated case. The SH wave velocity at an incidence angle of 90° is equal to the SV wave velocity at an incidence angle of 0°. Therefore, P and SV velocities at an incidence angle of 90° plus the fracture density can be used to describe the velocity model

for the medium regardless of incidence angle. Waves propagating perpendicular to fractures (incidence angle of 0^{o}) have the slowest P wave velocity for dry fractures and equal velocities for the SV and SH components for both dry and saturated fractures.

The time delay between the SV and the SH arrivals (shear wave splitting) is a result of the average anisotropy for the raypath, and dependent on fracture density. A greater time delay indicates a greater amount of anisotropy in the medium and a larger value of the anisotropy parameter, γ (Lewis et al., 1991; Li and Mueller, 1997; Mueller, 1992). γ is a nondimensional measure of anisotropy developed by Thomsen (1986) to simplify equations for anisotropic media and depends upon a ratio of parameters from the elastic constant matrix as described in Appendix B. To estimate γ from observations, it can be expressed in terms of the differences in shear velocities from traditional notions of anisotropy, the fractional difference between the parallel and perpendicular velocities of the waves through a fractured medium (Lynn and Thomsen, 1990; Sheriff and Geldart, 1995; Tatham et al., 1992; Thomsen, 2002), by

$$\gamma = (Vs_1 - Vs_2) / Vs_2. \qquad 3.4$$

Vs_1 is the velocity of the fastest shear wave component (traditionally SV) and Vs_2 is the velocity of the slowest shear wave component (traditionally SH). The parameters above can be measured from the seismic data. Fracture density as a seismic measurement is equivalent to the following expression (Thomsen, 1995), where σ is Poisson's ratio of the solid grains.

$$e = \gamma / (8/3) [(1-\sigma) / (2- \sigma)] \qquad 3.5$$

3.3 SYNTHETIC SEISMOGRAMS

Synthetic seismogram software has been developed to implement fracture anisotropy theory for a layered material. Anivec™, described by Mallick and Frazer (1990), produces synthetic seismic data based on the theory of wave propagation in

horizontally stratified, anisotropic media. The software uses the reflectivity method, which first determines single-frequency single-wavenumber, plane wave reflection coefficients of a layered stack of fractured solids with dry or fluid filled fractures. Plane waves then are summed over frequency and wavenumber to simulate the wavefield for various source and receiver orientations and offsets. The input parameters used in the calculations are given in Appendix B.

The synthetic seismograms are used to identify arrivals on observed seismograms and to aid in the construction of a layered model consistent with field seismograms. An example seismic profile for an unfractured, homogeneous half-space having input parameters given in Table 3.1 is shown in Figure 3.6 for the vertical source, vertical receiver component and offset range and frequencies similar to those of field seismograms. Slopes of arrivals are used to calculate the velocities of each wave. The P and S wave velocities of the synthetic seismograms are the same as the input velocities. For the unfractured case, results are the same for any incidence angle with the fracture normal and for both saturated and unsaturated conditions. All porosity for this model is assumed due to fractures.

Table 3.1 Input model parameters used to create synthetic seismogram in Figure 3.6.

Layer	**P-wave Velocity (V_p) (m/s)**	**S-wave Velocity (V_s) (m/s)**	**Lithologic Density (ρ) (kg/m^3)**	**Fracture Density (e) (%)**	**Saturation**
Half-space	5767	3183	2650	0	Saturated

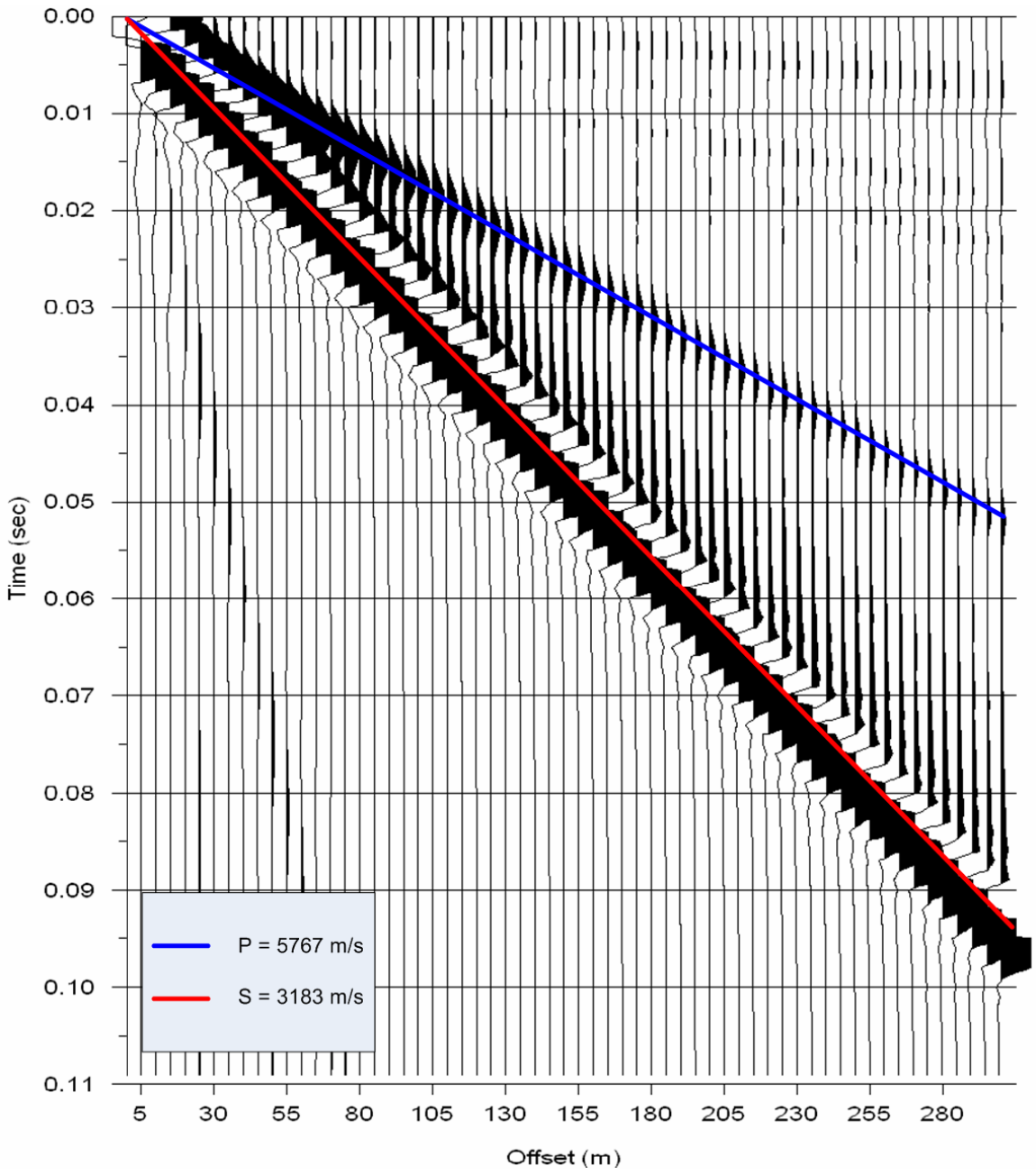

Figure 3.6 Synthetic profile of the vertical source, vertical receiver component for an unfractured, homogeneous half-space. Results are the same for any incidence angle with the fracture normal and for unsaturated conditions.

An example seismic profile for an homogeneous half-space containing 10% fractures and having input parameters given in Table 3.2 is shown in Figure 3.7 for the

vertical source, vertical receiver component. This profile is at an incidence angle of 0^{o} with the fracture normal (perpendicular to fracture strike) and the fractures are dry. As with the results from theory shown in Figure 3.2 and Figure 3.4, both P and S wave velocities are decreased from the input velocities.

Table 3.2 Input model parameters used to create synthetic seismogram in Figure 3.7.

Layer	**P-wave Velocity (V_p) (m/s)**	**S-wave Velocity (V_s) (m/s)**	**Lithologic Density (ρ) (kg/m^3)**	**Fracture Density (e) (%)**	**Saturation**
Half-space	5767	3183	2650	10	Unsaturated

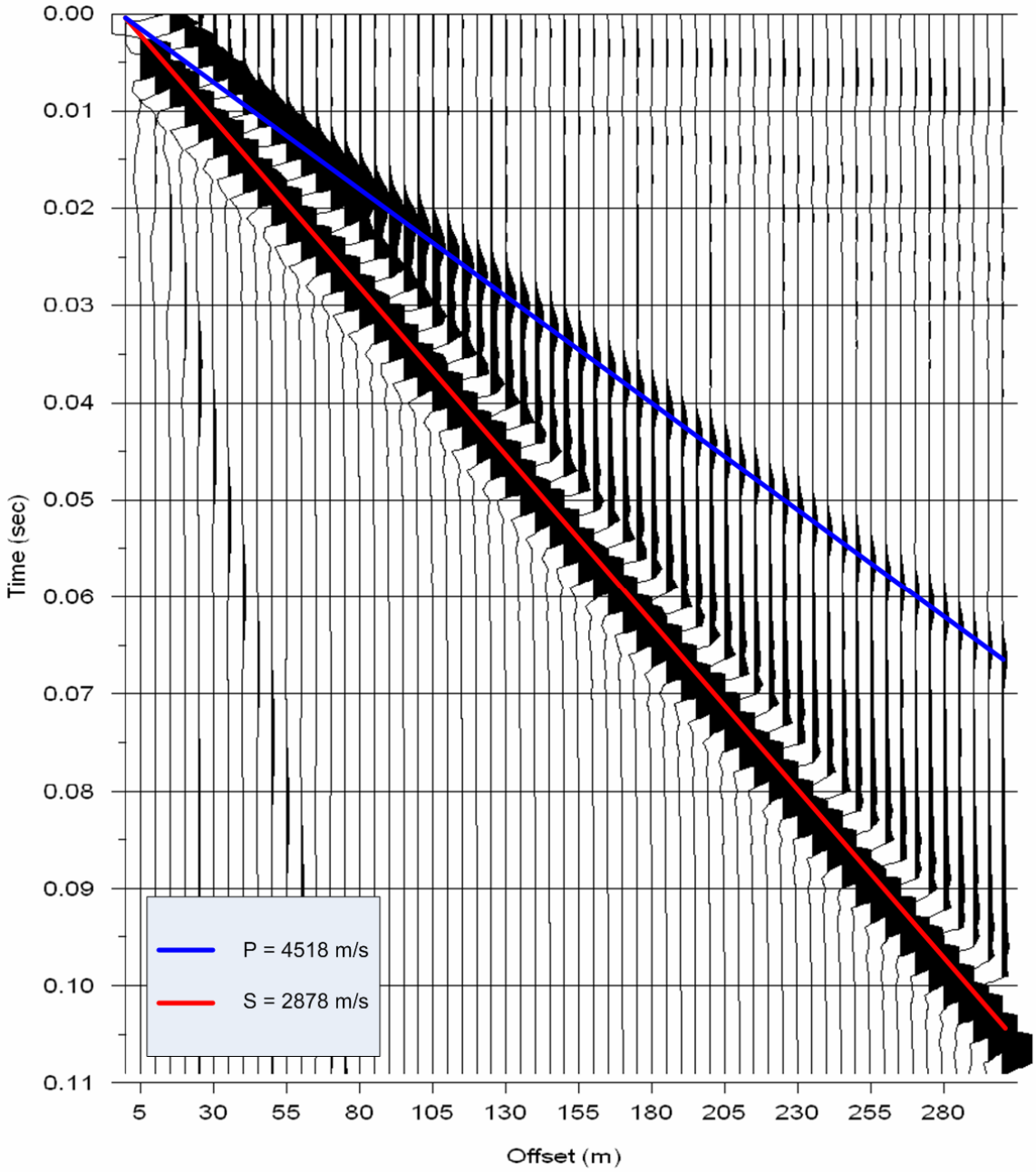

Figure 3.7 Synthetic profile of the vertical source, vertical receiver component for an unsaturated, homogeneous half-space containing 10% fractures at an incidence angle of 0° with the fracture normal (perpendicular to fracture strike). Velocities are decreased from input parameters due to fractures.

3.4 WAVE VELOCITIES AND WATER TABLE DEPTH

Depth to the water table is found using the slope-intercept refraction method for determining layer thickness (Gardner, 1939). Depth to the first refracting boundary can be calculated using the intercept time in Equation 3.6 or crossover distance in Equation 3.7.

$$Depth = \frac{\frac{t_i}{2}(V_2 V_L)}{\sqrt{V_2^2 - V_1^2}} \qquad 3.6$$

$$Depth = \frac{x_{co}}{2}\sqrt{\frac{(V_2 - V_1)}{(V_2 + V_1)}} \qquad 3.7$$

V_1 and V_2 are the velocities of the layers above and below the refracting boundary, respectively. t_i is the intercept time of the slope of first refractor on the time-distance curve. x_{co} is the crossover distance or the offset distance at which the travel times of V_1 and V_2 are equal. Depths found using the intercept time equation (3.6) are generally more accurate than the crossover distance equation (3.7) because t_i can be found with greater accuracy than x_{co} (Sheriff and Geldart, 1995).

Depth to the water table is calculated first by determining if fractures are filled with air or water and then by determining the depth at which fractures become water-filled. Converting the time of abrupt increase in P wave velocities to depth corresponds to the depth of the water table. Shear wave velocities should have no corresponding velocity change. The velocity of P waves in water (about 1500 m/s) is significantly greater than in air (about 330 m/s). Therefore P wave velocities increase as the waves travel from air-filled fractures into water-filled fractures. Shear wave velocities should remain relatively unchanged because they are not sensitive to fluids. However, West and Menke (2001) have observed that shear waves are sensitive to moisture content in unconsolidated sandy media. In the unsaturated zone, an increase in moisture increases cohesion between the

grains, in turn, increasing shear wave velocity. In the saturated zone, the shear strength between the grains is reduced, thereby decreasing the shear wave velocity. The actual water table boundary is not sharp, due to capillary forces. The boundary from dry sediments to full saturation actually occurs over a small range of depths. Therefore, the water table is slightly shallower than the seismic boundary of abrupt velocity increase (Bradford, 2002).

Chapter 4: Estimating Velocity Anisotropy and Fracture Properties: Sledgehammer Source

4.1 INTRODUCTION

In this chapter, I present seismograms for the seismic data taken with a high frequency source (sledgehammer), to observe velocity anisotropy and estimate depth to the water table. In section 4.2, I describe how synthetic seismograms are used to identify arrivals expected in the data. I also discuss Rayleigh waves that are large amplitude and low frequency events. In section 4.3, I present observed vertical receiver seismograms, interpret arrivals, and estimate velocities. In section 4.4, I evaluate modal propagation of surface waves and compare the results with observations from the data. In section 4.5, I present inline and crossline seismograms, describe arrivals and velocities, and interpret these using synthetic seismograms of inline and crossline components. In section 4.6, I estimate water table depth. In section 4.7, I present estimates of fracture density and evidence of velocity anisotropy. In section 4.8, I present my conclusions from these results. Chapter 5 analyzes 9C data obtained using the 3C Vibroseis source with 3C receivers.

4.2 MODELING USING SYNTHETICS

Geologic and outcrop evidence suggest that the Edwards Aquifer at Stoneledge Quarry is massive and extends from the ground surface to depths well below the water table. The water table is visible at the lowest parts of the quarry floor. In the presence of fractures, one might anticipate a first-order seismic model of a single lower speed layer over a half-space. In this case, the lower speed layer would correspond to the dry fractures, while the higher speed half-space, starting at the water table, would contain fluid-filled fractures. This model is used in the interpretation of the seismic data. To

illustrate the general appearance of seismic data anticipated in this case, I compute seismograms using seismic velocities and lithologic density typical of limestone for unsaturated (upper layer) and saturated (half-space) conditions, including values that were obtained from observed seismograms. The parameters used to create synthetic seismograms are shown in Table 4.1. Figure 4.1 is a 2D schematic representation of some seismic ray paths for the model. The seismic waves used to estimate anisotropy at Stoneledge Quarry include direct P and S waves, refracted P and S waves, and surface waves. Using conventional methods, direct waves are used to estimate upper layer parameters and refracted waves are used to estimate half-space parameters. The thickness of the unsaturated layer in the model is 25 m. Rayleigh wave velocities are estimated from the Poisson's ratio at 1024 m/s for layer 1, and 2930 m/s for the half-space. Figure 4.2 shows the relationship between Rayleigh wave velocity and shear wave velocity as a function of Poisson's ratio.

Table 4.1 Input model parameters used to create synthetic seismograms.

Layer	**P-wave Velocity (V_p) (m/s)**	**S-wave Velocity (V_s) (m/s)**	**Lithologic Density (ρ) (kg/m^3)**	**Fracture Density (e) (%)**	**Saturation**
1 (25m thick)	2015	1113	2650	5	Unsaturated
Half-space	5750	3185	2650	5	Saturated

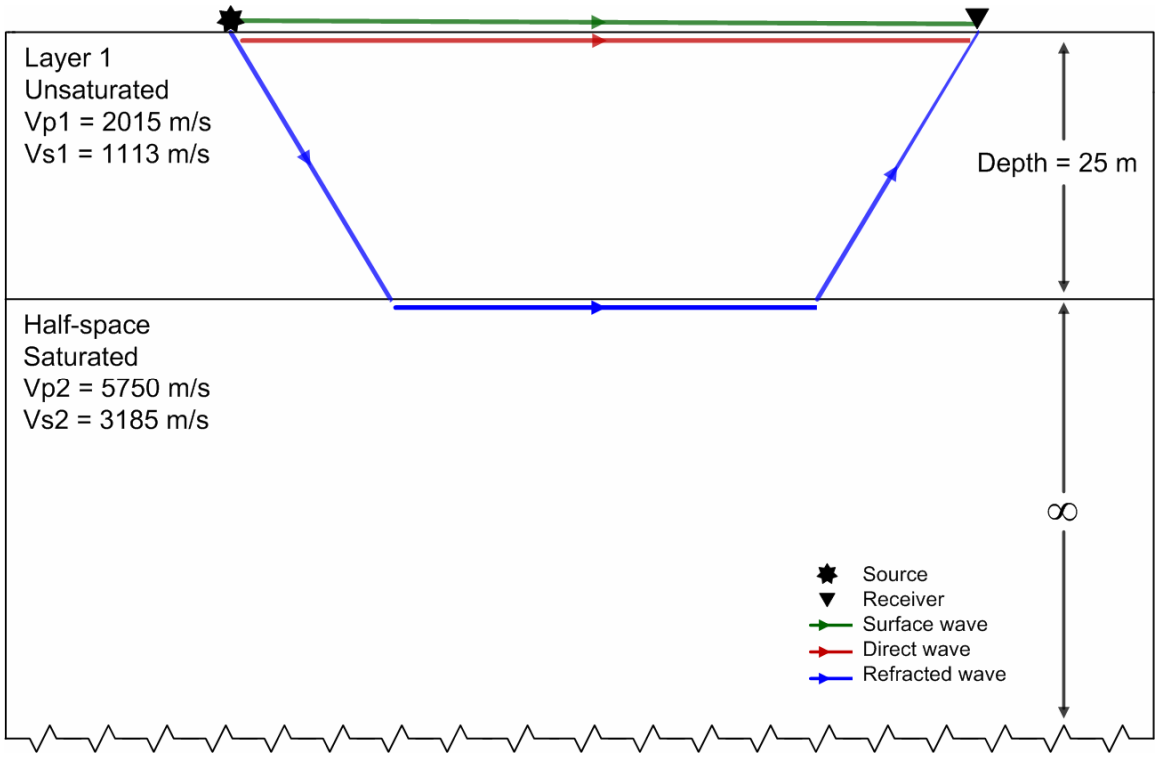

Figure 4.1 Schematic representation of the model and the ray paths of the expected seismic waves.

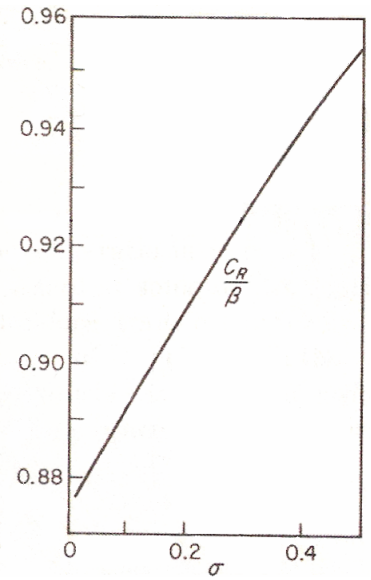

Figure 4.2 Relationship between Rayleigh wave velocity and shear wave velocity as a function of Poisson's ratio (Grant and West, 1965).

Synthetic seismic profiles were created as described in Chapter 3 and in Appendix B. The vertical source, vertical receiver component seismogram profile of a line of geophones 90° to the fracture normal (parallel to fracture strike) is presented in Figure 4.3. Identified waves are: refracted P (green), refracted SV (red), Rayleigh wave traveling at the half-space velocity (yellow), direct P (blue), and direct SV (pink). The slopes of these arrivals correspond well to the expected values from the model, as indicated in the figure. Hyperbolic moveout events are present in the synthetic profile corresponding to reflections from the interface. The waves in the synthetic profile from Figure 4.3 are the dominant waves expected in the data from Stoneledge Quarry with one exception. As observed below, the synthetics do not calculate events with the reverberant and dispersive nature of observed surface waves. Synthetic data aid in interpretation by displaying arrivals of interest without effects of noise, reflections from out-of-line, and other arrivals.

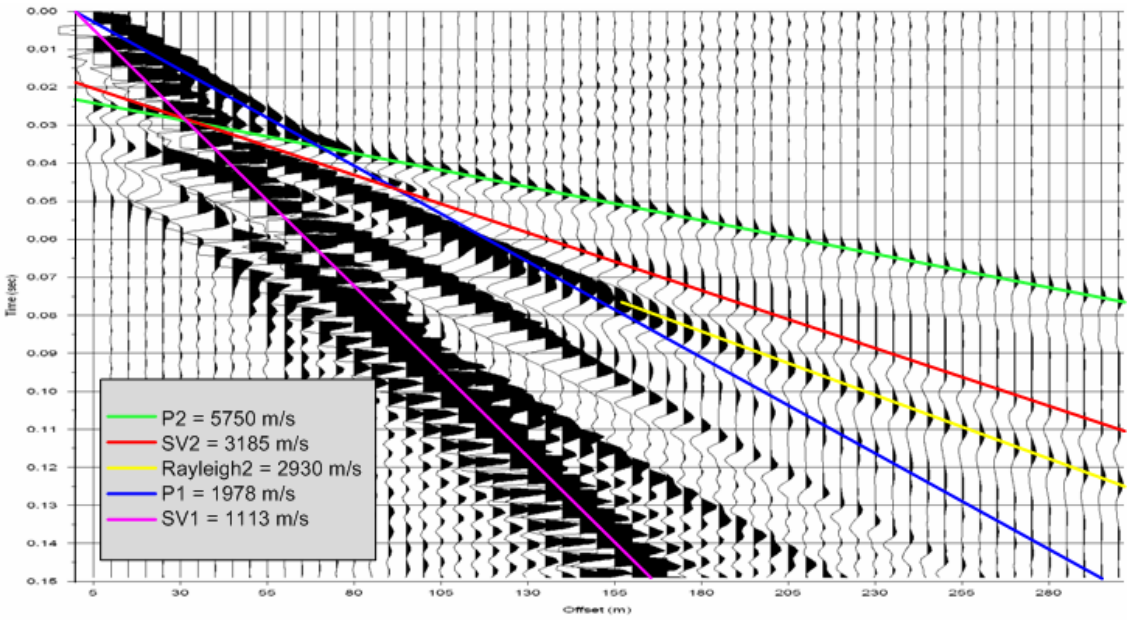

Figure 4.3 Synthetic seismic profile for the vertical source, vertical receiver component line of geophones oriented at 90° with the fracture normal for the model in Figure 4.1 with 5% fracture density.

When velocity increases with depth, Rayleigh-type surface waves may become dispersive. A general feature is that as offset increases, lower frequency waves will arrive first, while higher frequency waves arrive later. Dispersive Rayleigh-type waves exhibit upward curvature in walk-away seismic profiles as shown in Figure 4.4. The slowest arriving wave train spreads out (disperses) as it propagates. Also, the low frequency events arrive first, a situation called 'normal dispersion'. There is a slight upward curvature to the first arriving event in the surface wave train, corresponding to increasing phase velocity as the lower frequency component emerges from the wave train. Depending on structure and source properties, there may be multiple arrivals corresponding to different propagation modes. The effect of this dispersion is for the wave train to spread out (disperse) as offset increases and for the phase velocity (apparent velocity across the array) to increase with offset.

The dispersive nature of Rayleigh waves is not present in the synthetic seismograms. Instead, the program appears to use a non-dispersive velocity equal to 92% of the shear wave velocity. For most geologic materials, the Rayleigh wave velocity is about 92% of the shear wave velocity and is dependent on Poisson's ratio for isotropic conditions as shown in Figure 4.2.

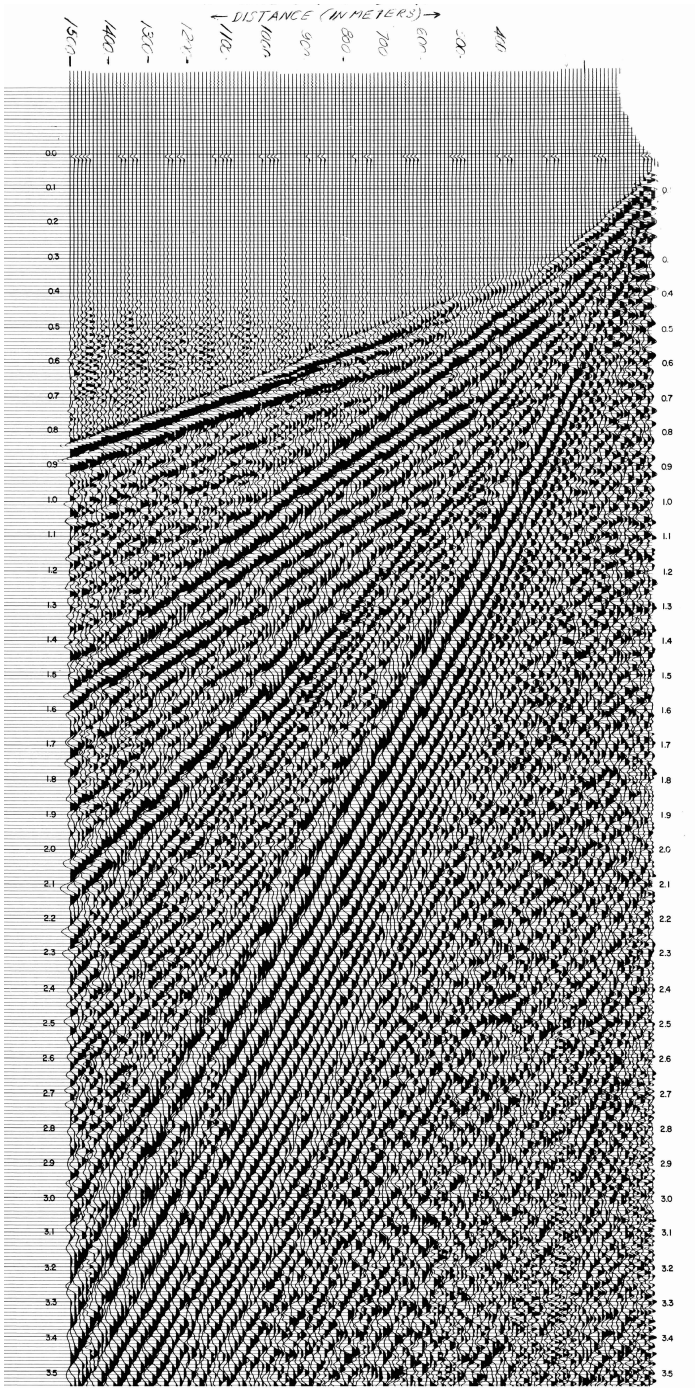

Figure 4.4 Walk-away noise spread displaying upward curvature of Rayleigh waves due to different modes. The x-axis is offset from 100 m to 1500 m in 100 m intervals. The y-axis is two-way-travel-time from 0 s to 3.5 s in 0.1 s intervals. This is an exploration industry example from an impulsive source of unknown origin.

4.3 SEISMIC PROFILES AND VELOCITY ESTIMATES: VERTICAL RECEIVERS

Seismic profiles for the vertical receiver are shown in Figure 4.5 through Figure 4.7. These correspond to Lines 1, 2, and 3, respectively. Line 3 is approximately along the direction of fractures, so elementary considerations of fracture effects on velocity would lead one to expect higher velocities for all wave types (except SH) along this direction. The vertical receiver observing waves generated by a vertical source is the most common seismic record and is sometimes called a P wave profile, though it records many other wave types. Other arrivals include SV and Rayleigh waves. Wave arrivals of interest are indicated on each profile with colors corresponding to the waves interpreted to be arrivals labeled in Figure 4.3. Velocities from slopes and corresponding wavelengths are presented in Table 4.2. Uncertainty is assigned based on repeated estimates using the wave-picking algorithm that is part of the Seismic Processing Workshop (SPW) processing package. The error in velocity measurements represents the change in velocity expected for a given arrival based on picking accuracy. Error was obtained by re-picking each arrival at least six times and determining the variation in velocity.

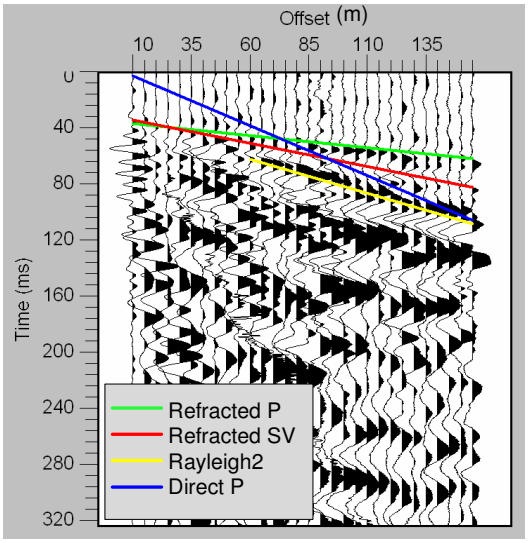

Figure 4.5 Seismic data profile with interpretation for Line 1 at N13W, vertical receiver component.

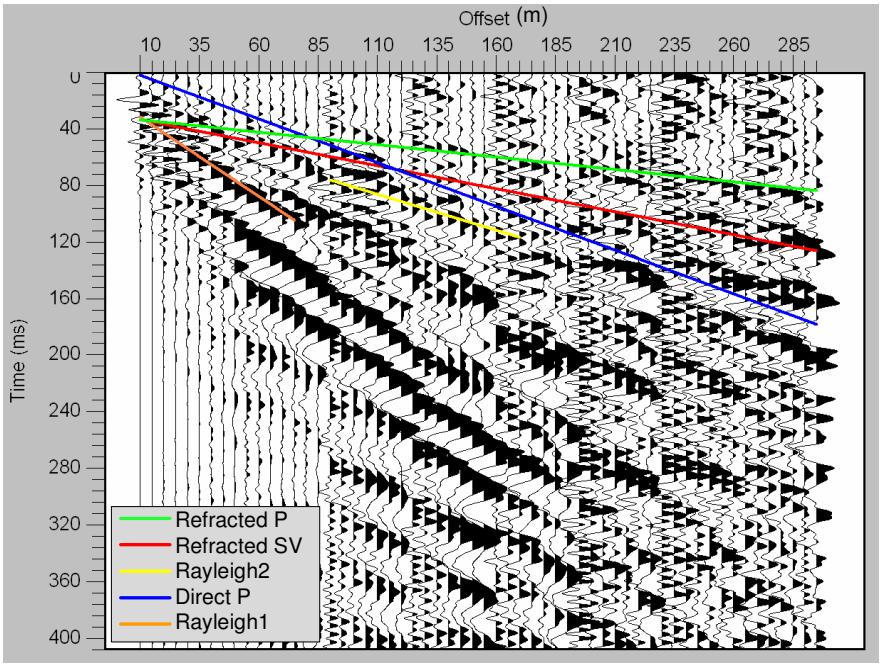

Figure 4.6 Seismic data profile with interpretation for Line 2 at N88E, vertical receiver component.

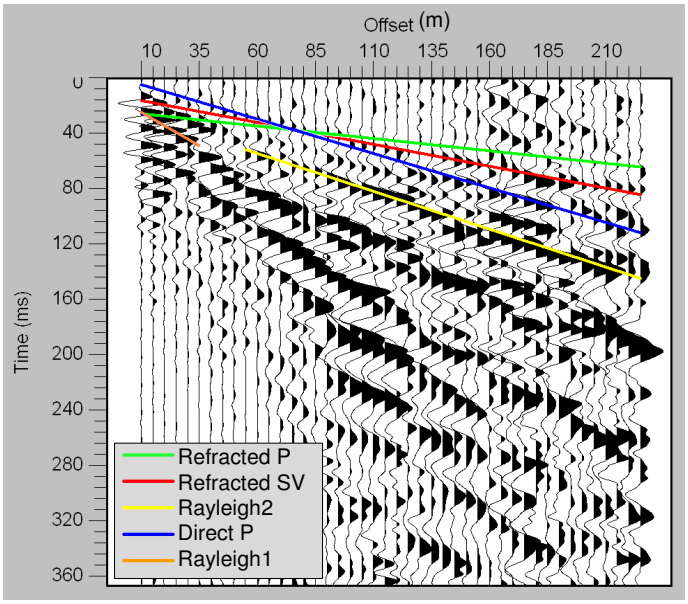

Figure 4.7 Seismic data profile with interpretation for Line 3 at N30E, vertical receiver component.

The direct P1 wave (blue) is the first arriving energy at near-offsets on the seismograms. This wave is most clearly indicated on Line 3 and is barely distinguishable on Line 1. The velocity of this wave is fastest for Line 3 and slows from Line 2 to Line 1 as expected from theory for unsaturated conditions as the angle to the fracture normal decreases. As a reminder from Chapter 2, the primary strike of the fractures measured at Stoneledge Quarry is at N35E. The refracted P2 wave (green) is the first arriving energy at far-offsets on the seismograms. The velocity is fastest for Lines 1 and 3 and slows slightly on Line 2 as expected from theory for saturated conditions. The second arrival identified at far-offsets is the refracted SV2 wave (red). The velocity of this wave is fastest for Line 3 and slows from Line 2 to Line 1 as expected from theory for saturated conditions as the angle to fracture normal decreases. The SV waves have smaller amplitudes and lower frequencies than the P waves.

Table 4.2 Wave velocities for the arrivals on the vertical receiver components.

	Sledgehammer Data	**P1**	**P2**	**SV2**	**Rayleigh1**	**Rayleigh2**
Line1 N13W	**Velocity (m/s)**	1399 ± 14	5740 ± 186	3026 ± 58	n/a	2121 ± 69
	Wavelength (m)	90	290	300	n/a	60
Line2 N88E	**Velocity (m/s)**	1606 ± 11	5700 ± 116	3095 ± 35	878 ± 25	1920 ± 48
	Wavelength (m)	160	380	210	30	50
Line3 N30E	**Velocity (m/s)**	2004 ± 25	5733 ± 151	3175 ± 52	960 ± 44	1834 ± 20
	Wavelength (m)	130	290	320	30	50

In all three seismic profiles, the highest amplitudes and lowest frequencies are associated with surface waves. With a single layer over a half-space, there may be multiple surface wave types or modes. As wavelengths become less than the layer thickness, one anticipates that a simple Rayleigh wave in the upper layer will be visible. At much longer wavelengths, a Rayleigh wave including the effect of the half-space will be observed. The surface waves observed in Figure 4.5 through Figure 4.7 have wavelengths around 30 m at near-offsets and 50 m to 60 m at far-offsets. The 30 m wavelengths are on the order of the thickness of the upper layer, presented below in section 4.5. The surface wave is effectively guided within this upper layer resulting in a strong refraction and significantly decays in amplitude at deeper depths (further offsets). The 50 m to 60 m wavelengths are about twice the thickness of the upper layer, therefore would not be influenced significantly by the upper layer. Instead these longer wavelengths are influenced by the half-space. From these considerations, I interpret the slower, near-offset arrivals to be the Rayleigh1 wave (orange) traveling at the speed of the upper layer and the faster, far-offset arrivals to be the Rayleigh2 wave (yellow) traveling at the speed of the half-space. Rayleigh waves in the half-space are measured around offsets of 155 m for consistency because this is the shortest acquisition line.

Lines 2 and 3 show evidence of two different surface wave modes that can be interpreted in a way that is consistent with the single layer over a half-space model. Line

1 surface waves are much less organized and the lower velocity mode (around 900 m/s) is not evident. The reason for this is not known. The high amplitude, low frequency surface wave arrivals (orange and yellow) in Figure 4.5 through Figure 4.7 are mildly dispersive. The orange arrivals at near-offsets are traveling at speeds expected for the upper layer and the yellow arrivals at far-offsets are traveling near the expected half-space Rayleigh speed. The upper layer speed is 879 m/s and 960 m/s in Lines 2 and 3, respectively. Its absence in Line 1 could be interpreted as a lack of this low speed layer, but there may be other explanations including changes in depositional units or other causes. The higher wave speed along Line 3 is consistent with general predictions of fracture anisotropy that the effective shear modulus (which is known to dominate Rayleigh wave speed) is greatest for shear propagation parallel to fracture strike.

4.4 SURFACE WAVE ANALYSIS

The surface wave arrivals can be examined for consistency with interpretation of P and S wave arrivals that have been used to infer layer velocities via conventional refraction methods. Further investigation of surface wave arrivals may yield additional information about anisotropy, but since the theory of surface waves in a vertically fractured material does not appear in the literature, the present discussion is limited to an evaluation of modal propagation in isotropic layers and a qualitative comparison with observed arrivals on Line 2.

The observation from Line 2 (Figure 4.6) is that there are two distinct surface wave arrivals with phase velocities around 878 m/sec (frequency range 25 - 35 Hz) and 1920 m/s (frequency range 50 - 60 Hz). For a single low speed layer over a half-space, the phase velocity curves (dispersion curves) are found by evaluating the expression given by Ewing et al., (1957). For the parameters shown in the figure (velocities determined from Line 2, assumed density of 2.0 and assumed shear velocity in Layer 1 of

900 m/s) the dispersion curves are shown in Figure 4.8. The general appearance is that there are several modes possible, whose phase velocity approaches the Rayleigh wave speed of the low speed layer (around 830 m/s) as wavelengths become small and frequency increases. In the 30 - 40 Hz range, the fundamental mode (left most curve) is dominantly at the Rayleigh wave speed of the low speed layer. The first higher mode (next one to the right) has a phase velocity at 2000 - 1500 m/s in this frequency range. These are consistent with values from observed surface waves on Line 2. That is, the 878 m/s arrival is interpreted as the fundamental mode, while the 1920 m/s arrival is interpreted as the first higher mode. Also, there is general consistency with layer thickness and velocities of the low speed layer and the half-space.

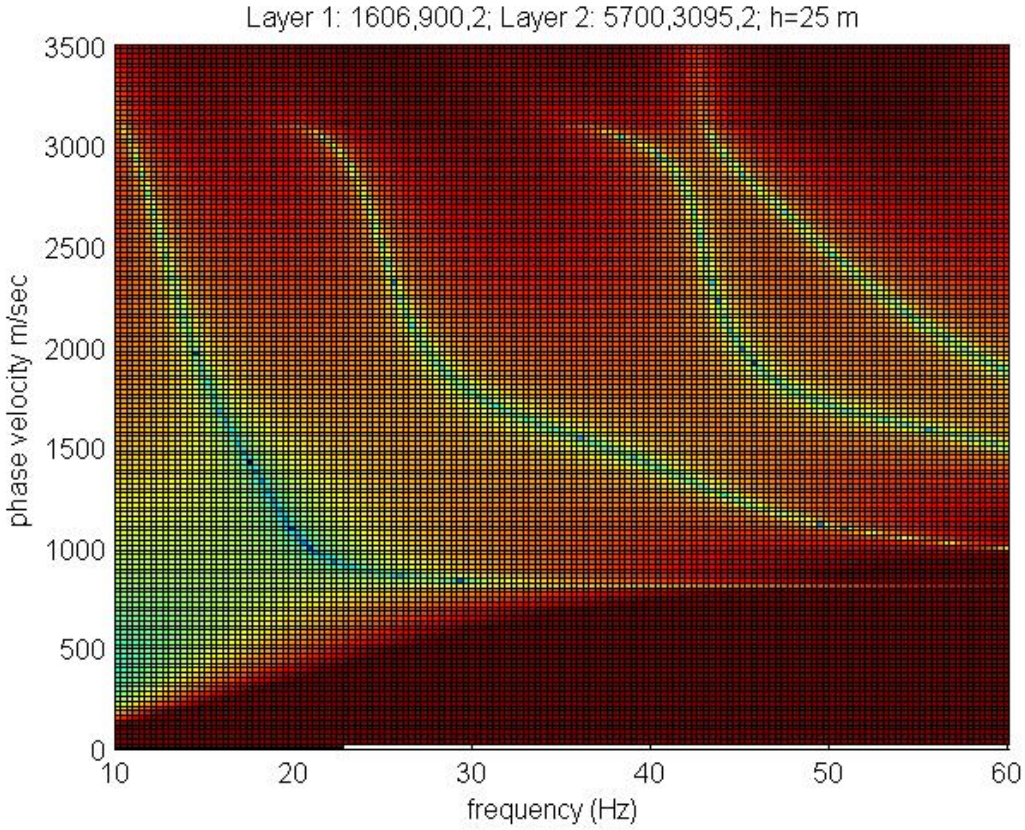

Figure 4.8 Dispersion curves from Ewing et al. (1957, Equation 4-202) showing the logarithm of the absolute value. The minima of the curves are near-zero values corresponding to modal propagation.

4.5 SEISMIC PROFILES AND VELOCITY ESTIMATES: REMAINING COMPONENTS

Here I examine inline and crossline profiles for the vertical sledgehammer source to determine whether they add additional information. For isotropic materials, the inline profile is expected to contain P and SV waves as well as Rayleigh-type surface wave arrivals. The crossline profile may contain P and S arrivals and surface waves, depending on layer geometry. The inline and crossline receiver synthetics for the model in Figure 4.1 for a vertical source component are shown in Figure 4.9 and Figure 4.10, respectively

for a line of geophones oriented at a 0° angle with the fracture normal (perpendicular to fracture strike).

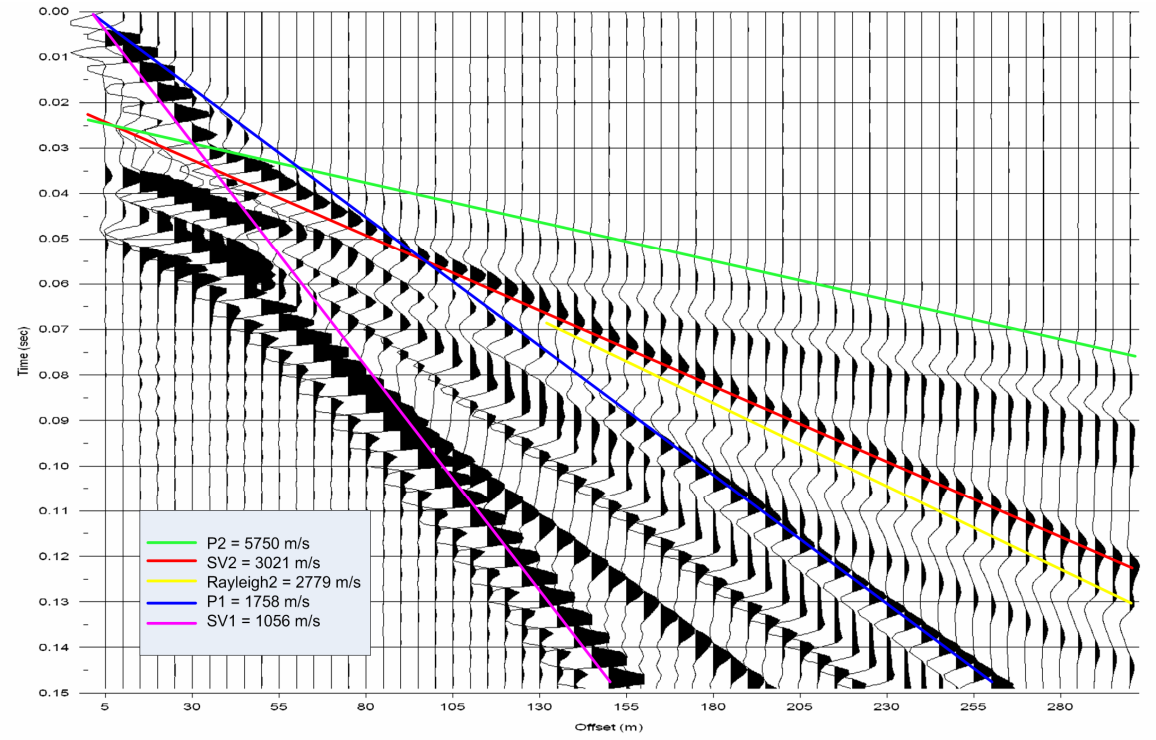

Figure 4.9 Synthetic seismic profile for the vertical source, inline receiver component line of geophones oriented at 0° with the fracture.

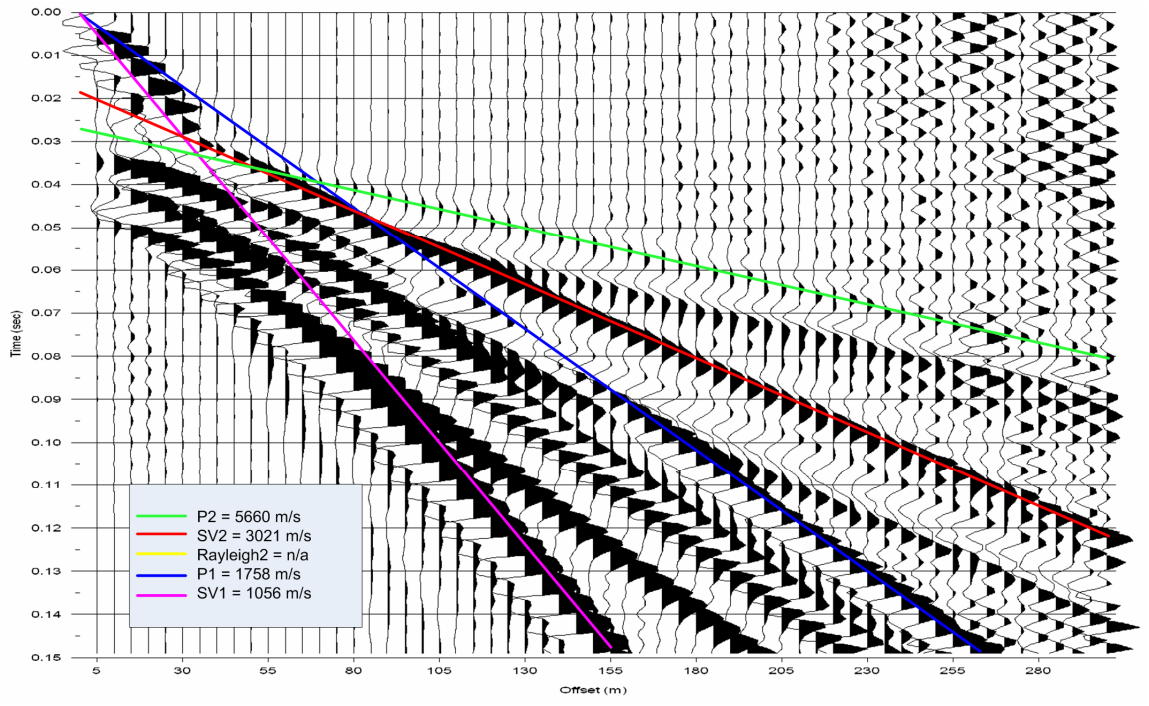

Figure 4.10 Synthetic seismic profile for the vertical source, vertical receiver component line of geophones oriented at 90° with the fracture normal.

The velocity of P1 is the same for the inline and crossline receiver components and is less than the input velocity by an amount expect from theory for 5% fracture density parallel to the fracture normal. The velocity of P2 in Figure 4.9 is the same as the input velocity, which is expected for saturated conditions parallel to the fracture normal. The polarity of P2 on the inline component is reversed compared to the vertical and crossline receiver components. The velocity of P2 is slightly slower in Figure 4.10 due the change in angle with fracture normal caused by the crossline receiver direction. The velocities of S1 and S2 are the same for the inline and crossline receiver components and are less than the input velocity by an amount expect from theory for 5% fracture density parallel to the fracture normal. The shear waves do not split at angles parallel to the fracture normal, therefore, SV and SH travel at the same speed at this orientation (indicated only as SV). The Rayleigh wave responding to the lower medium (at far-

offsets) has a velocity of 92% of the shear wave on the inline component as expected from theory. The Rayleigh wave is not present on the crossline component.

Significant arrivals were picked on inline and crossline observed seismograms as indicated in Figure 4.11 through Figure 4.13. The corresponding velocities are presented in Table 4.3. The red lines on the profiles have velocities similar to the SV velocities from the vertical components, so these arrivals are interpreted to be the SV wave. The presence of inline directed energy on the crossline receiver component may be due to imprecision in geophone orientations, anisotropy, or cross talk between receivers (Lawton, 1990). The light blue arrival in Figure 4.11 b) has the velocity of sound in air so it is assumed to be the air wave. The orange arrival in Figure 4.12 a) has a velocity similar to the velocity of the Rayleigh wave at near-offsets. This arrival also has high amplitudes and low frequencies indicative of surface waves and is interpreted to be the Rayleigh wave traveling at the upper layer speed. All remaining arrivals in purple have not been interpreted. The seismograms may include out-of-line reflections of various wave types.

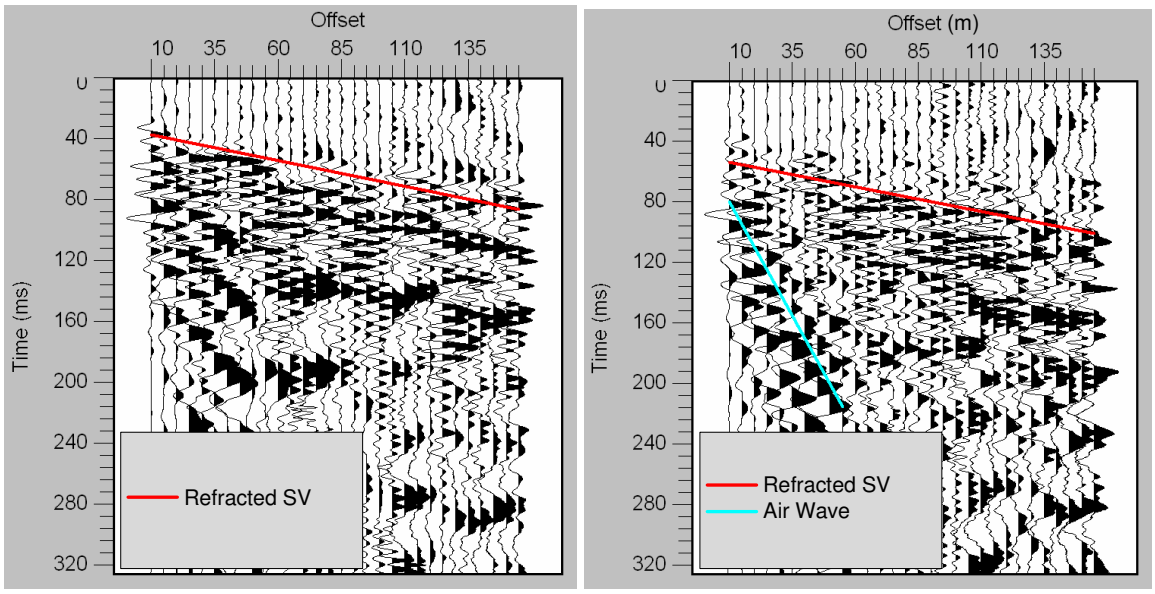

(a) (b)

Figure 4.11 Seismic data profile with interpretation for Line 1 at N13W, a) inline and b) crossline receiver components.

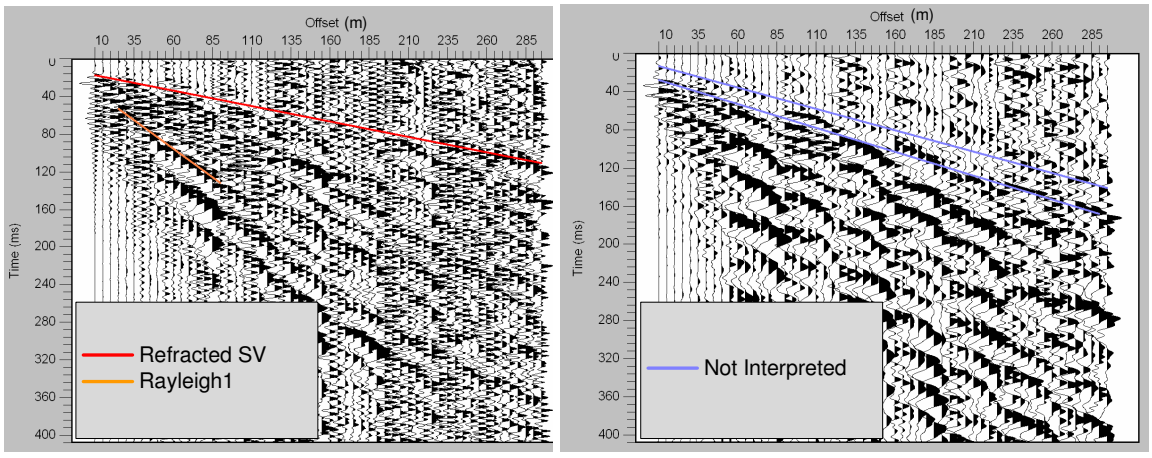

(a) (b)

Figure 4.12 Seismic data profile with interpretation for Line 2 at N88E, a) inline and b) crossline receiver components.

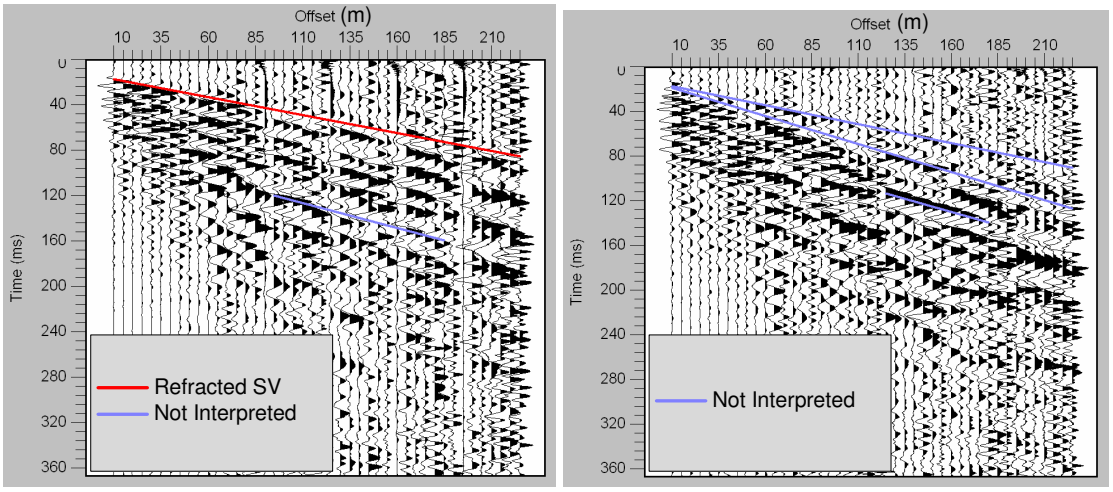

(a) (b)

Figure 4.13 Seismic data profile with interpretation for Line 3 at N30E, a) inline and b) crossline receiver components.

Table 4.3 Wave velocities for the arrivals on the inline and crossline receiver components.

Sledgehammer Data	Receiver Component		SV2	Air	Rayleigh1	Other
Line1 N13W	Inline	Velocity (m/s)	3026	n/a	n/a	n/a
	Crossline	Velocity (m/s)	3026	332	n/a	n/a
Line2 N88E	Inline	Velocity (m/s)	3074	n/a	884	n/a
	Crossline	Velocity (m/s)	n/a	n/a	n/a	2243 & 2006
Line3 N30E	Inline	Velocity (m/s)	3175	n/a	n/a	2215
	Crossline	Velocity (m/s)	n/a	n/a	n/a	2867, 1984, & 2200

4.6 WATER TABLE DEPTH ESTIMATES

To determine if fractures are filled with air or water, the depth to the water table is estimated. Anisotropy theory predicts that the depth of the water table should correspond to an abrupt increase in P wave velocities and the observed velocity change should be diagnostic of fracture density. Depth to the water table can be calculated from intercept time or crossover distance using standard travel time interpretation formulas for flat-lying layers, as appropriate in this situation. The crossover distance observed on the synthetics in Figure 4.3 is at 66.5 m corresponding to a water table depth of 23.2 m. This is slightly different from the model layer depth of 25 m but the synthetic seismogram program source and receivers are actually located at 1 m depth, which will change arrival times slightly. However, depth to the interface calculated from the intercept time of the refracted P wave (0.237 s) is very nearly 25.0 m.

Water table depth estimates from observed seismogram intercept times and crossover distances are shown in Table 4.4. Differences in water table depth among different acquisition lines may be due to actual variations in the water table surface at the

time of data acquisition, slight variations in ground surface elevations among acquisition lines, or both. Water table depths measured from the seismic data are roughly consistent with visual observations of the water table on the floor of Stoneledge Quarry.

Table 4.4 Results of water table depth analysis.

Sledgehammer Data	Intercept time (s)	Depth (m) from intercept time	Crossover distance (m)	Depth (m) from crossover distance
Line 1	0.03698	26.7	73	28.5
Line 2	0.03255	27.2	83	31.1
Line 3	0.02644	28.3	77	26.7

4.7 FRACTURE DENSITY ESTIMATES

Fracture density is the parameter used to develop theoretical predictions of velocity anisotropy in a fractured medium. The time difference between the S1 and S2 arrivals measures average anisotropy along the raypath described in Chapter 3, section 3.3. Equation 3.5 allows an estimate of fracture density from observed anisotropy measured from the seismic data and a value for Poisson's ratio for unfractured conditions. Velocity depends upon the incidence angle of the wave relative to the fracture normal; therefore the angle of incidence must be taken into account. At 90^{o} incidence to fracture normal, seismic velocities are closest to unfractured conditions as shown in Figure 3.2 through Figure 3.5 in Chapter 3. At this angle of incidence, traditional notions of SV and SH wave velocities may be applied. Assuming that dominant fracture orientation is at N35E, as determined from field measurements, the acquisition angle relative to the fracture normal for Lines 1 through 3 are 8^{o}, 37^{o}, and 85^{o}, respectively. This means that velocities from Line 3 should be closest to unfractured conditions and can be used in estimating expected velocities along Lines 1 and 2 for a specified fracture density. Velocities from the vertical receiver are used to estimate fracture density. Velocities from the other receiver components are comparable.

Line 3 P and SV wave velocities are used to calculate Vp/Vs and Poisson's ratio. SH velocity is required to calculate γ, which when combined with Poisson's ratio in Equation 3.5, gives fracture density. SV velocity from Line 1 is used as a proxy for SH velocity, because SV equals SH velocity at 0^{o} incidence (Line 1 conditions) and SH velocity at 0^{o} equals SH velocity at 90^{o} (Line 3 conditions) as shown in Figure 3.4 and Figure 3.5 in Chapter 3. In this calculation, velocities of the saturated half-space are used to estimate fracture density from Equation 3.5 because shear wave arrivals in the upper, unsaturated layer were not identified in the seismograms. Table 4.5 shows the values used to obtain fracture density using Equation 3.5.

Table 4.5 Fracture density estimates from saturated half-space P and S velocities

Sledgehammer Data	Saturated Half-space
Vp (m/s)	5733
Vsv (m/s)	3175
Vsh (m/s)	3026
Vp/Vs	1.81
Poisson's Ratio	0.279
γ	0.049
Fracture Density	0.044

A second approach to fracture density estimation comes from a plot of calculated velocity versus angle with respect to fracture normal for various fracture densities such as in Figure 3.2 through Figure 3.5. Theoretical curves with velocities listed in Table 4.6 from observed seismograms are shown in Figure 4.14 through Figure 4.16. Predictions for fracture densities of 0%, 1%, 5%, and 10% are calculated from theory. The fracture densities of 4.4% from Table 4.5, 5% from Figure 4.14, 3% from Figure 4.15, and 5% from Figure 4.16 at Stoneledge Quarry are within the confidence interval calculated from field scan line measurements (0.2 to 5%).

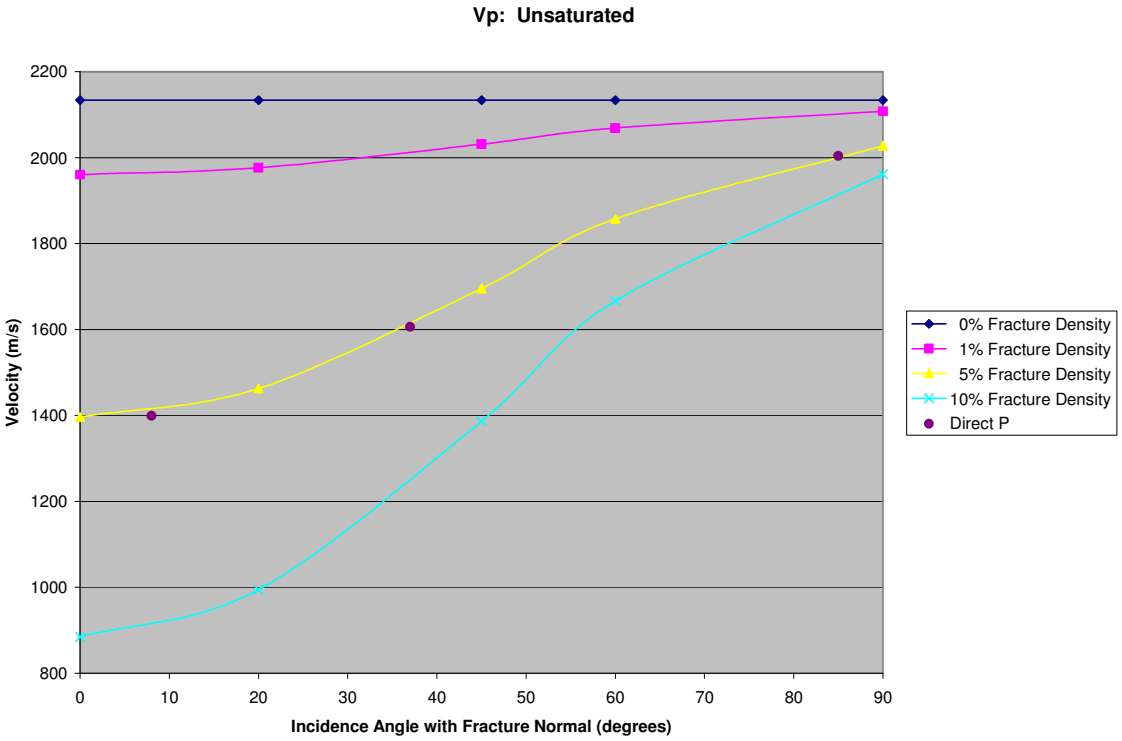

Figure 4.14 Velocities for the direct P wave at different azimuths. Fracture density in the unsaturated upper layer is about 5% based on this graph.

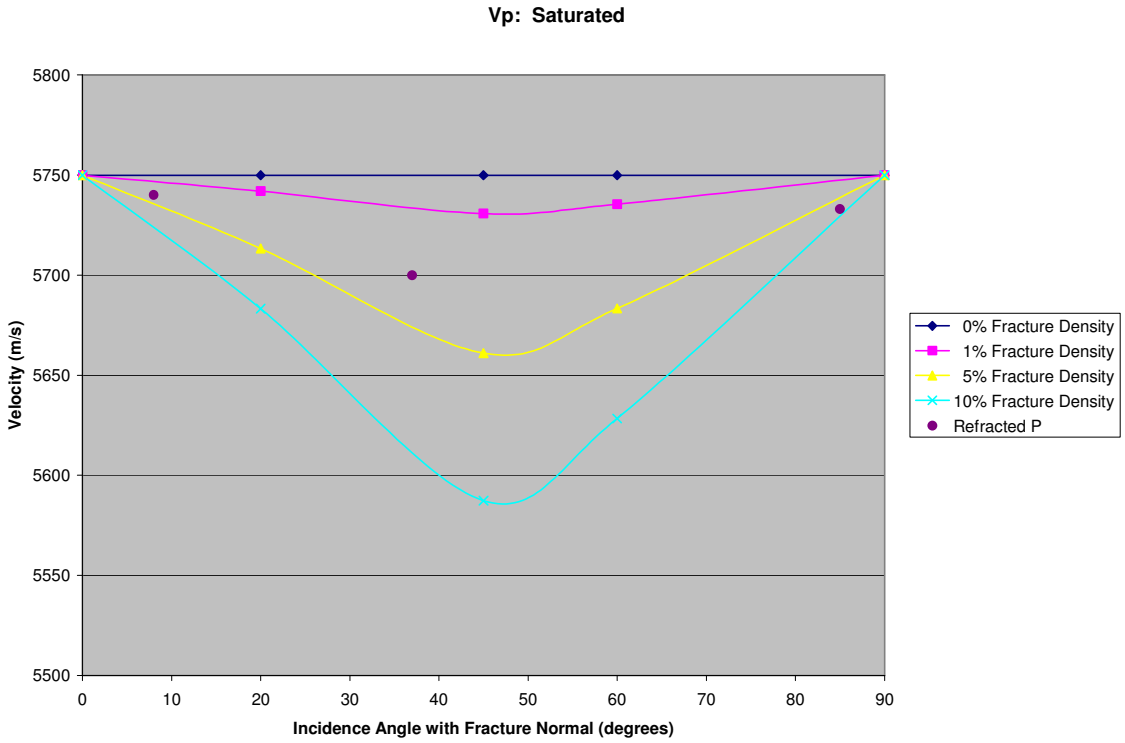

Figure 4.15 Velocities for the refracted P wave at different azimuths. Fracture density in the saturated half-space is about 3% based on this graph.

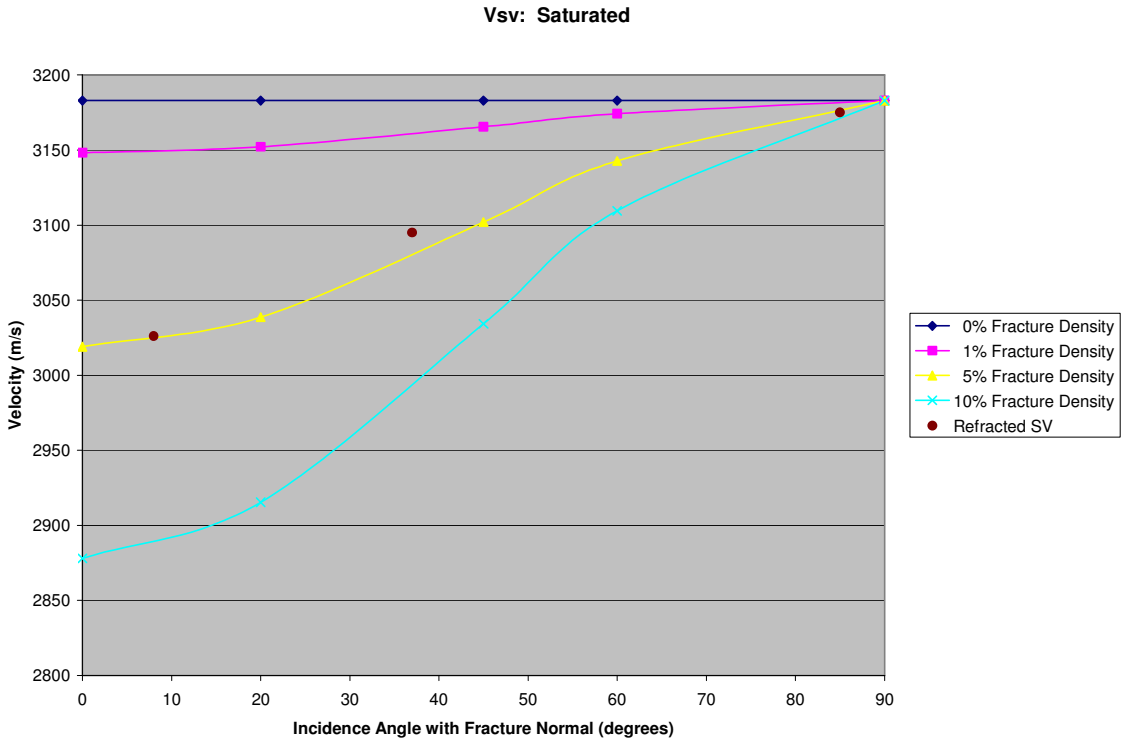

Figure 4.16 Velocities for the refracted SV wave at different azimuths. Fracture density in the saturated half-space is about 5% based on this graph.

Table 4.6 Values from Stoneledge Quarry seismic data plot in Figure 4.14 through Figure 4.16.

Seismic Acquisition Line	Incidence Angle with Fracture Normal	Direct P Velocity (m/s)	Refracted P Velocity (m/s)	Refracted SV Velocity (m/s)
Line 1	8°	1399 ± 14	5740 ± 186	3026 ± 58
Line 2	37°	1606 ± 11	5700 ± 116	3095 ± 35
Line 3	85°	2004 ± 25	5733 ± 151	3175 ± 52

Additionally, velocity anisotropy is evident in the Rayleigh wave arrivals. The Rayleigh waves exhibit strong evidence for anisotropy because their arrivals are less ambiguous than the body wave arrivals. High amplitudes and low frequencies make the surface wave arrivals easy to detect in the seismic record. Rayleigh wave velocities measured from the seismic data also have fairly low error. The variation in Rayleigh

wave velocity with azimuth is significant because it is within the range of velocity variation in the body waves. The percent variation in velocity among the three acquisition lines for the waves detected in the seismic data are shown in Table 4.7. Rayleigh wave speeds are known to be most sensitive to shear (SV) speeds in a homogeneous material, implying that these can be taken as proportional to SV velocities and the fractional change used as another measure of anisotropy. However, as shown in Table 4.7, the percent change in velocity of Rayleigh waves is much higher than SV waves, implying that the Rayleigh wave may not fit this line of reasoning for anisotropic conditions.

Table 4.7 Percent change in velocities measure from the sledgehammer source seismic data at Stoneledge Quarry.

Velocity variation between:	Direct P (%)	Refracted P (%)	Refracted SV (%)	Rayleigh1 (%)	Rayleigh2 (%)
Lines 1 & 2	14.8	0.7	2.3	n/a	10.5
Lines 1 & 3	43.2	0.1	4.9	n/a	15.6
Lines 2 & 3	24.8	0.6	2.6	9.3	4.7

Finally, the increase in P velocity for the presumed unsaturated layer to the saturated half-space provides an additional measure of fracture density, given the only change in the medium is fracture saturation. For example, theory indicates that the increase in P wave velocity from unsaturated to saturated conditions at 5% fracture density for 0^{o} angle with fracture normal is about 15%. Lower fracture densities show smaller increases and higher densities show larger increases. However, taking the increase in P velocity in Line 1 from 1399 m/s for dry fractures to 5740 m/s for saturated fractures implies a fracture density of over 100%. This is obviously not possible. Other factors besides saturation are contributing to the low velocity of the upper layer and fracture density in the upper layer cannot be determined using this method.

4.8 CONCLUSIONS

Because Line 3 is oriented nearly parallel to the fracture strike, the velocities estimated on this line plus fracture density can be used to describe the conditions of the subsurface. Velocities from this direction correspond with conventional notions and velocities at other azimuths can be estimated by including fracture density. Based on this line of reasoning, the wave velocities at Stoneledge Quarry are about: 2004 m/s and 5733 m/s for P in the upper unsaturated layer and half-space, respectively; 3175 m/s for SV in the half-space; and 960 m/s and 1834 m/s for Rayleigh at near and far offsets, respectively. Fracture density is estimated between 3% and 5% based on velocity anisotropy. Field measurements of fracture density average about 1% with a confidence interval between 0.2% and 5%. The seismic estimates of fracture density are in the high range of the confidence interval from the field measurements but this may be due to the contribution of the matrix porosity. Seismic waves average the porosity of both the fractures and the matrix, so the higher fracture density could be due to matrix porosity. Seismic measurements are within the range of field measurements indicating that the two different methods of measuring fracture density may be relatable.

Thickness of the upper layer corresponds to the depth to the water table, which is between 26 and 31 m. Therefore, fractures above this depth are assumed filled with air and water-filled below. This is deeper than the rough estimate made from observations in the field (17.2 m) but reasonable considering wavelengths of about 90 m to 380 m. Additionally, part of upper layer may be saturated and the water table is somewhat shallower than indicated in seismic data (Bradford, 2002) as discussed in Chapter 3.

Variations in velocity for anisotropic conditions are functions of fracture density and incidence angle with the fracture normal as discussed in Chapter 3, section 3.3. Field measurements of fracture orientation are roughly parallel with seismic acquisition Line 3.

P velocities on this line are faster than those on Lines 1 and 2, which corresponds to velocities expected from theory for incidence angles of nearly 90° to the fracture normal or parallel to fracture strike. P wave velocities in the upper layer (direct P) decrease with decreasing angle from fracture normal for unsaturated conditions. P wave velocities in the saturated half-space (refracted P) decrease with decreasing angle from fracture normal to 45° then increase to 0°. SV wave velocities in the half-space (refracted SV) decrease with decreasing angle from fracture normal for saturated (and unsaturated) conditions. Rayleigh waves are controlled predominantly by the shear wave velocity and are expected to have similar behaviors under anisotropic conditions. Therefore, velocities for different wave types on Lines 1, 2, and 3, are consistent with theory and indicate the fracture orientation should be roughly parallel to Line 3 at N30E.

Other information gained from the seismic data includes lithology from Vp/Vs and Poisson's ratio. Laboratory data show Vp/Vs ranges from 1.84 to 1.99 for limestone and from 1.78 to 1.84 for dolomite (Domenico, 1984). Additionally, laboratory data show Poisson's ratios range from 0.29 to 0.33 for limestone and from 0.27 to 0.29 for dolomite (Domenico, 1983). Vp/Vs is 1.81 and Poisson's ratio is 0.279 from this data set. The seismic data indicate that the medium is dolomite, which is in accordance with Stoneledge Quarry being in the dolomitic member of the Edwards Group.

Finally, the inline and crossline receiver components provide other data in addition to the conventional vertical component. These components did not provide information that was not already obtained form the vertical receiver component. However, these components, especially the inline receiver, did confirm velocities of waves identified on the vertical component. I believe this provides additional validity to the velocities of the arrivals. Though some arrivals in this data may be ambiguous, the confirmation of their velocities on other components makes them more credible.

Therefore, in areas where wave arrivals are ambiguous due to interference from waves not being studied, additional receiver components may decrease the ambiguity.

Chapter 5: Estimating Velocity Anisotropy and Fracture Properties: Vibroseis Source

5.1 INTRODUCTION

9C data from a Vibroseis source are used to estimate velocity anisotropy and depth to the water table at Stoneledge Quarry. Fracture parameters of filling material, orientation, and fracture density are estimated from the data. In section 5.2, I present the three Vibroseis records corresponding to the 3C, vertical source hammer data in Chapter 4. In section 5.3, fracture filling material from estimates of depth to the water table is discussed. In section 5.4, I discuss the theory of shear wave splitting. In section 5.5, I analyze synthetic and observed data of matched components, most similar to traditional notions of SV and SH wave records. These include seismograms from inline and crossline sources recorded on inline and crossline receiver components, respectively. In section 5.6, I discuss Alford Rotation and use this analysis to estimate fracture orientation. In section 5.7, I estimate fracture density from the seismic data with conclusions in section 5.8. The Vibroseis source and related recording equipment are part of the NEES@UTexas facility sponsored by the National Science Foundation. The survey at Stoneledge Quarry was one of the field trials of this equipment during the development portion of the NEES equipment grant.

5.2 VERTICAL SOURCE COMPONENTS

First, I present the vertical source records because these are most directly comparable to the sledgehammer data set in Chapter 4. Velocity results should be similar to those in Chapter 4.

5.2.1 Vertical Receiver Component

Seismic profiles for vertical receivers are shown in Figure 5.1 through Figure 5.3 for Lines 1, 2, and 3, respectively. Line 3 is approximately along the direction of fractures, so elementary considerations of fracture effects lead one to expect higher velocities for all wave types (except SH) along this direction. Wave arrivals of interest are indicated on each profile with colors corresponding to arrivals labeled on the model in Figure 4.3. Velocities from slopes and corresponding wavelengths are presented in Table 5.1. Velocity estimates are comparable to those from the hammer source. Uncertainty is assigned from repeated estimates using the wave-picking algorithm that is part of the SPW processing package. Error was obtained by re-picking each arrival at least six times and determining the variation in velocity.

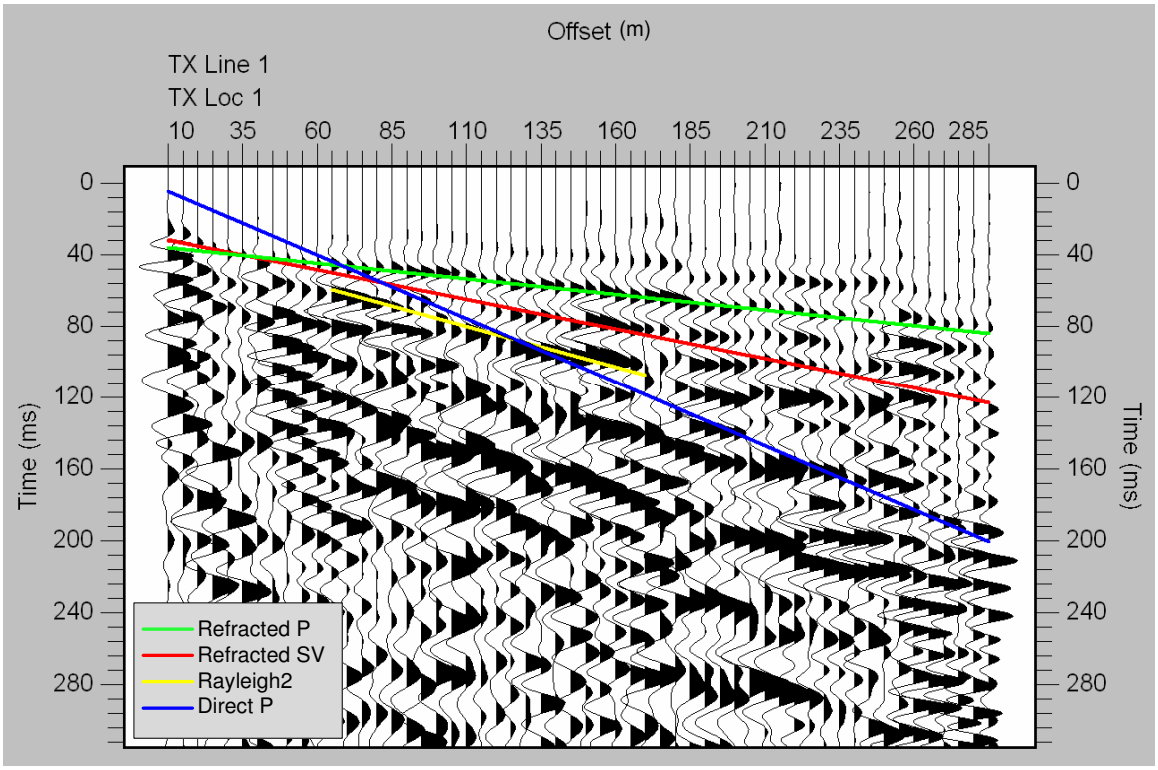

Figure 5.1 Seismic data profile with interpretation for Line 1 at N13W, vertical source, vertical receiver component.

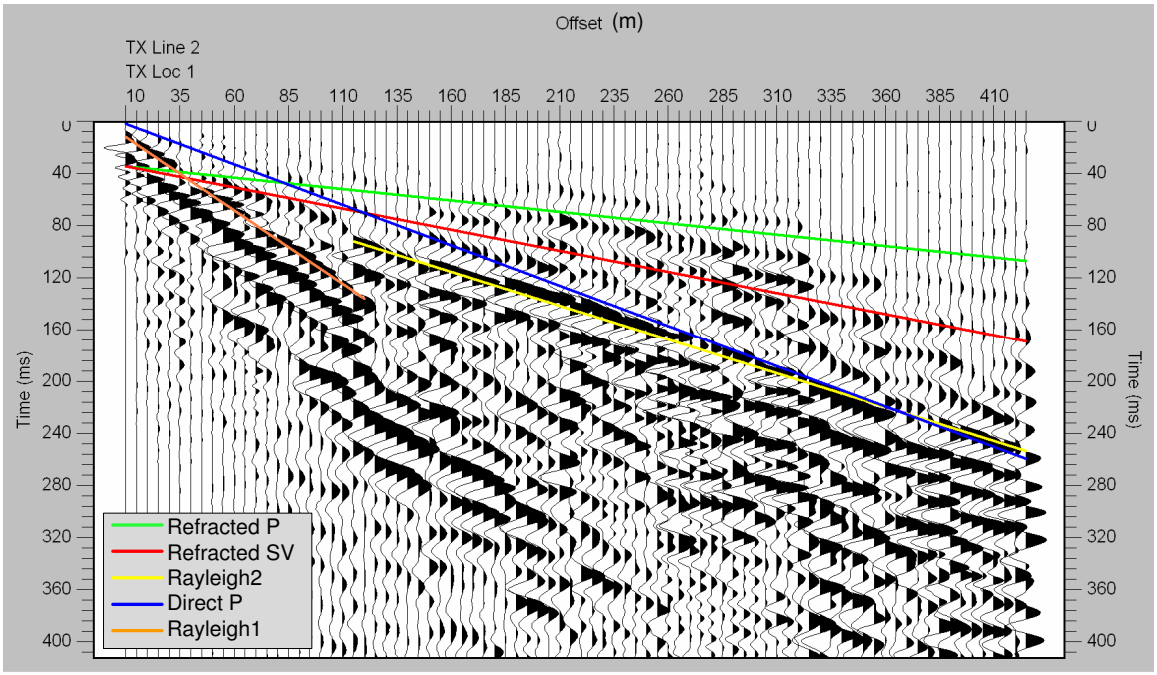

Figure 5.2 Seismic data profile with interpretation for Line 2 at N88E, vertical source, vertical receiver component.

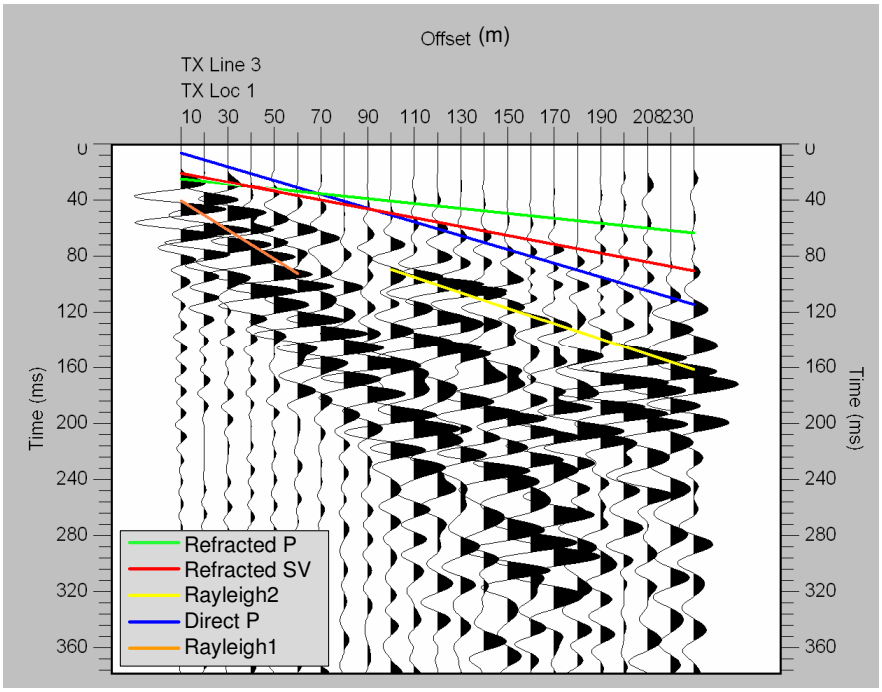

Figure 5.3 Seismic data profile with interpretation for Line 3 at N30E, vertical source, vertical receiver component.

The direct P wave (blue) is the first arriving event at near-offsets on the seismograms. This is clearest on Line 2 and barely distinguishable on Lines 1 and Line 3. The velocity of this wave is fastest for Line 3 and diminishes along Line 2 and Line 1 as expected from theory for unsaturated conditions as the angle to the fracture normal decreases. The primary strike of the fractures measured at Stoneledge Quarry is at N35E, generally along the direction of Line 3. The refracted P wave (green) is the first arriving event at far-offsets on the seismograms. The velocity of this wave is fastest for Lines 1 and 3 and slows slightly in Line 2 as expected from theory for saturated conditions. The second arriving energy identified in the seismograms at far-offsets is the refracted SV wave (red). The velocity of this wave is fastest for Line 3 and slows from Line 2 to Line 1 as expected from theory for saturated conditions as the angle to the fracture normal

decreases. The SV waves have smaller amplitudes and lower frequencies than the P waves.

Table 5.1 Wave velocities and wavelengths for the arrivals on the vertical source, vertical receiver components.

	Vibroseis Data	**P1**	**P2**	**SV2**	**Rayleigh1**	**Rayleigh2**
Line1 N13W	**Velocity (m/s)**	1397 ± 15	5739 ± 122	3049 ± 36	n/a	2100 ± 46
	Wavelength (m)	120	380	200	n/a	50
Line2 N88E	**Velocity (m/s)**	1616 ± 11	5700 ± 27	3091 ± 77	887 ± 8	1931 ± 14
	Wavelength (m)	160	380	210	20	50
Line3 N30E	**Velocity (m/s)**	2011 ± 28	5729 ± 167	3171 ± 47	960 ± 21	1835 ± 22
	Wavelength (m)	130	290	320	20	50

In all three seismic profiles, the highest amplitudes and lowest frequencies are associated with surface waves. With a single layer over a half-space, there may be multiple surface wave types or modes. As wavelengths become comparable to or smaller than the layer thickness, one anticipates that a simple Rayleigh wave in the upper layer will be visible. At much longer wavelengths, a wave corresponding to a Rayleigh wave in the half-space will be observed. The surface waves observed in Figure 5.1 through Figure 5.3 have wavelengths around 20 m at near-offsets and 50 m at far-offsets. The 20 m wavelengths are on the order of the thickness of the upper layer, presented below in section 5.3. The 50 m wavelengths are about twice the thickness of the upper layer, therefore would be less influenced by the upper layer. From these considerations, I interpret the slower, near-offset arrivals to be Rayleigh1 (orange) for the upper layer and the faster, far-offset arrivals to be Rayleigh2 (yellow) for the half-space. Rayleigh wave speeds in the half-space are measured around offsets of 155 m for all three lines.

Lines 2 and 3 show evidence of two different surface wave modes that can be interpreted as consistent with the single layer over a half-space model. Line 1 surface waves are less organized and the lower velocity mode (around 900 m/s) is not evident.

The reason for this is not known. The high amplitude, low frequency surface wave arrivals (orange and yellow) in Figure 5.1 through Figure 5.3 are mildly dispersive. The orange arrivals at near-offsets are traveling at speeds expected for the upper layer and the yellow arrivals at far-offsets are traveling near the expected half-space Rayleigh speed. The upper layer speed is 887 m/s and 960 m/s in Lines 2 and 3, respectively. Its absence in Line 1 could be interpreted as a lack of this low speed layer, but there may be other explanations, including changes in depositional units or other causes. The higher wave speed along Line 3 is consistent with general predictions of fracture anisotropy that the effective shear modulus (which is known to dominate Rayleigh wave speed) is greatest for shear propagation parallel to fracture strike. Section 4.3 in Chapter 4 discusses Rayleigh waves and Rayleigh wave dispersion in more detail. Generally the conclusions from the Vibroseis source seismograms are similar to those obtained with the sledgehammer source.

5.2.2 Inline and Crossline Receiver Components

Significant arrivals were picked on the remaining two horizontal receiver components of each line for the vertical source component. Wave arrivals of interest are indicated on each profile in Figure 5.4 through Figure 5.6. The corresponding velocities are presented in Table 5.2. The green lines on the profiles have velocities similar to the P2 velocities from the vertical receiver components, so these arrivals are interpreted to be the P2 wave. The red lines on the profiles have velocities similar to the SV2 velocities from the vertical receiver components, so these arrivals are interpreted to be the SV2 wave. Orange and yellow arrivals have velocities similar to the Rayleigh velocities from the vertical receiver components, so these arrivals are interpreted to be the Rayleigh wave response at near- and far-offsets, respectively. These arrivals also have high amplitudes and low frequencies indicative of surface waves. All remaining arrivals in purple do not

correspond with any expected wave arrivals and are not analyzed. As discussed in Chapter 4, the presence of inline directed energy on the crossline receiver component may be due to imprecision in geophone orientations, anisotropy in the near surface, or cross talk between receivers (Lawton, 1990).

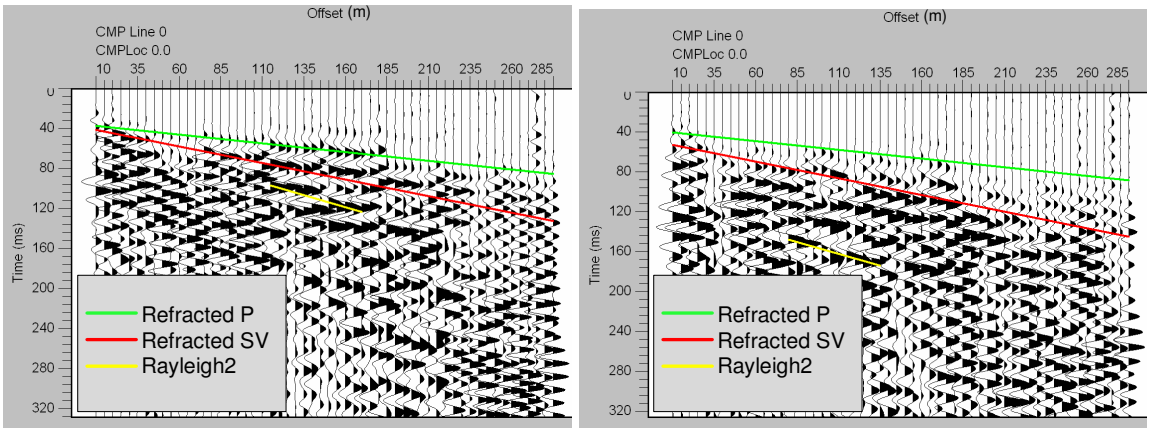

(a) (b)

Figure 5.4 Seismic profile with interpretation for Line 1 at N13W, vertical source, a) inline and b) crossline receiver components.

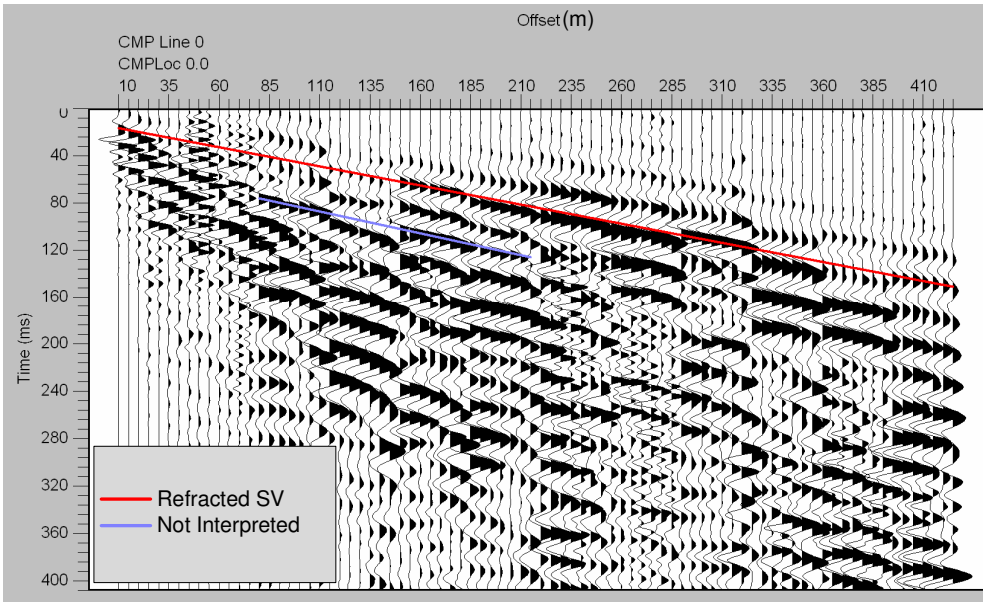

(a)

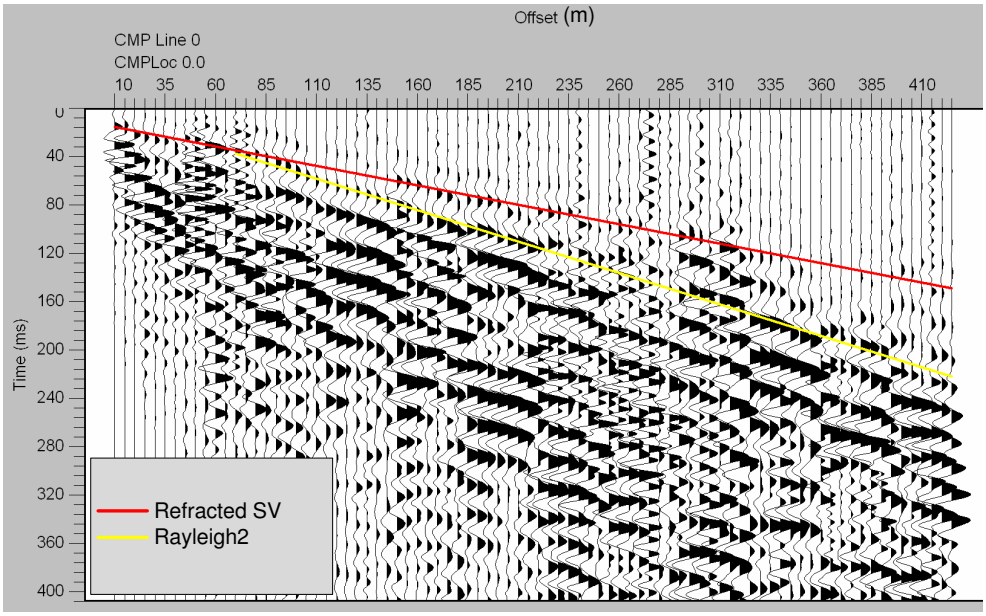

(b)

Figure 5.5 Seismic profile with interpretation for Line 2 at N88E, vertical source, a) inline and b) crossline receiver components.

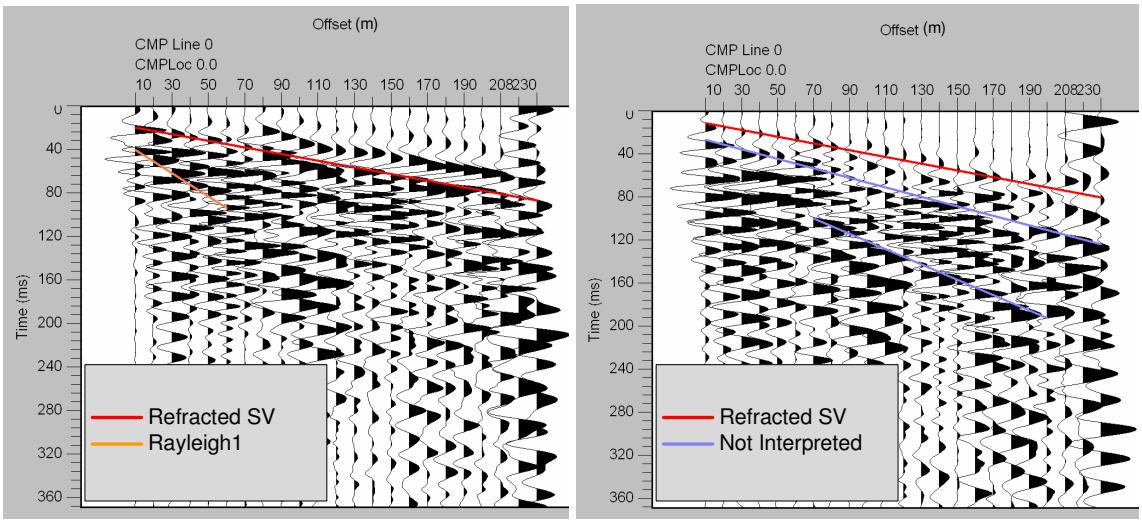

(a) (b)

Figure 5.6 Seismic profile with interpretation for Line 3 at N30E, vertical source, a) inline and b) crossline receiver components.

Table 5.2 Wave velocities for the arrivals on the vertical source, inline and crossline receiver components.

	Receiver Component		P2	SV2	Rayleigh 1	Rayleigh 2	Other
Line 1	**Inline**	Velocity (m/s)	5739 ± 42	3034 ± 53	n/a	2112 ± 43	n/a
	Crossline	Velocity (m/s)	5739 ± 42	3034 ± 35	n/a	2112 ± 48	n/a
Line 2	**Inline**	Velocity (m/s)	n/a	3088 ± 36	n/a	n/a	2700 ± 56
	Crossline	Velocity (m/s)	n/a	3088 ± 23	n/a	1925 ± 16	n/a
Line 3	**Inline**	Velocity (m/s)	n/a	3171 ± 63	960 ± 29	n/a	n/a
	Crossline	Velocity (m/s)	n/a	3168 ± 32	n/a	n/a	2271 ± 25 1371 ± 15

5.3 WATER TABLE DEPTH

Anisotropy theory predicts that the depth of the water table should correspond to an abrupt increase in P wave velocities and the observed velocity change should be

diagnostic of fracture density. Depth to the water table can be calculated from intercept time or crossover distance using standard travel time interpretation formulas for flat-lying layers, as appropriate in this situation.

Results of analysis using intercept time and crossover distance are shown in Table 5.3. As discussed in Chapter 4, differences to water table depth among different acquisition lines may be due to actual variations in the water table surface due to varying dates of the surveys, slight variations in ground surface elevations among acquisition lines, or both. Water table depths measured from the seismic data are roughly consistent with results from the hammer source data and with observations of water table evident at the floor of Stoneledge Quarry during the survey. Water levels were observed to be higher during Vibroseis source surveys relative to sledgehammer source surveys and this is reflected in the estimates.

Table 5.3 Results of water table depth analysis.

Vibroseis Data	Intercept time (s)	Depth (m) from intercept time	Crossover distance (m)	Depth (m) from crossover distance
Line 1	0.036	25.9	69	26.9
Line 2	0.034	29.0	81	30.2
Line 3	0.025	26.9	70	24.2

5.4 SHEAR WAVE SPLITTING

When a shear wave propagates through an anisotropic medium, the wave may split into two different shear waves, S1 and S2, which have orthogonal polarizations and different velocities [note that nomenclature in sections above connected numbers 1 and 2 with layer 1 and the half-space] (Lewis et al., 1991; Li and Mueller, 1997; Tatham and McCormack, 1991). Shear wave splitting is also referred to as birefringence. S1 is defined as the faster of the two waves and is polarized parallel to the dominant orientation of anisotropy. This is traditionally known as the SV wave in isotropic media

and may also be referred to as the $S_{//}$ (S-parallel) wave. S2 is the slower wave and is polarized perpendicular to the dominant orientation of anisotropy. This is traditionally known as the SH wave in isotropic media and may also be referred to as the $S_{\perp}$ (S-perpendicular) wave.

Figure 5.7 is a schematic illustration of shear-wave splitting with respect to direction for a transversely isotropic media. A shear wave entering an anisotropic region parallel to the direction of anisotropy splits into two or more fixed polarizations, which propagate in the same ray direction. These split phases propagate with different polarizations and different velocities. A shear wave entering an anisotropic region perpendicular to the direction of anisotropy will not split because both SV (S1) and SH (S2) polarizations will travel at the same speed (Tatham and McCormack, 1991).

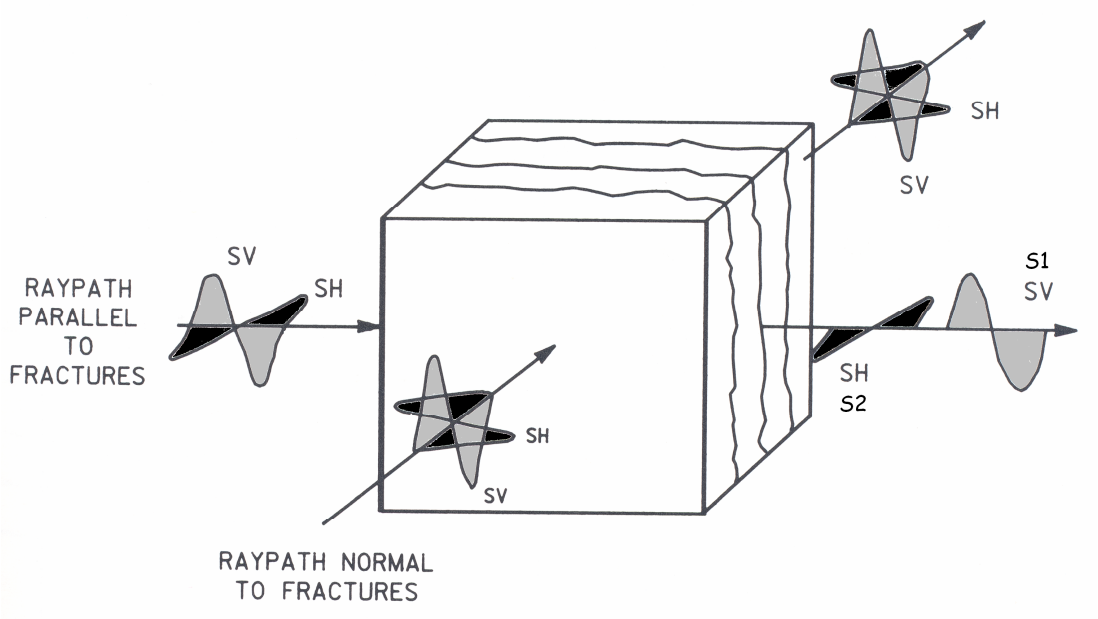

Figure 5.7 Schematic illustration of shear-wave splitting with respect to direction for a transversely isotropic media (Tatham and McCormack, 1991).

5.5 REMAINING DIAGONAL COMPONENTS

Inline source, inline receiver and crossline source, crossline receiver components are called SV and SH orientations, respectively, corresponding to conventional SV and SH wave data (Tatham and McCormack, 1991). Components that have matched source and receiver pairs are often referred to as the diagonal components.

5.5.1 Synthetic Seismograms

Synthetic seismic profiles were created as described in Chapter 3 and in Appendix B. The vertical source, vertical receiver component seismogram profile of a line of geophones 90° to the fracture normal (parallel to fracture strike) is presented in Chapter 4, Figure 4.3. Profiles of the inline source, inline receiver and crossline source, crossline receiver components at 90° to the fracture normal are presented in Figure 5.8. Shear wave velocities should have the greatest variability between these two profiles at this orientation. The faster of the split shear waves (S1) should arrive on the matched inline source, inline receiver (SV) components. The slower of the shear waves (S2) should arrive on the matched crossline source, crossline receiver (SH) components. Identified waves in Figure 5.8 are: a) refracted P (green), refracted SV (bright red), direct P (blue), and direct SV (bright pink), b) direct P (blue), refracted SH (dark red), and direct SH (pale pink). The slopes of these arrivals correspond well to the expected values from the model for 5% fracture density, as indicated in the figure. Hyperbolic moveout events are present in the synthetic profile corresponding to reflections from the interface. The waves in the synthetic profile are the dominant waves expected in the data from Stoneledge Quarry, except, as observed with sledgehammer source data in Chapter 4 and here below, the synthetics do not calculate events with the reverberant and dispersive nature of observed surface waves.

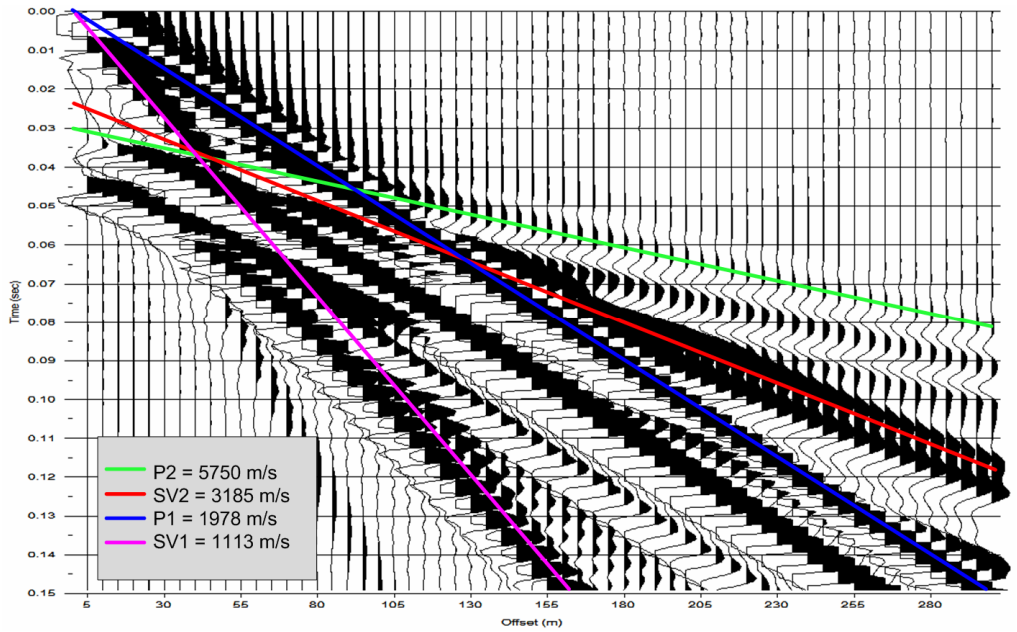

(a)

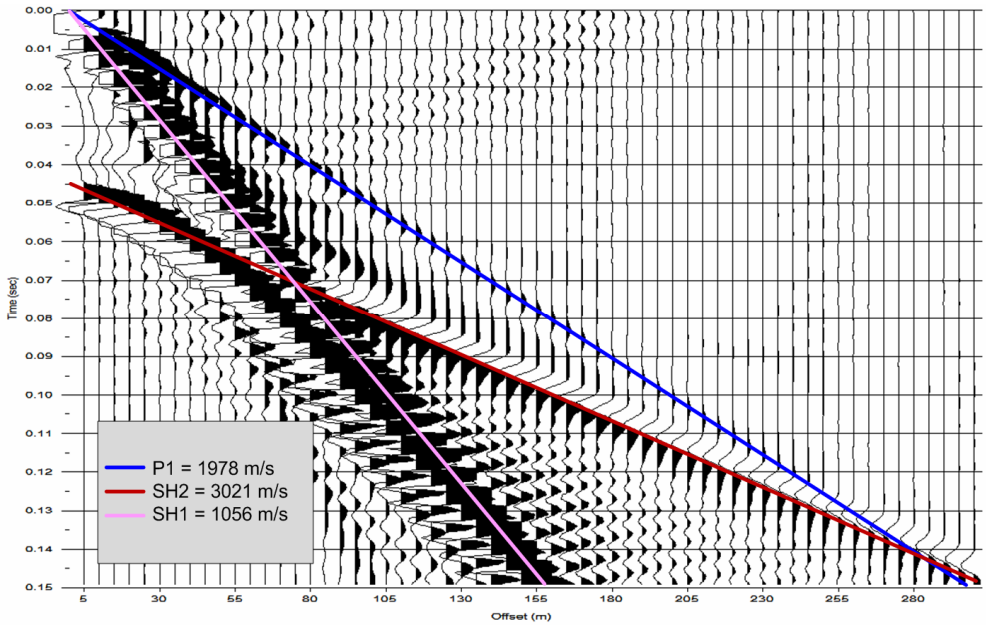

(b)

Figure 5.8 Synthetic seismic profiles for a) the inline source, inline receiver component and b) for the crossline source, crossline receiver component for a line of geophones oriented at 90° with the fracture normal for the model in Figure 4.1 with 5% fracture density.

5.5.2 Stoneledge Quarry Data

Significant arrivals were picked on matched pairs, inline and crossline observed seismograms, as indicated in Figure 5.9 through Figure 5.11. The corresponding velocities are presented in Table 5.4. The green lines on the profiles have velocities similar to the direct P wave velocities from the vertical components, so these arrivals are interpreted to be the P wave. The bright red lines on the profiles have velocities similar to the SV velocities from the vertical components, so these arrivals are interpreted to be the SV wave. The dark red lines on the profiles have velocities similar to the SH velocities expected from theory, so these arrivals are interpreted to be the SH wave. The orange arrivals have a velocity similar to the velocity of the Rayleigh wave at near-offsets. The yellow arrivals have a velocity similar to the velocity of the Rayleigh wave at far-offsets. These arrivals also has high amplitudes and low frequencies indicative of surface waves and interpreted to be the Rayleigh wave in the upper layer and half-space, respectively. The remaining arrival in purple (Figure 5.10 a) was not interpreted. They may include out-of-line reflections of various wave types.

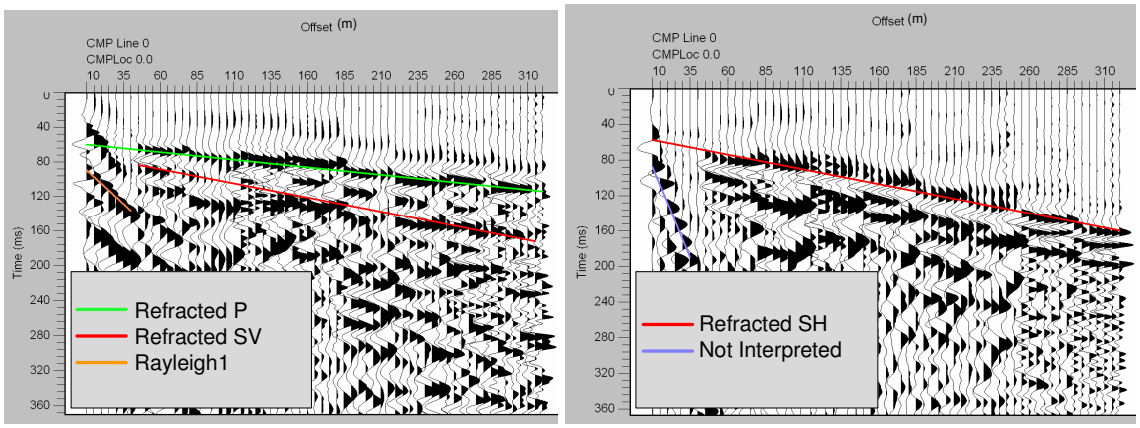

(a) (b)

Figure 5.9 Seismic profile with interpretation for Line 1 at N13W, a) inline source, inline receiver and b) crossline source, crossline receiver components.

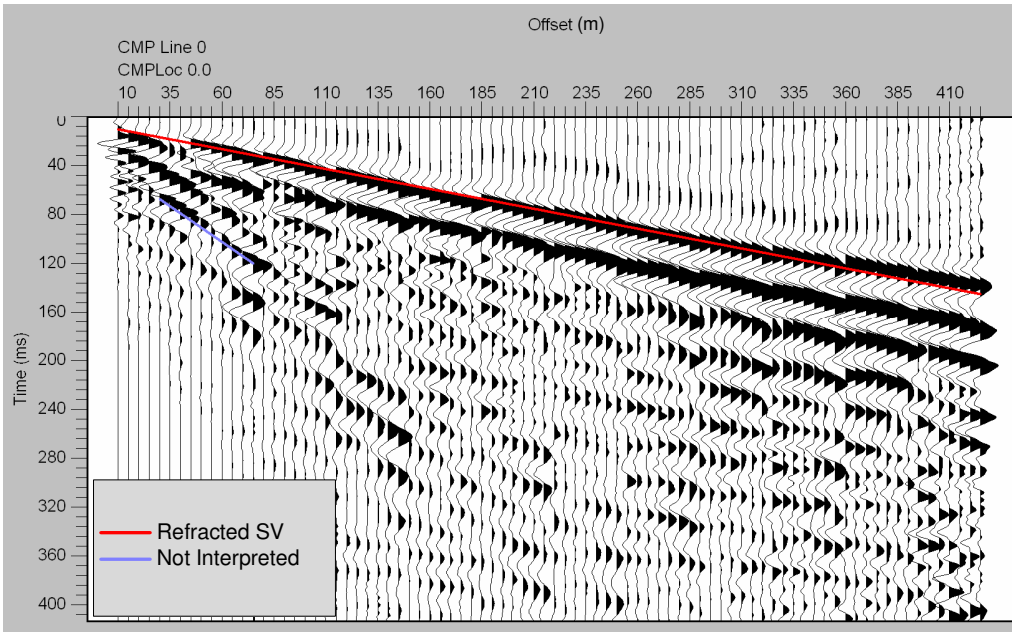

(a)

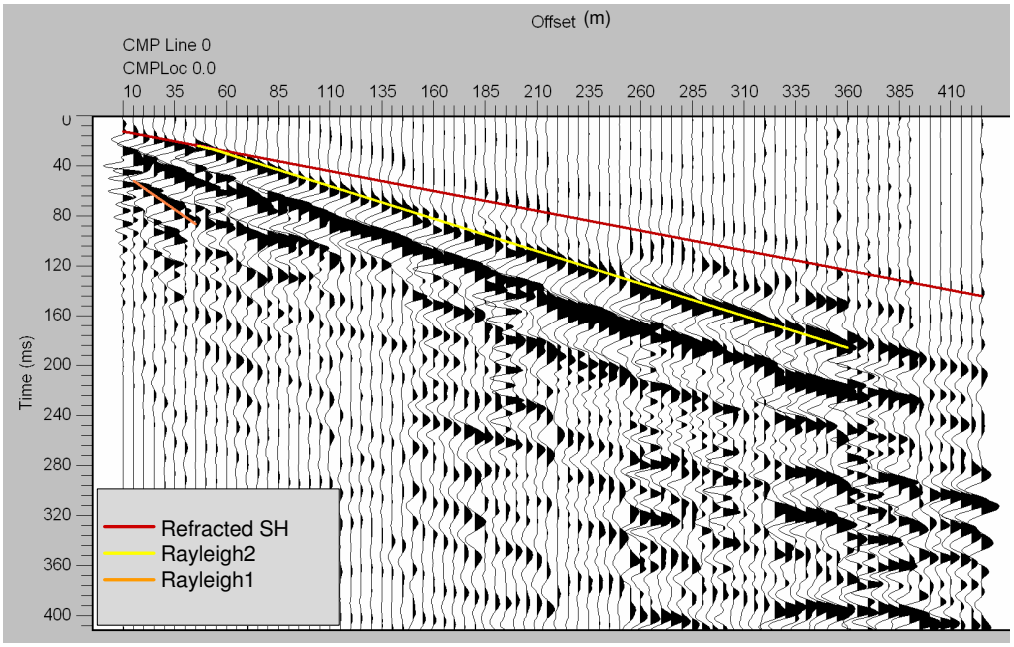

(b)

Figure 5.10 Seismic profile with interpretation for Line 2 at N88E, a) inline source, inline receiver and b) crossline source, crossline receiver components.

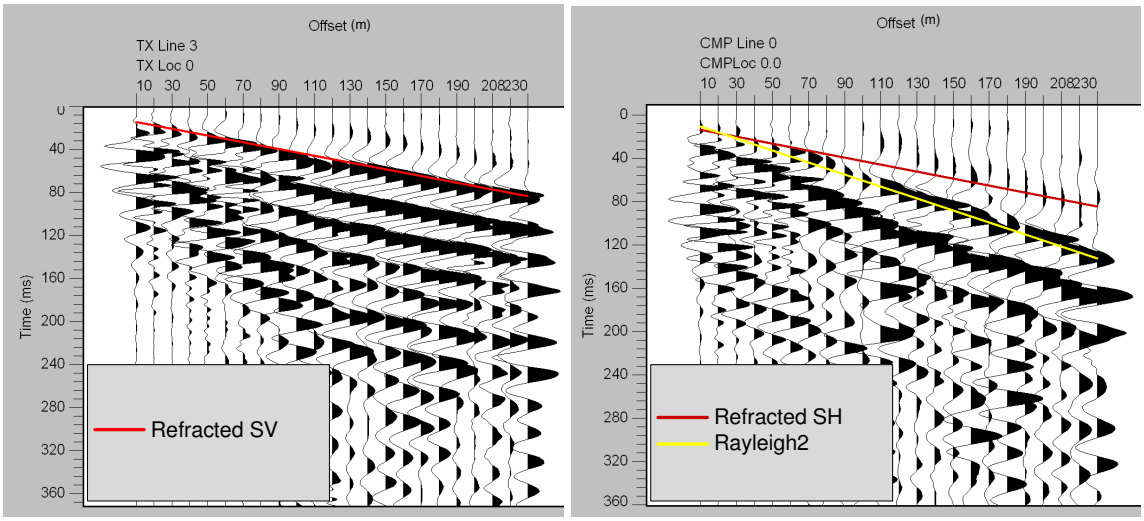

(a) (b)

Figure 5.11 Seismic profile with interpretation for Line 3 at N30E, a) inline source, inline receiver and b) crossline source, crossline receiver components.

Table 5.4 Wave velocities for the arrivals on the inline source, inline receiver (IN-IN) and crossline source, crossline receiver (X-X) components.

	Matched Source & Receiver Pairs		P2	SV2	SH2	Rayleigh 1	Rayleigh 2	Other
Line 1	**IN-IN**	Velocity (m/s)	5738 ± 77	3049 ± 37	n/a	n/a	n/a	640 ± 18
	X-X	Velocity (m/s)	n/a	n/a	3031 ± 34	n/a	n/a	245 ± 3
Line 2	**IN-IN**	Velocity (m/s)	n/a	3088 ± 24	n/a	882 ± 21	n/a	n/a
	X-X	Velocity (m/s)	n/a	n/a	3162 ± 25	873 ± 27	1928 ± 9	n/a
Line 3	**IN-IN**	Velocity (m/s)	n/a	3176 ± 24	n/a	n/a	n/a	n/a
	X-X	Velocity (m/s)	n/a	n/a	3017 ± 21	n/a	1823 ± 16	n/a

5.6 FRACTURE ORIENTATION

Fracture orientation is estimated by determining the angles of polarization of split shear waves. The angles of polarization are often found by using the Alford rotation. The

Alford rotation is discussed below with the resulting fracture orientation at Stoneledge Quarry.

5.6.1 Alford Rotation

To determine the polarization directions of the split shear wave properly, the axes of the recorded data must be aligned with the natural coordinate system of the anisotropic medium. This is done using a method of synchronous rotation such as that developed by Alford (1986) and used in the birefringence analysis during processing of the Vibroseis source seismic data.

Alford's (1986) method numerically rotates the source and receiver data simultaneously in a horizontal plane about the vertical axis using incremental changes in polarization angle. Both the S1 wave and the S2 wave are recorded at each trace unless in the rare case that the recording coordinate system is aligned with the natural anisotropic coordinate system (Mueller, 1992). Therefore, the angles of rotation showing only one shear wave are the angles that correspond to the medium's natural coordinate system.

Figure 5.12 displays the physical set up and results of an experiment by Cheadle et al. (1991). The results show polarized seismic traces at different angles of rotation through an anisotropic sample of phenolic. The phenolic used for this experiment is a laminate of sheets of woven canvas fabric adhered together with phenolic resin. The phenolic cube is rotated 360^{o} about the vertical axis. S1 and S2 are separated completely by approximately 90^{o} rotations. The azimuth of the first arriving shear wave, S1, on the seismic record corresponds to the azimuth of the cube parallel to the sheets of fabric.

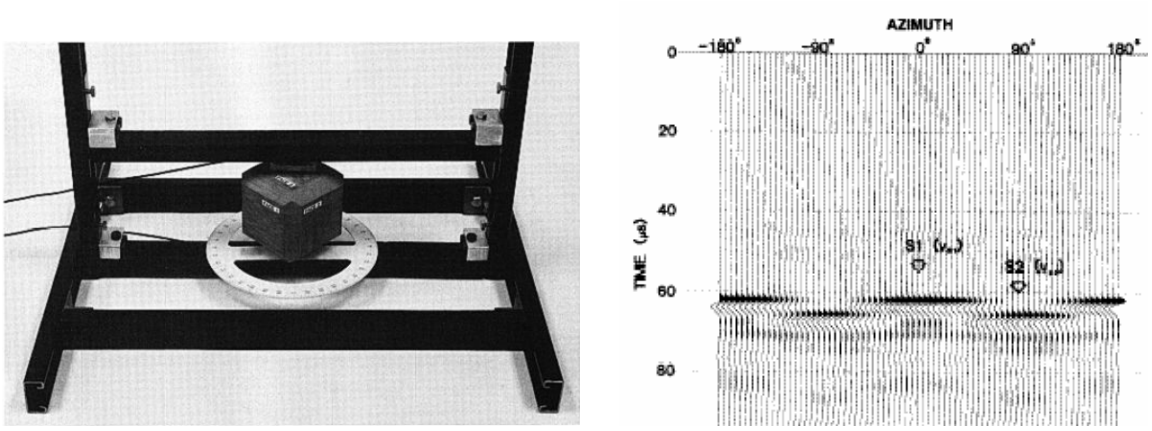

a) b)

Figure 5.12 a) Set up of shear wave splitting experiment. b) The seismic record of shear wave splitting experiment (Cheadle et al., 1991).

S1 is polarized in the same direction as the dominant orientation of anisotropy and can therefore be used to estimate its strike after rotation of the data (Li and Mueller, 1997). A dominant orientation of anisotropy can be expected in fractured areas because observed fractures are usually near vertical and have parallel alignment. Non-vertical fractures often become closed and sealed due to overburden pressures. The horizontal stress field tends to align vertical fractures provided stress is greater in one direction than its orthogonal component, which is typical in most cases of fracturing (Mueller, 1992).

5.6.2 Fracture Orientation Results

Fracture orientation is estimated by determining the polarization angles of the split shear waves, S1 and S2. The axes of the recorded data should be aligned with the natural coordinate system of the anisotropic medium to properly determine the polarization directions. This was done using the birefringence analysis in SPW, which is based on the Alford rotation. Figure 5.13 shows the results of numerically rotating the four shear wave components using this method. Figure 5.13 is Line 2 of the Vibroseis

data at an offset of 150 m (receiver location 29). This analysis uses the inline and crossline source components, 24 and 23 respectively, recorded on the inline and crossline receiver components, 14 and 13 respectively. Energy is maximized on components having matched source and receiver pairs and minimized on mixed component pairs. Significant energy still remains on the mixed pairs but it is greatly diminished compared to the amplitudes prior to rotation. The optimal angle of rotation producing the result in Figure 5.13 is 54°. S1 arrives on the matched inline source and receiver pair as indicated on the figure by the red circle. S2 arrives on the crossline source and receiver pair. Both S1 and S2 have negative polarity indicating that the rotation angle is in the negative direction. Therefore, Line 2 at an azimuth of 88° should be rotated -54° to be aligned parallel to the strike of the dominant fracture set. This rotation results in an azimuth of N34E, which is approximately the same as the orientation of the primary fracture set measured in the field.

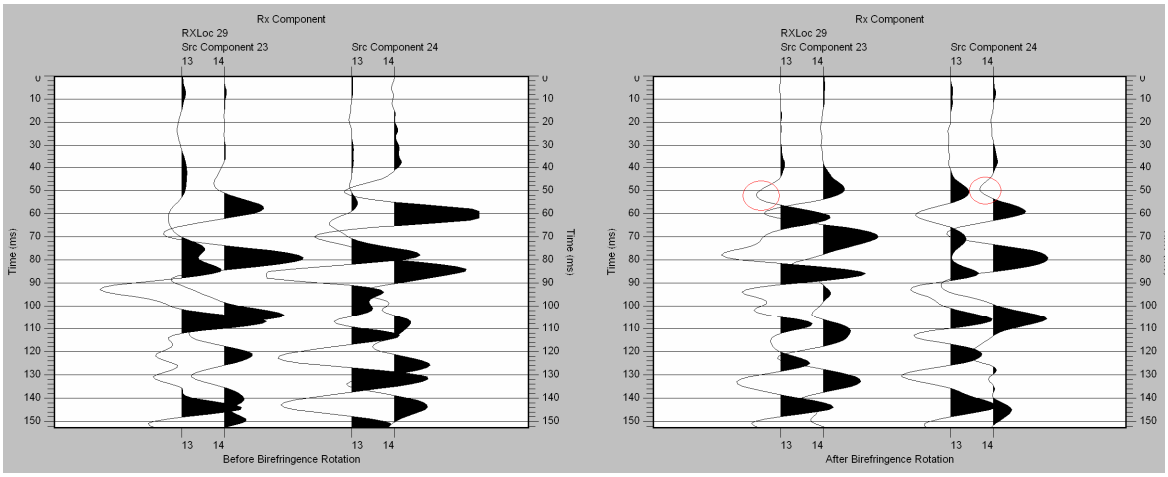

(a) (b)

Figure 5.13 Shear wave component traces a) before and b) after Alford rotation. X-axis: outer two traces are the matched source and receiver pairs, inner two traces are the unmatched pairs. Y-axis: time in ms.

Optimum rotation angles calculated using the Alford rotation on the Stoneledge Quarry Vibroseis data are listed in Table 5.5. The results show that fractures at Stoneledge Quarry are oriented at about N39E, which is comparable to the primary orientation measured in the field. The average azimuth of the inline components of the geophones is used to determine the orientation of the principal axes of the fracture anisotropy rather than the azimuth of the acquisition line. Geophone azimuth is more sensitive to shear wave polarizations than acquisition line azimuth.

Table 5.5 Results of birefringence analysis.

Fracture Orientation	Average Geophone Azimuth (degrees)	Optimum Rotation Angle (degrees)	Principal Axis Azimuth Parallel to Anisotropy (degrees)
Line 1	320	78	38
Line 2	93	-54	39
Line 3	34	5	39

5.7 FRACTURE DENSITY RESULTS

Fracture density may be estimated from observed anisotropy of a fractured medium. The time difference between the S1 arrival and the S2 arrival is a result of the average anisotropy of the raypath as described in Chapter 3, section 3.3. Equation 3.5 allows an estimate of fracture density from observed anisotropy velocities measured from the seismic data and a value for Poisson's ratio for unfractured conditions. This is one of the methods used to calculate fracture density from the sledgehammer source data in Chapter 4. Fracture density is also related to the incidence angle of the wave relative to the fracture normal. Therefore, the angle of incidence must be taken into account. At 90^{o} incidence to fracture normal, seismic velocities are closest to isotropic conditions as shown in Figure 3.2 through Figure 3.5 in Chapter 3. This angle of incidence also is appropriate to invoke traditional notions of SV and SH waves and related velocities. Using the fracture orientation found above at N39E, the average geophone azimuthal

angle to the fracture normal for Lines 1 through 3 are 11°, 36°, and 85°, respectively. These angles are similar to those used in fracture density analysis from the sledgehammer source data. Line 3 should be appropriate to use in calculation of fracture density because it is orientated near 90° with the fracture normal.

P and SV wave velocities are used to calculate Vp/Vs and Poisson's ratio. The SH velocity is used to calculate γ, which is included with Poisson's ratio in Equation 3.5 to get fracture density. The P wave velocity is obtained from the vertical source, vertical receiver component, as this corresponds to the conventional P wave velocity. Likewise, the SV and SH wave velocities are obtained from the matched components for inline and crossline orientations, respectively. Only the velocities of the saturated half-space are used to determine fracture density from Equation 3.5 because shear wave velocities in the upper, unsaturated layer were not identified in the seismograms. Table 5.6 shows the values used to obtain fracture density from the seismic data from Equation 3.5. These values are similar to those obtained from the sledgehammer source.

Table 5.6 Fracture density and values used to obtain it from the Vibroseis source seismic data.

Vibroseis Data	Saturated Half-space
Vp (m/s)	5729
Vsv (m/s)	3176
Vsh (m/s)	3017
Vp/Vs	1.80
Poisson's Ratio	0.278
γ	0.053
Fracture Density	0.047

Also, I calculated the percent change in velocity from theory between SV and SH for various fracture densities and azimuths. Then, I calculated the percent change in velocity from the matched component data for SV and SH arrivals for each line. The results of the calculations from theory and the data are presented in Table 5.7. The data

show changes in velocities very similar to those expected for 5% fracture density under saturated conditions.

Table 5.7 Velocity variation between SV & SH waves for unsaturated and saturated conditions from theory and results from this study.

Incidence angle with fracture normal		Unsaturated			Saturated		
		1%	5%	10%	1%	5%	10%
Theory	0°	0.00	0.00	0.00	0.00	0.00	0.00
Line 1	**11°**					-0.59	
Theory	20°	0.05	0.02	-0.32	-0.33	-1.59	-3.07
Line 2	**36°**					-2.34	
Theory	45°	0.36	1.22	1.49	-0.55	-2.54	-4.67
Theory	60°	0.68	2.93	4.97	0.00	0.00	0.00
Line 3	**85°**					5.27	
Theory	90°	1.11	5.43	10.59	1.11	5.43	10.59

Another approach to estimating fracture density is to plot velocity versus incidence angle relative to fracture normal for various fracture density curves such as in Figure 3.2 through Figure 3.5. Estimates of fracture density may be made from fitting the velocity values to the appropriate fracture density curve. The curves with velocities from the seismic data are shown in Figure 5.14 through Figure 5.17. The values used in these figures are listed in Table 5.2 and Table 5.4 and are from the matched component pairs. Other values of fracture density at 0%, 1%, 5%, and 10% are calculated from theory. The fracture densities of 4.7% from Table 5.6, 5% from Figure 5.14, 4% from Figure 5.15, and 5% from Figure 5.17 at Stoneledge Quarry are within the confidence interval calculated from field scan line measurements (0.2% to 5%).

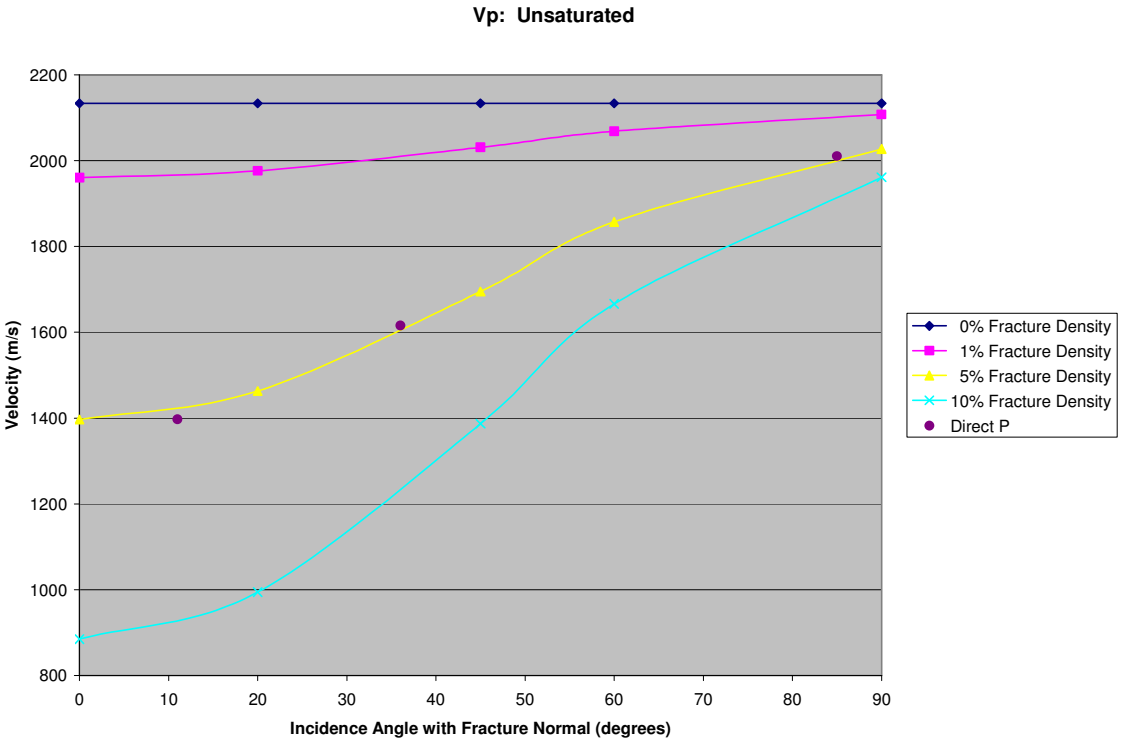

Figure 5.14 Velocities for the direct P wave at different azimuths. Fracture density in the unsaturated upper layer is about 5% based on this graph.

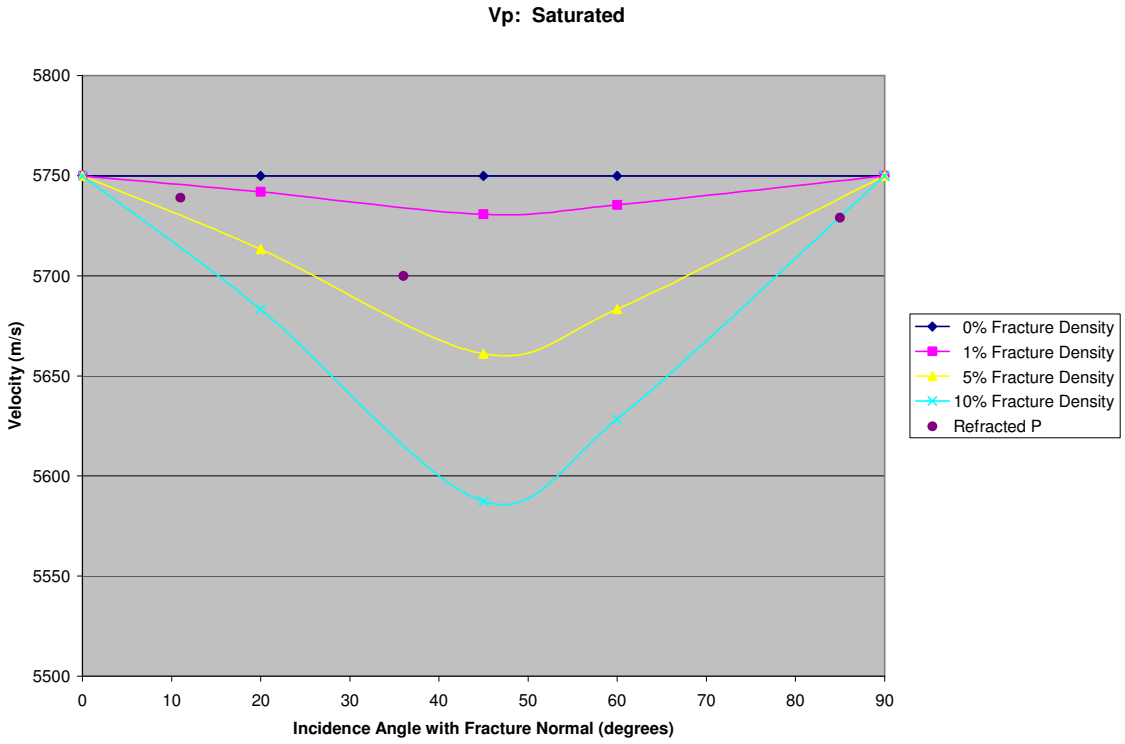

Figure 5.15 Velocities for the refracted P wave at different azimuths. Fracture density in the saturated half-space is about 4% based on this graph.

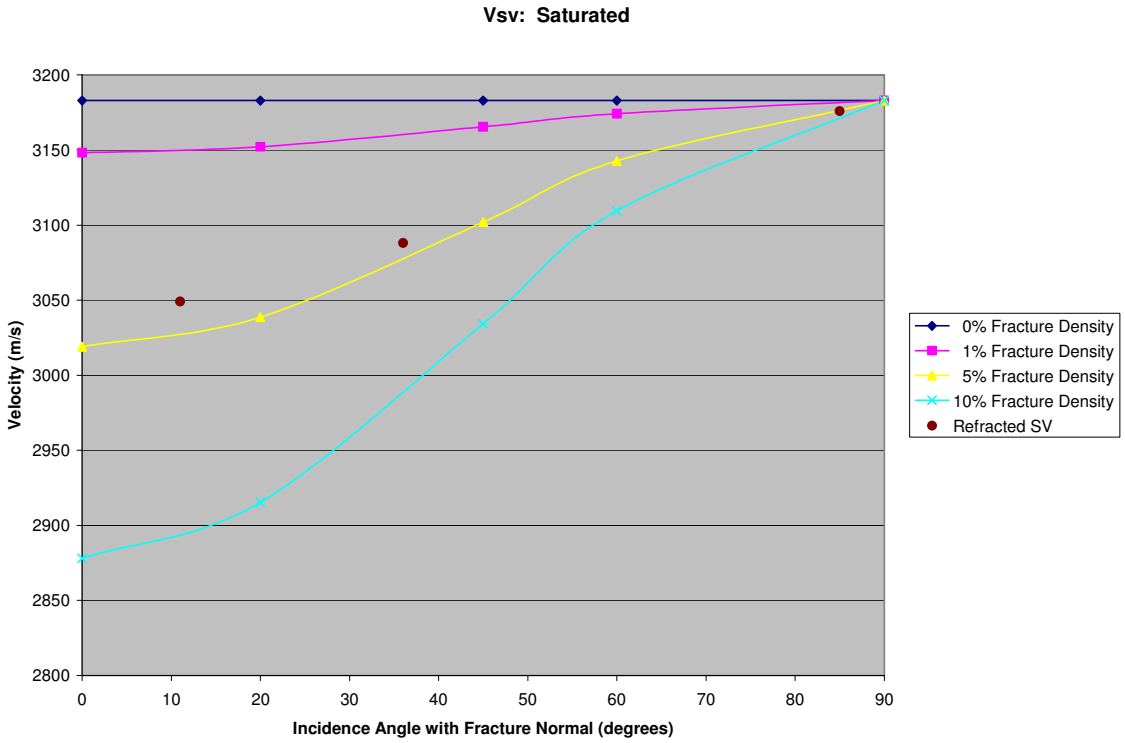

Figure 5.16 Velocities for the refracted SV wave at different azimuths. Fracture density in the saturated half-space is about 5% based on this graph.

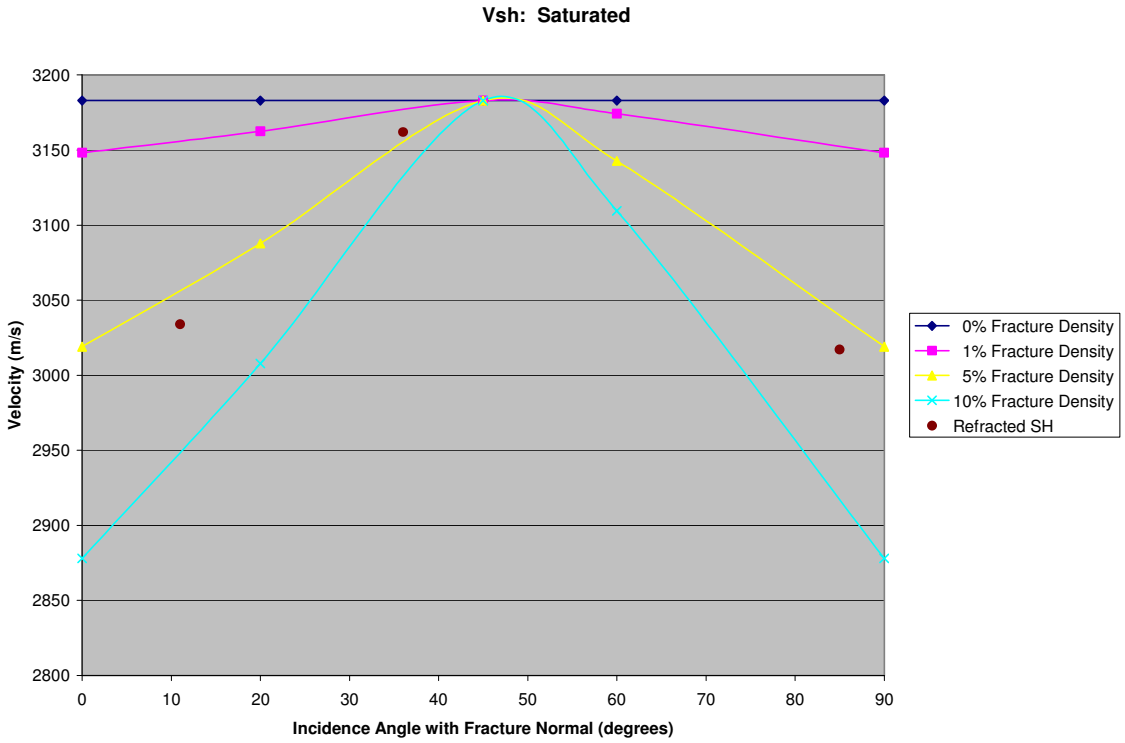

Figure 5.17 Velocities for the refracted SH wave at different azimuths. Fracture density in the saturated half-space is about 5% based on this graph.

Table 5.8 Values from Stoneledge Quarry seismic data plot in Figure 5.14 through Figure 5.17.

Seismic Acquisition Line	Incidence Angle with Fracture Normal	Direct P Velocity (m/s)	Refracted P Velocity (m/s)	Refracted SV Velocity (m/s)	Refracted SH Velocity (m/s)
Line 1	11°	1397 ± 15	5739 ± 122	3049 ±	3031 ±
Line 2	36°	1616 ± 11	5700 ± 27	3088 ±	3162 ±
Line 3	85°	2011 ± 28	5729 ± 167	3176 ±	3017 ±

Additionally, velocity anisotropy is evident in the Rayleigh wave arrivals. The Rayleigh waves exhibit strong evidence for anisotropy because their arrivals are clear and of large amplitude, leading to relatively low error. The fractional variation in Rayleigh wave velocity with azimuth is within the range of velocity variation in the body waves. The percent variation in velocity among the three acquisition lines for the waves detected

in the seismic data are shown in Table 5.9. Rayleigh wave speeds are known to be most sensitive to shear (SV) speeds in a homogeneous material, implying that these can be taken as proportional to SV velocities and the fractional change used as another measure of anisotropy. However, as shown in Table 5.9 and in Chapter 4, the percent change in velocity of Rayleigh waves is much higher than SV waves, implying that the Rayleigh wave may not fit this line of reasoning for anisotropic conditions.

Table 5.9 Percent change in velocities measure from the sledgehammer source seismic data at Stoneledge Quarry.

Velocity variation between:	Direct P (%)	Refracted P (%)	Refracted SV (%)	Rayleigh1 (%)	Rayleigh2 (%)
Lines 1 & 2	15.7	0.7	1.4	n/a	8.8
Lines 1 & 3	44.0	0.2	4.0	n/a	14.4
Lines 2 & 3	24.4	0.5	2.6	8.2	5.2

Finally, the increase in P velocity for the presumed unsaturated layer to the saturated half-space provides an additional measure of fracture density, given the only change in the medium is fracture saturation. For example, theory indicates that the increase in P wave velocity from unsaturated to saturated conditions at 5% fracture density for 0^{o} angle with fracture normal is about 15%. Lower fracture densities show smaller increased and higher densities show larger increases. However, taking the increase in P velocity in Line 1 from 1397 m/s for dry fractures to 5739 m/s for saturated fractures implies a fracture density of over 100%. This is obviously not possible. Other factors besides saturation are contributing to the low velocity of the upper layer or fracture density in the upper layer cannot be determined using this method. Similar results were determined in Chapter 4.

5.8 CONCLUSIONS

Fracture orientation from Alford rotation analysis is estimated at N39E, which generally agrees with field measurements, regional faulting at N35E, and the Mt. Bonnell

fault at N40E about 5 km from the site. Because Line 3 at N30E is oriented near the fracture strike, the velocities estimated from this line plus fracture density can be used to describe the conditions of the subsurface. Velocities from this direction may be interpreted using conventional notions for isotropic material and velocities at other azimuths can be estimated from the fracture density and line azimuth. Based on this reasoning, wave velocities at Stoneledge Quarry are about: 2011 m/s and 5729 m/s for P in the upper layer and half-space, respectively, 3171 m/s for SV in the half-space, and 960 m/s and 1835 m/s for Rayleigh in the upper layer and half-space, respectively. These values are consistent with those measured from the sledgehammer source data. Fracture density is estimated between 4% and 5% based on velocity anisotropy. This range is similar to the 3% and 5% range determined from the sledgehammer source data. Field measurements of fracture density average about 1% with a confidence interval between 0.2% and 5%.

Thickness of the upper layer corresponds to the depth to the water table, which is between 26 and 30 m. Therefore, fractures above this depth are assumed filled with air and water-filled below. This is deeper than the rough estimate made from observations in the field (17.2 m) but reasonable considering the wavelengths of about 120 to 380 m. Additionally, part of upper layer may be saturated. The water table is somewhat shallower than indicated in seismic data (Bradford, 2002) as discussed in Chapter 3.

Other information gained from the seismic data includes lithology from Vp/Vs and Poisson's ratio. Empirical data show Vp/Vs ranges from 1.84 to 1.99 for limestone and from 1.78 to 1.84 for dolomite (Domenico, 1984). Additionally, empirical data show Poisson's ratios range from 0.29 to 0.33 for limestone and from 0.27 to 0.29 for dolomite (Domenico, 1983). Vp/Vs is 1.80 and Poisson's ratio is 0.278 from this data set. The

seismic data indicate that the medium is dolomite, which agrees with Stoneledge Quarry being in the dolomitic member of the Edwards Group.

Finally, the additional components provided by the 9C Vibroseis data provide other data in addition to the conventional vertical component. These components provided direct measurement of the SH wave velocity in addition to the P, SV, and Rayleigh wave velocities measured from the vertical source, vertical receiver component. SH waves were not identified on any of the vertical source components. The additional components also confirm velocities of waves identified on vertical source, vertical receiver records. Arrivals are less ambiguous on matched component pairs and appear to have a higher signal to noise ratio. This provides additional confirmation and confidence in velocity estimates. Though some arrivals may be ambiguous, confirmation of their velocities on other components makes them more credible. Therefore, in areas where wave arrivals are ambiguous due to interference from out of plane reflections and other events, additional receiver components serve to decrease the ambiguity. In addition, the Vibroseis data show a higher signal to noise ratio than the sledgehammer data, leading to better estimates. Finally, the Vibroseis data provided direct measurement of the SH wave velocity, not generated directly in the sledgehammer survey, providing a more accurate estimate of fracture density.

Chapter 6: Tracer Imaging with GPR Experiment

6.1 INTRODUCTION

Understanding how liquids flow in fractures is important for understanding groundwater flow and for developing remediation efforts for subsurface contamination. Variations within a fracture often cause liquids to favor a particular path or channel, a situation referred to as channelized flow. Traditional hydrogeological methods using observations at wells cannot easily determine flow channel geometry. As point measurements, well observations do not provide the spatial resolution concerning fracture properties or fluid flow that is possible with a noninvasive geophysical imaging method like ground penetrating radar (GPR).

Tracer tests are performed in hydrogeological studies to determine velocity and direction of fluid flow in the subsurface. The tracer may be natural or induced and must be easy to distinguish from groundwater. Common tracers are solutes such as dyes and sodium chloride, suspended material, or heat (Sharp, 2003). As part of a hydrogeological study by Garner (2007), a saline tracer was used to determine the contribution of channeling to tracer breakthrough curves, which plot tracer concentration versus time. Variations in curve peak and shape may indicate channeling effects. An understanding of flow path location, length, and pooling are necessary for accurate models of channelized flow and transport and to interpret tracer breakthrough curves.

Two types of channeling are analyzed in this study, flow channeling in the fracture plane and tracer channeling within the flow. The hypotheses are that spatial and temporal variations in concentration may be controlled by channel geometry and that understanding channel geometry will lead to more precise descriptions of advection and hydrodynamic dispersion.

Previous research has used GPR in fluid detection studies. Daniels et al. (1995) used changes in amplitude to map hydrocarbons in the vadose zone. Tsoflias and Sharp (1998) and Tsoflias et al. (2001) used changes in amplitude to determine aquifer saturation conditions. Talley et al. (2005) used changes in amplitude to map fluid tracers flowing through a saturated fracture in an aquifer. Day-Lewis et al. (2003) and Lane et al. (1999) used attenuation-difference tomography to locate fluid tracers flowing through a saturated fracture in an aquifer. Lane et al. (2000) used changes in amplitude to identify fractures and determine fracture filling fluid. All of these studies with the exception of Daniels et al. (1995) used 100 MHz and/or 200 MHz centerline radar frequencies. The highest centerline frequency used by Daniels et al. (1995) was 500 MHz. My study differs from these previous studies in several ways: 1) the saline tracer moves through a variably saturated fracture in the vadose zone; 2) the channel network rather than tracer plume is mapped using surface GPR; 3) the experiment approximates steady-state conditions rather than flow under dynamic conditions; and 4) much higher frequencies (1500 MHz) are used to obtain greater resolution at shallow depths. The exposed outcrop and shallow depth of the fracture for this study allow visual assessment of fractures intersecting the imaged fracture.

6.2 GROUND PENETRATING RADAR OVERVIEW

GPR uses electromagnetic (EM) waves, typically in the frequency range of 10 MHz to 1.5 GHz to image the shallow subsurface. EM waves are transmitted by one antenna, propagate through the subsurface until they are reflected at boundaries, and are received at a second antenna. Theory of EM waves is given in detail for geophysical applications by Ward and Hohmann (1987). Davis and Annan (1989) outline principles and methodologies for conducting GPR surveys.

The relevant physical properties that control behavior of the EM waves in the near-surface are found in Maxwell's equations. These include magnetic permeability, electrical conductivity, and dielectric permittivity (Keller, 1987). Magnetic permeability relates the strength of the magnetic field to magnetic induction and describes the capacity of a material to become magnetized by an applied magnetic field. Most rocks lack significant quantities of magnetic minerals and have a relative permeability of 1, equal to magnetic permeability in a vacuum. Therefore, magnetic permeability often has a negligible effect on GPR data. Electrical conductivity relates the strength of the electric field to current density. Geologic materials with low electrical conductivity (called 'low-loss') allow passage of EM waves and with increasing electrical conductivity there is greater attenuation of the EM waves. Relative dielectric permittivity, also called the dielectric constant, is the capacity of electrically sensitive particles (electrons, nuclei, and polar molecules) to become polarized, aligned with the direction of the field, when an electric field is applied (Lane et al., 2000). For low electrical conductivity (< 10 mS/m) and nonmagnetic media, relative dielectric permittivity can be calculated empirically from field data or measured in the laboratory (Martinez and Byrnes, 2001).

Water is both a polar molecule and a major contributor to subsurface electrical conductivity. Therefore, the presence of water often is the dominant influence on EM wave velocity and attenuation in the subsurface (Annan, 2005). The presence of water in a void generally produces large reflection amplitudes. The polarity is also indicative of water, because a negative reflection coefficient is produced at a boundary between a low dielectric permittivity region (e.g., air or granite) to a high dielectric permittivity region (e.g., water-filled fracture or void).

EM waves reflect at boundaries in the subsurface where electrical properties change. In nonmagnetic, low-loss media, the relative dielectric permittivity controls the phase velocity of the EM waves by

$$v \approx \frac{c}{\sqrt{\mu_r * \varepsilon_r}} \qquad 6.1$$

where c is EM wave velocity in a vacuum (3 x 10^8 m/s), μ_r is relative magnetic permeability (1), and ε_r is relative dielectric permittivity of the medium (Davis and Annan, 1989). Like reflection seismology, the Fresnel reflection and transmission coefficients quantify changes in amplitude of EM waves across a boundary. For normally incident waves, reflection coefficients for electric and magnetic fields are the same. Fractures investigated in this study can be modeled as a thin layer with thickness much less than incident wavelength. Separate reflections from the top and bottom of the layer cannot be resolved but together may produce constructive or destructive interference affecting reflected signal amplitude and phase. A thin layer reflection equation describes this interference that includes all reverberations within the layer and is frequency (or wavelength) dependent. The reflection coefficient equation for a thin layer for a plane wave arriving at incidence angle, θ, is given by

$$R_{thin-layer} = R_{12} + \frac{T_{12}T_{21}R_{21}\exp^{i2kd\cos\theta}}{1 - R_{21}^2\exp^{i2kd\cos\theta}} \qquad 6.2$$

where R and T are the Fresnel reflection and transmission coefficients, respectively (Annan, 2005; Hollender and Tillard, 1998; and Talley et al., 2005). Subscript 1 denotes the medium surrounding the layer and subscript 2 denotes the material within the layer of thickness d. The incidence angle, θ, is zero for normally incident waves. The exponents

contain the time delay or phase shift of plane waves within the layer and depend upon wavenumber, k, proportional to angular frequency ($\omega=2\pi f$).

$$k = \frac{2\pi}{\lambda} = \frac{\omega}{v} \tag{6.3}$$

where λ is wavelength and v is phase velocity. R and T can be calculated using Equation 6.4, which gives values for reflection and transmission coefficients for normally incident waves assuming the following conditions are met: 1) Snell's law is fulfilled (horizontal components of propagation vectors of EM waves are identical in the material above and below the boundary), and 2) electric and magnetic fields in the plane of the boundary as well as the electric current and magnetic flux density are equal above and below the boundary.

$$R = \frac{Z_1 - Z_2}{Z_1 + Z_2} \text{ and } T = 1 + R \tag{6.4}$$

Z is electromagnetic impedance and is given by

$$Z = \sqrt{\frac{\mu}{\varepsilon}}\left(1 - i\frac{\sigma}{2\omega\varepsilon}\right) \tag{6.5}$$

where σ is electrical conductivity. Large contrasts between relative permittivity of the medium above and below the reflecting boundary will result in large reflection coefficients (near $\pm$ 1) and large wave amplitudes.

6.3 NUMERICAL MODELING EXPERIMENT

The response of GPR waves reflected from a horizontal fracture in granite can be modeled using the equations above. A diagram of the model is shown in Figure 6.1. The

model uses typical values for parameters to obtain Equation 6.5. The thin layer represents the fracture and layer thickness, d, is fracture aperture. The model assumes normal incident waves and all materials are nonmetallic. Electrical losses were assumed insignificant and were ignored. Signal attenuation at the 1500 MHz center frequency used in this experiment was assumed negligible and was also ignored. The findings presented estimate the 1-dimensional response of GPR waves to different materials filling the fracture. Four different scenarios are modeled for the material filling the fracture: 1) air, 2) fresh water, 3) low salinity tracer, and 4) higher salinity tracer.

Figure 6.1 Cross-section of the model used to compute a thin layer GPR reflection. The granite layers are half-spaces above and below the fracture. Fracture response is modeled for various fluids including air, fresh water, low salinity water, and high salinity water.

Figure 6.2 shows how amplitude fluctuates as the ratio of aperture to wavelength varies and how the filling fluid affects the reflection response. Table 6.1 lists the parameters used to model the signal response. These parameters are within the typical

range given by Davis and Annan (1989) and Reynolds (1997). As aperture increases from 0.01 to 50 mm, reflection amplitude fluctuations become more frequent, with greatest variability as aperture approaches wavelength. Amplitude fluctuates as interference changes from constructive to destructive. With increasing aperture to wavelength ratio, wave attenuation would eventually reduce the amplitude of the reflections. Figure 6.3 shows amplitude fluctuations for the range of apertures expected to be encountered in this study.

Table 6.1 Parameters used in numerical model analysis.

	Dielectric Permittivity ε	Electrical Conductivity σ (mS/m)	EM Wave Velocity v (m/ns)	Magnetic Permeability μ
Granite	6	0.1	0.120	1
Air	1	0.0	0.300	1
Fresh water	80	0.5	0.033	1
Low salinity water	80	10	0.030	1
High salinity water	80	100	0.028	1

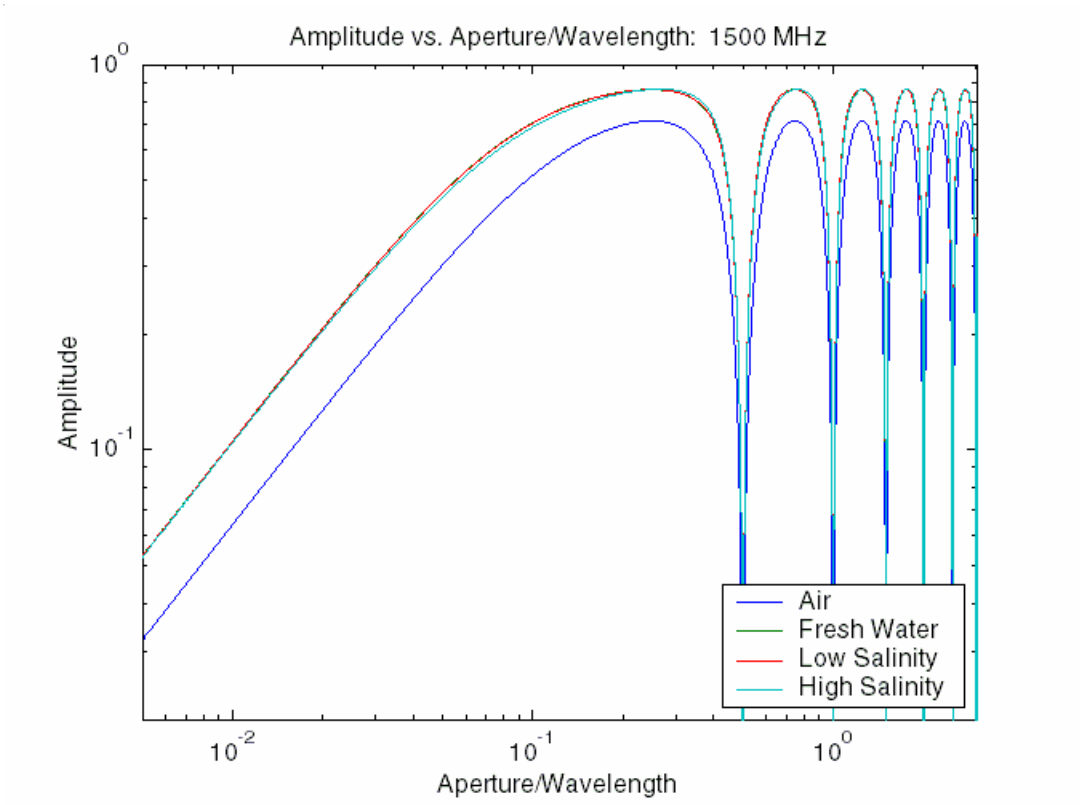

Figure 6.2 Amplitude of the reflection from a thin layer versus aperture to wavelength ratio. Fracture-filling fluids include air, fresh water, low salinity water, and higher salinity water.

Figure 6.3a) shows amplitude versus aperture for apertures in the 1 to 5 mm range and wavelengths expected in this study. This is similar to Figure 6.2, which show amplitude versus the ratio of aperture to wavelength. From Figure 6.3a), it is clear that amplitude alone is not diagnostic of fluid filling the fracture at some apertures. Previous studies used variations in amplitude to determine filling fluids (Daniels et al., 1995; Tsoflias and Sharp, 1998; Tsoflias et al., 2001; and Talley et al., 2005). However, these studies used lower frequencies (larger wavelengths) for which amplitudes increase with increasing fluid conductivity, as in Figure 6.3b). In this study, amplitudes alone may be diagnostic of fracture-filling fluid only for the smallest apertures from greater than zero to about 5 mm.

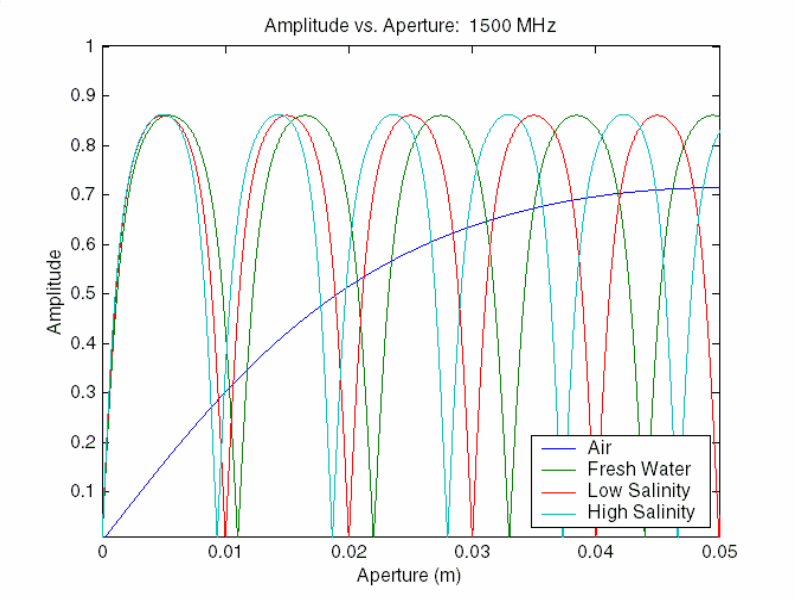

(a)

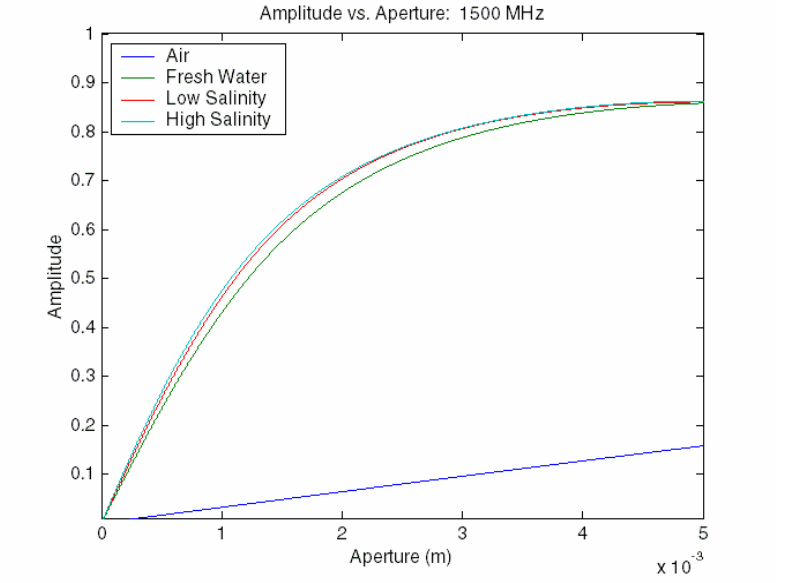

(b)

Figure 6.3 Amplitude versus aperture for air, fresh water, low salinity water, and higher salinity water as fracture filling fluids. a) amplitude variations over typical fracture apertures (~0 to 50 mm) and b) amplitudes diagnostic of filling fluid are only for the smallest fractures (~0 to 5 mm).

Variations of both reflection phase and amplitude can also be determined from Equation 6.2 for the four fluids. A Ricker wavelet, commonly used in GPR acquisition equipment, is used to model the response over a range of typical fracture apertures. A Ricker wavelet is a zero-phase or symmetric pulse with positive peak amplitude (Sheriff, 2002). The center frequency used is 1500 MHz and results of reflection variations due to the four fluids are shown in Figure 6.4.

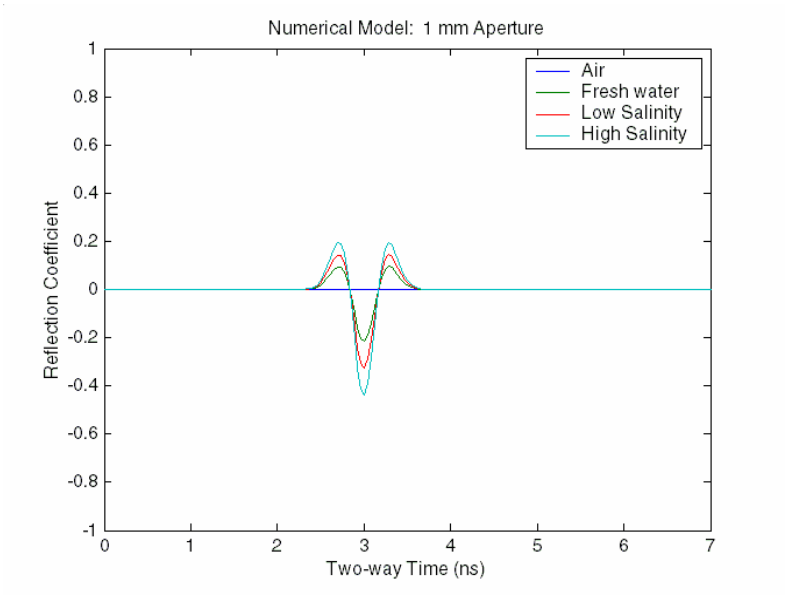

(a)

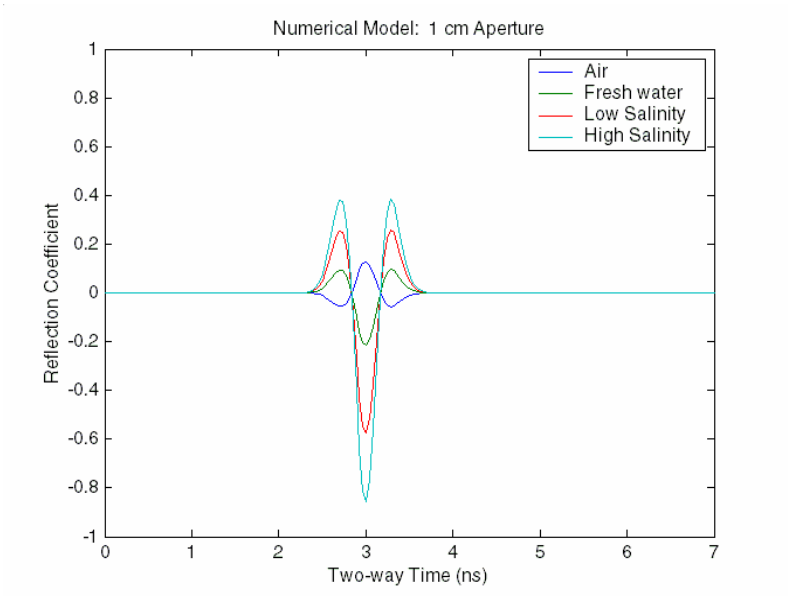

(b)

Figure 6.4 Reflected waveform for the four different fracture-filling fluids: air, fresh water, low salinity water, and higher salinity water for two fracture apertures: a) 1 mm, b) 10 mm.

6.4 FIELD EXPERIMENT

6.4.1 Site Description

The field experiment was conducted near Buchanan Dam, Texas about 90 km northwest of Austin (Figure 6.5). The site contains a granite outcrop with a subhorizontal shallow exfoliation fracture, ranging from a few centimeters to a few tens of centimeters below the surface. With such small depths, attenuation of high frequency radar waves is not significant and depth of penetration exceeds fracture depth. The shallow depth also provides direct access to the fracture via bore holes and additional intersecting fractures may be assessed visually. Intersecting fractures may result in loss of fluid and affect the experiment, but none were visible. The fracture is open, at least in part, allowing fluids to pass through. The bottom of slab of granite above the fracture has broken off and been removed by weathering. This allows fluid to be collected downslope for the tracer tests. Figure 6.6 is a picture of the site. The end of the top slab is visible, revealing the fracture opening downslope.

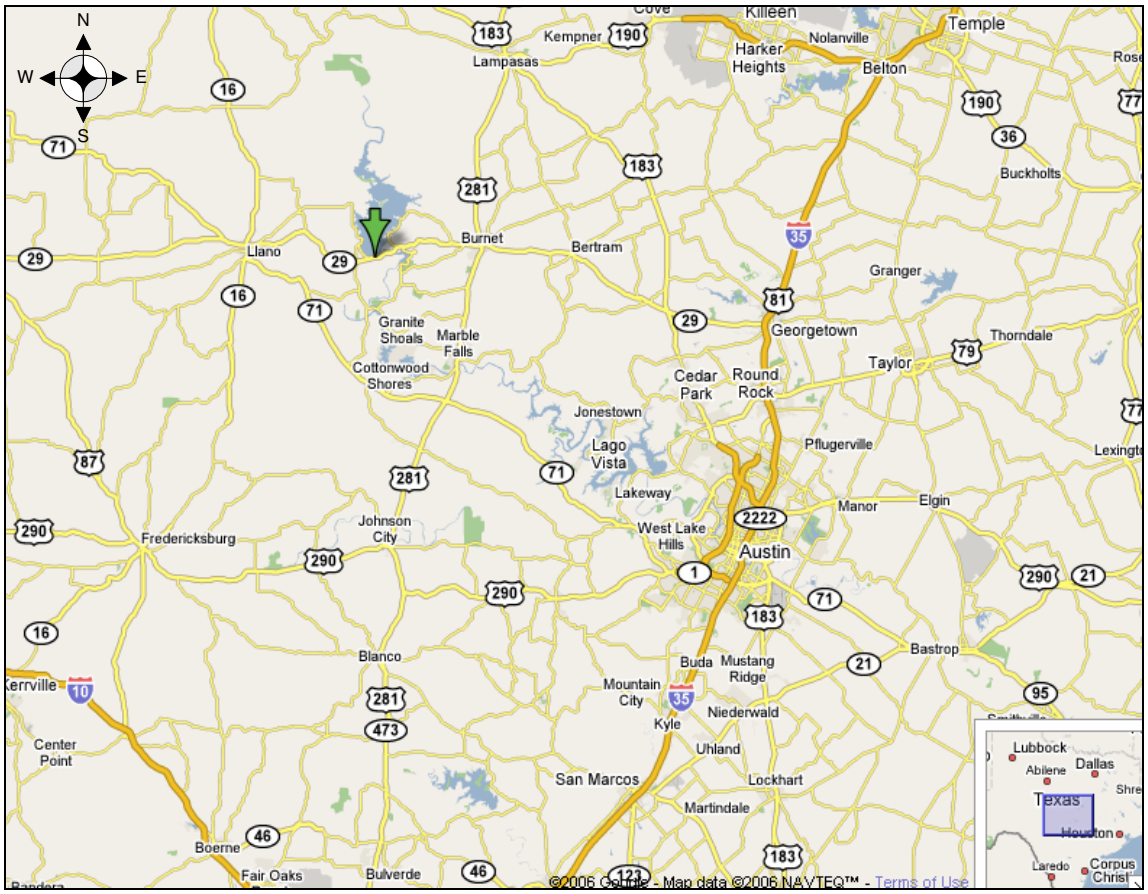

Figure 6.5 Map showing the site location. Buchanan Dam, Texas, is about 90 km northwest of Austin, marked with the green arrow (Google, 2006).

Figure 6.6 Photograph of the field site. The end of the top slab is visible, revealing the fracture opening downslope.

6.4.2 Field Experiment Design

Four boreholes were drilled vertically through the top layer of granite to intersect the subhorizontal fracture, along the upper edge area and spaced roughly one meter apart starting about one meter from the edge of the survey area. Figure 6.7 shows borehole locations and GPR survey locations. Boreholes were used to inject water and saline tracers into the fracture. Water from a nearby reservoir in excavated granite was pumped into a 20 kiloliter fiberglass container. During injection, a constant hydraulic head was maintained by pumping water to maintain overflow from the container. Steady-state flow conditions within the fracture were maintained by pumping water from the bottom of the

container into the fracture at a constant rate. A loop of tubing was used to equalize flow into each borehole. Valves and flow meters were placed on tubes leading to each borehole to independently regulate flow into each hole. Figure 6.8 shows the setup of injection tubes into the boreholes.

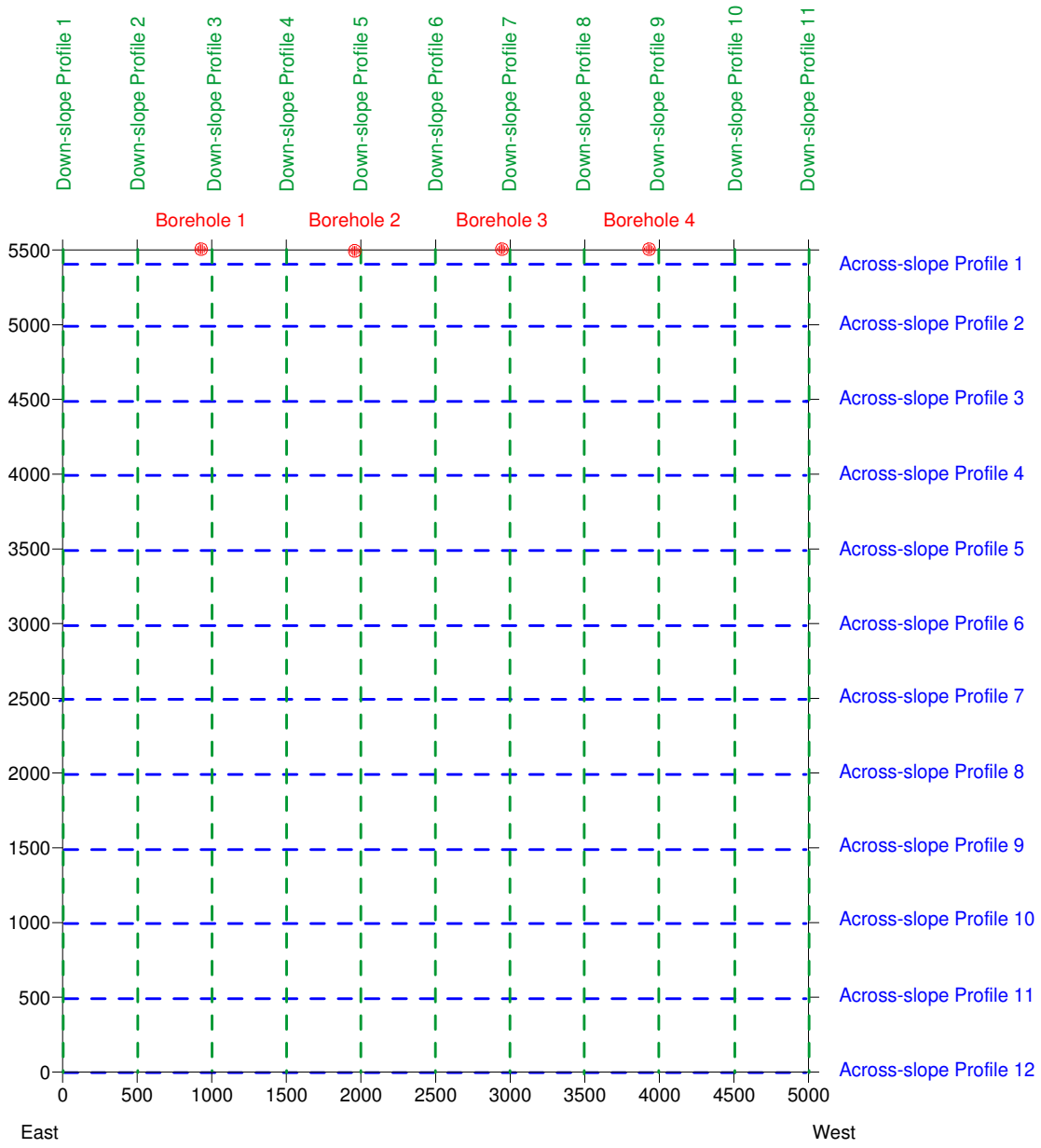

Figure 6.7 A schematic of borehole locations and the GPR survey area used in this experiment.

Water was injected into all four boreholes in an attempt to saturate the fracture. However, this failed because flow could not be increased sufficiently. Flow from Borehole 1 left the east edge of the fracture, out of the survey area. There was no flow from Borehole 2 indicating that it was not hydraulically connected to the fracture. Therefore, only Boreholes 3 and 4 were used to inject fluids during the experiments.

The low concentration saline tracer consisted of 230 mg of salt dissolved in 200 liters of water (1.15 mg/L). The high concentration tracer consisted of additional salt dissolved in 200 liters of water. Injections and surveys were performed in the order of increasing concentration so higher salinity injections would not contaminate lower salinity surveys. Tracers were gravity fed from a 200 liter container into Borehole 4. Pulse injections of tracer were conducted for tracer tests. Steady-state injections were conducted during GPR imaging to allow enough time for GPR data acquisition before tracers ran out. The time for each GPR survey was approximately 30 minutes.

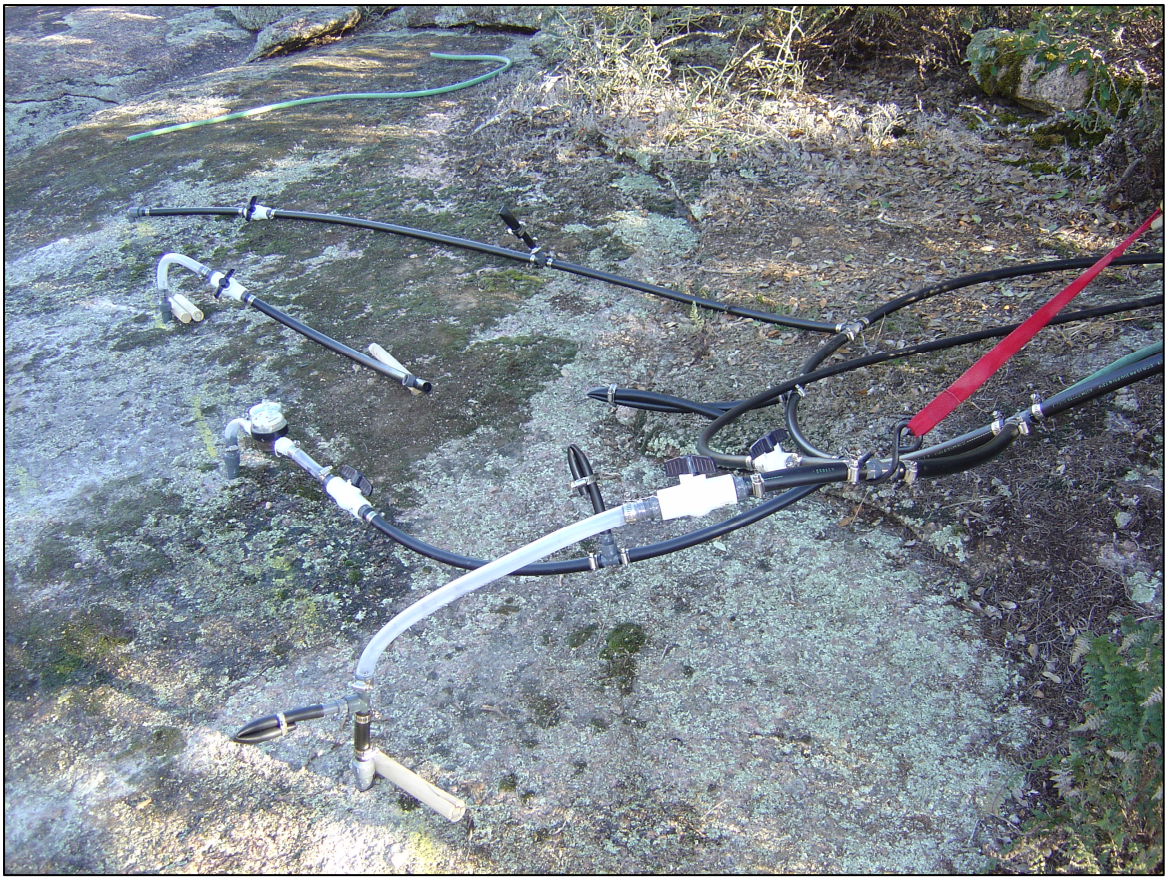

Figure 6.8 Boreholes and fluid injection tubes.

6.4.3 Survey Parameters

There is a tradeoff between resolution and depth of penetration in GPR surveys. High frequency waves improve resolution while low frequency waves provide greater penetration depth. Shallow depths in this case allow the use of the highest frequency available with the radar system. A Geophysical Survey Systems, Inc. (GSSI) TerraSIRch SIR System-3000 was used with 1500 MHz frequency, common-source-receiver-offset, ground-coupled, bistatic antennas. The system permits continuous data collection for fast acquisition. GSSI's 1500 MHz antennas have a parallel (broadside) configuration that was moved across a survey line to produce each radar profile. The method is similar to

common-offset profiling used in seismic reflection surveys. Multiple parallel profiles were collected to provide three-dimensional images.

The survey area was 5.0 m in the across-slope direction (approximately East-West) and 5.5 m in the down-slope direction (approximately North-South). Data were collected in constant sampling mode at 1000 traces per meter using a survey wheel. All profiles were collected at 0.5 m intervals except Profile 1 in the across-slope direction, which was positioned about 75 mm less than the 0.5 m interval to avoid the injection tubes. Profile direction was perpendicular to the dominant direction of expected flow (down-slope) during fluid injection. Profiles were collected during injection for: 1) water only, 2) water and low salinity tracer, and 3) water and high salinity tracer. Antennas were oriented perpendicular to the survey line to enhance diffractions from fluid flowing parallel to the antennas. Water was injected into Boreholes 3 and 4, but tracers were introduced into Borehole 4 only. However, some tracer may have entered Borehole 3 due to the tubing configuration. Figure 6.7 illustrates GPR survey profiles and borehole locations. Figure 6.8 shows injection tubes and relationship to the boreholes.

Two surveys were collected prior to injection of fluids to find signal response due to air filling and to determine variability of radar response for the site. The fracture may not have been completely dry due to rainfall the night before the survey. However, the surface was dry and no water was flowing from the fracture. The two initial surveys give site specific EM properties of the medium and reveal the presence of reflectors that might be erroneously interpreted during tracer tests. Differences between the two background surveys show variability expected at the same location due to slight variations in survey geometry, such as antenna location and orientation. The two surveys included profiles collected in the across-slope and down-slope direction, but only the across-slope profiles

were used to compare with the surveys collected during fluid injection. The data from the two were averaged to compare with the fluid injection surveys.

After the dry fracture GPR surveys, water was injected, and another survey was conducted. This was followed by the low concentration tracer injection and GPR survey, and finally the high concentration tracer injection and GPR survey. Survey parameters were based on results of equations given in Sensors & Software (1992) and system parameters of the GSSI equipment for optimal response at the site. Survey parameters are given in Table 6.2. Normally incident wave are assumed since the fracture is relatively shallow and the surface is relatively flat.

Table 6.2 Survey parameters used in GPR experiment.

Horizontal spatial sampling (mm): between profile lines	500
Horizontal spatial sampling (mm): along profile lines	1
Vertical sample rate (ns)	0.0391
Temporal sampling (samples/ns)	25.6
Trace length (ns)	20
Trace length (samples)	512
Antenna center frequency (MHz)	1500

6.4.4 Data Processing

Seismic Processing Workshop (SPW) software (Parallel Geoscience Corp.) was used to process GPR survey data. Each across-slope profile contains about 5000 traces with 1000 traces/meter and line lengths near 5.0 m. Profile lengths were slightly variable due to a rough granite surface and a relatively small survey measuring wheel. The data were resampled to make each profile contain an equal number of traces. Resampling allows more accurate comparison between profiles and each trace number corresponds to the same position on every profile. To make total line length exactly 5000 mm, traces were binned in 2 mm bins and averaged to produce one trace in each bin. This provides

2500 traces for each across-slope profile. The same process was applied to down-slope profiles to produce lines of 2750 traces spaced every 2 mm.

Figure 6.9 shows selected profiles of the raw data. Each profile in Figure 6.9 was collected during injection of water and high salinity tracer. Reflections from the fracture are clearly visible in all profiles. On across-slope Profile 1, there is an additional reflector around position 2521 mm and 15 ns (nanoseconds), which may be an additional fracture at this location. The additional reflector on across-slope Profile 12 is a multiple reflection of the fracture surface. Figure 6.9 shows that the fracture dips towards the East near the top of the survey area (near across-slope Profile 1) and undulates towards the bottom (near across-slope Profile 12) as the depth to the fracture decreases.

Figure 6.10a) shows a 3D representation of relative ground surface elevation collected using a Total Station. The elevation range is about 0.3 m from the upper area to the lower, as shown by the color bar. Below this, partially visible, is the fracture surface determined from first break picks in SPW. Figure 6.10b) shows the entire fracture surface. The image shows that the fracture surface is relatively flat in the down-slope direction while surface elevation slopes more steeply. The vertical scale is exaggerated relative to horizontal. The image of the fracture surface from first break picks is neither the top nor bottom of the fracture, because neither can be resolved, and the image might be referred to as “pseudo-surface”.

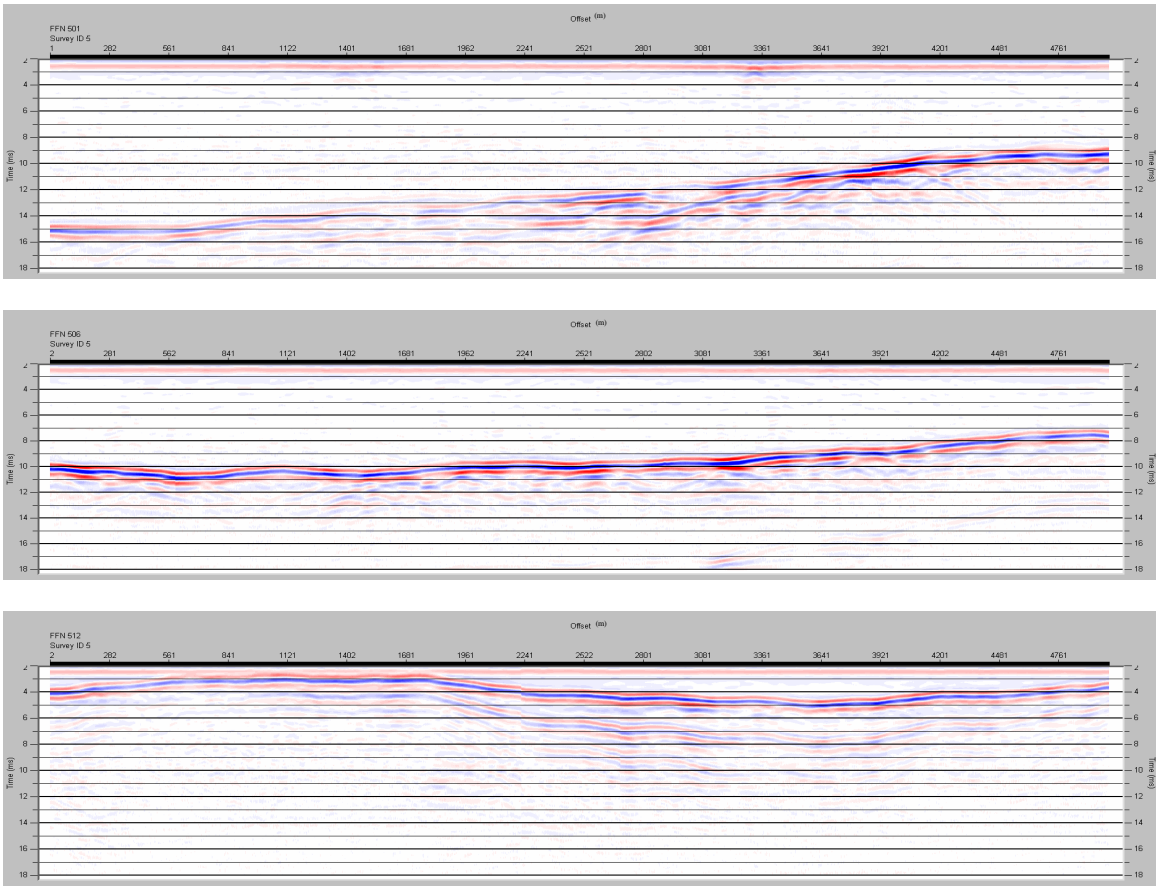

Figure 6.9 GPR across-slope Profiles 1, 6, and 12 from top to bottom, respectively. Profiles were collected during injection of water and high salinity tracer. Reflections from the fracture are clearly visible in all profiles.

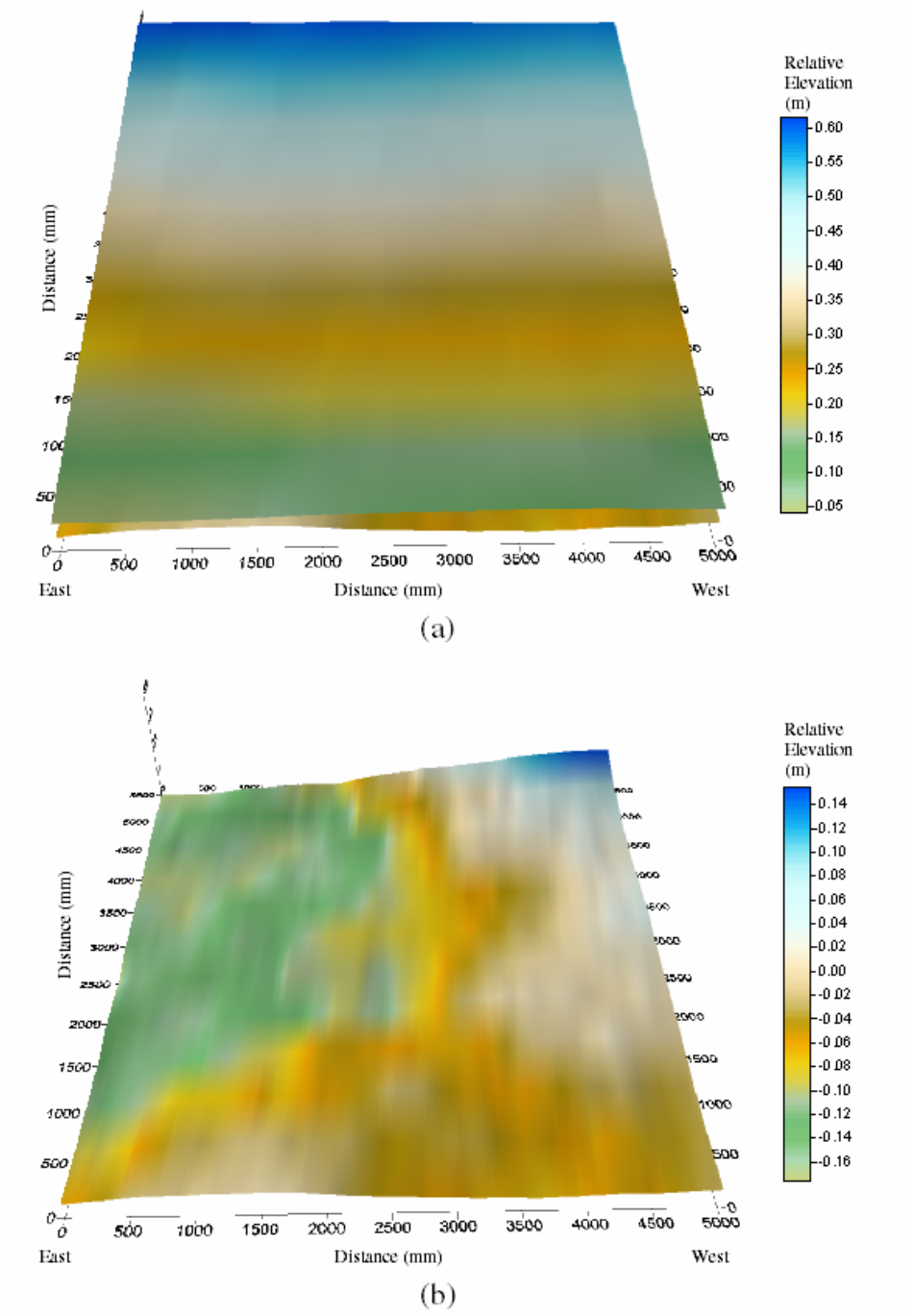

Figure 6.10 3D representations of a) the ground surface overlying the fracture pseudo-surface and b) the fracture pseudo-surface without the ground surface. The x and y scales are in millimeters and the z scale shown in the color bar is in meters. The z-axis is shown with vertical exaggeration.

6.5 RESULTS

6.5.1 Borehole Measurements

Flow path geometry from the GPR data discussed below in section 6.5.2 can be compared with injection locations and fluid discharge locations to provide ground-truth. Figure 6.7 shows that borehole (fluid injection) locations are at (across-slope position in mm, downslope position in mm) (2943, 5500) and (3985, 5500) for Boreholes 3 and 4, respectively. Water was injected into Borehole 3 and water with tracer was injected into Borehole 4. Boreholes 1 and 2 were not used to inject liquid. Fluid collection locations downslope were near x-axis positions 750, 1600, and 3100 corresponding to major outlet flow channels. Other minor flow outlets were near x-axis locations: -300 and -750 east of the survey area, 1150–1350, 2400, 2500, and 2800.

Depth to the fracture was measured at the boreholes using a wooden dowel with a nail hammered perpendicularly into one end, to feel for the top and bottom of the fracture. In addition to boreholes drilled at the top of the survey area, four boreholes (Boreholes 5-8) were drilled down-slope. Depth of the borehole, depths to the top and bottom of the fracture, two-way travel time to the top of the fracture reflection in the GPR data, and borehole position coordinates are summarized in Table 6.3. The fracture was not physically detected in Boreholes 2 and 8 because the boreholes did not intersect the fracture. The bottom of the fracture was about the same depth as the top in Boreholes 1, 4, 5, and 6. Where the fracture was detected but not measurable with the wooden dowel technique, aperture is assumed to be 1 mm or less (Boreholes 1, 4, 5, and 6). The bottom of the fracture was at deeper depths than the top in Borehole 3 and 7, respectively, indicating larger fracture apertures than at other borehole locations. Aperture increases by over an order of magnitude at Boreholes 3 and 7, where apertures are measured at 21 and 30 mm, respectively. Borehole 3 and 7 are near the center of the survey area.

Table 6.3 Summary of borehole measurements. The fracture was not physically detected in Boreholes 2 and 8 because the boreholes did not intersect the fracture. Fracture reflection is the approximate two-way travel time in nanoseconds where the fracture event begins in the GPR data at that location. X- and Y-coordinates for Boreholes 5 - 8 are approximate.

	Depth of borehole (mm)	Depth to top of fracture (mm)	Depth to bottom of fracture (mm)	Fracture reflection (2-way tt) (ns)	Borehole Coordinates (mm) X	Y
Borehole 1	784	774	774	12.5	980	5500
Borehole 2	550	-	-	11.5	1995	5500
Borehole 3	606	585	606	9.8	2943	5500
Borehole 4	546	495	495	8.2	3985	5500
Borehole 5	517	482	482	8.0	1000	2500
Borehole 6	495	445	445	7.3	2000	2500
Borehole 7	419	389	419	6.8	3000	2500
Borehole 8	285	-	-	5.7	4000	2500

Two-way travel times to the top of the fracture reflection event were estimated from GPR data at each borehole location. This information was used with the borehole measurements to estimate the velocity of the GPR waves in the granite at this site. The average velocity of the granite was calculated at 0.120 m/ns, which is in the range of values published in the literature (Davis and Annan, 1989; and Reynolds, 1997). The second reflector seen in the GPR data at Profile 1 occurs at a two-way travel time of 11.7 ns at Borehole 3. Using calculated granite velocity, the second reflection event occurs 703 mm below the ground surface. Borehole 3 was only drilled to 606 mm depth; therefore, it does not intersect this reflector, which may be associated with another fracture. A second deeper reflector is not evident in the GPR profiles at the remaining borehole locations. Borehole 2 was not drilled deep enough to intersect the primary fracture, accounting for the lack of fluid flow at this location. Borehole 8 was also not drilled deep enough to intersect the primary fracture.

Profiles near Boreholes 3 and 7 show evidence of two reflections from the primary fracture. Wavelengths in the liquids at these locations should be on the order of

fracture aperture and the thin-layer reflection coefficient (Equation 5.2) would no longer apply. In this case, Equation 6.4 would be used to model reflections from the top and bottom of the fracture. Distinct separation of reflections from the top and bottom of the fracture would be evident. Fracture aperture could be calculated by estimating the velocity of the waves in the liquid provided the fracture is completely saturated. Calculations of aperture from reflections on traces at Boreholes 3 and 7 (Figure 6.11) indicate the fracture aperture should be around 13.5 and 17 mm, respectively, rather than 21 and 30 mm, respectively, as physically measured in the boreholes. Therefore, the fracture is not saturated and an air gap exists above the fluid in the fracture. This air gap may also be responsible for the lack of 180^{o} phase shift in GPR signals between background and liquid injection surveys at some locations. Additionally, the fracture was probably not dry at the time the background surveys were run due to heavy rains the night before the surveys. A thin film of rainwater may also be responsible for the lack of 180^{o} phase shift in the GPR data.

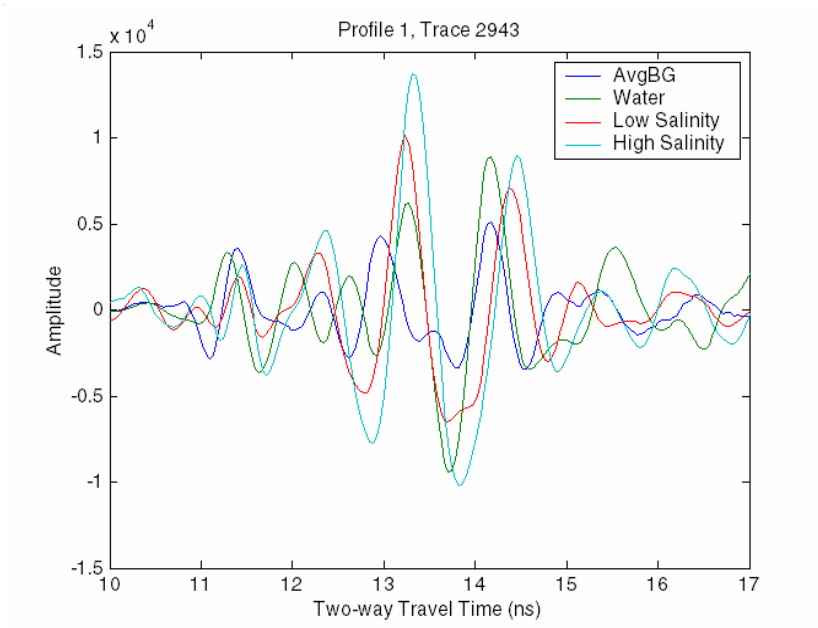

(a)

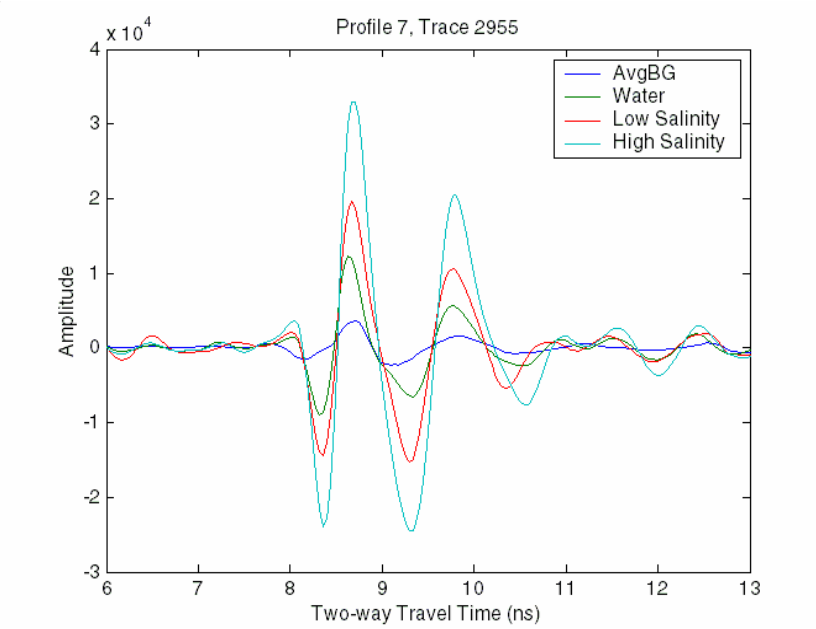

(b)

Figure 6.11 Traces near Boreholes a) 3 and b) 7, where fracture aperture is large.

6.5.2 Flow Channels

Correlation between the same traces on profiles taken during different fluid injections is expected to be small in regions of fluid flow. On Figure 6.12 and Figure 6.13 (fracture pseudo-surface) regions of low correlation (indicated by black dots) are displayed for various injection fluids. These regions are interpreted as defining flow path geometry for water only (Figure 6.12), low salinity tracer (Figure 6.13a) and high salinity tracer (Figure 6.13b). Figure 6.12 shows the extent to which water fills the fracture. Figure 6.13 a) and b) show smaller features that reflect changes from water to each saline tracer (low and high salinity, respectively). These smaller features are interpreted as transport channels within mostly water filled fractures.

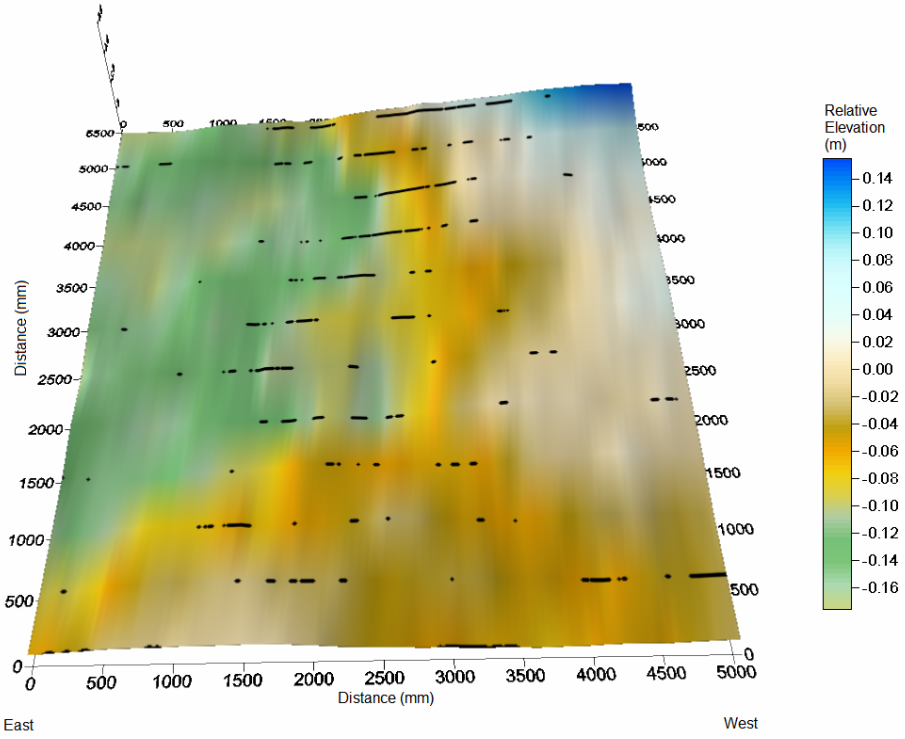

Figure 6.12 Fracture pseudo-surface with regions of low correlation (indicated by black dots) displayed for injection of water only. These regions are interpreted as defining flow path geometry for the water and show the extent to which water fills the fracture.

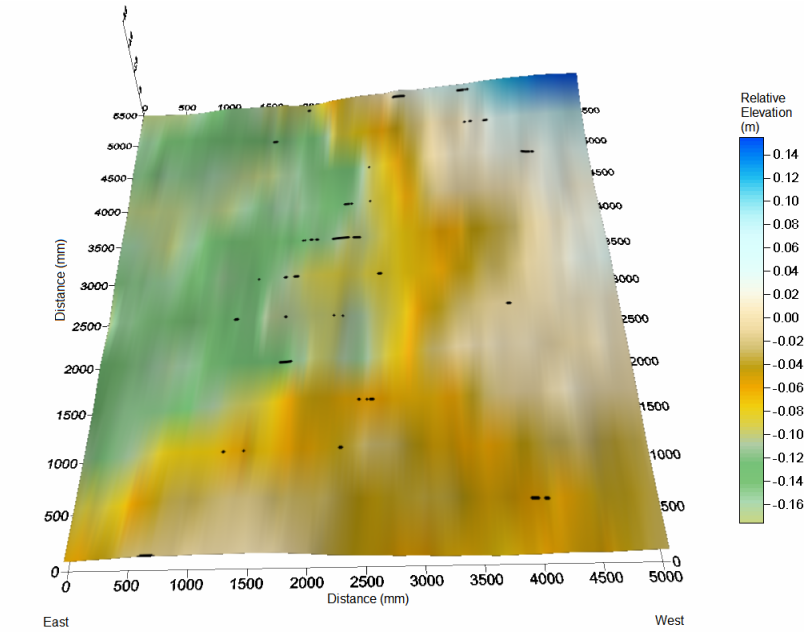

(a)

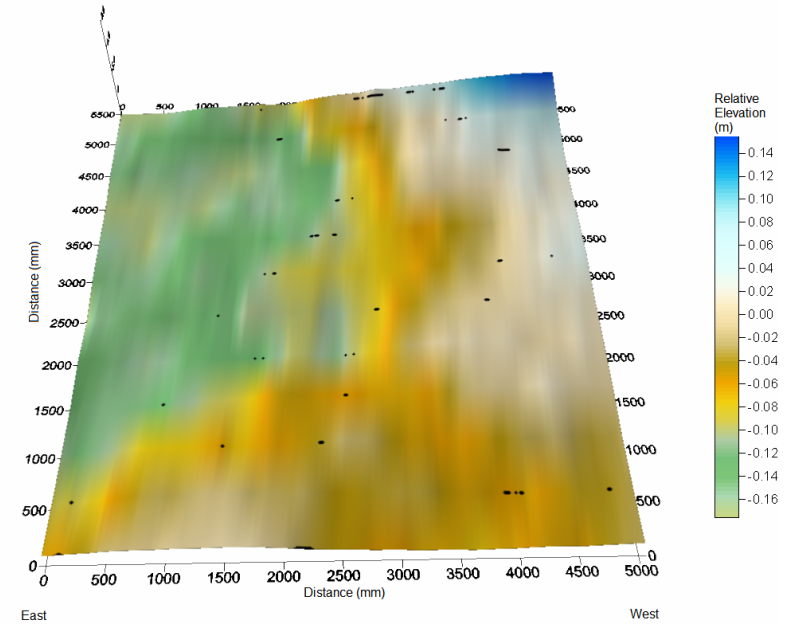

(b)

Figure 6.13 Fracture pseudo-surface with regions of low correlation (indicated by black dots) displayed for injection of a) water and low salinity tracer and b) water and high salinity tracer. These regions are interpreted as defining flow path geometry for the tracers and reflect changes from water to each saline tracer.

Figure 6.12 and Figure 6.13 show fluid concentrated near the center of the survey. Some fluid from Boreholes 3 and 4 flows down gradient in an across-slope direction in the upper survey area before flowing out towards the east. However, most fluid flows from south to north despite a stronger west to east gradient. This may be due to larger aperture near the center of the survey and the fracture may not be open in some areas. Sediment such as clay and organic matter may clog the fracture. Flow channels tend to spread out in the bottom part of the survey area as fracture surface gradient diminishes. Fluid indicated near location (4000, 500) may be flowing out of the survey area upslope of this location. The bottommost data at 0 on the y-axis (Profile 12) are ignored due to poor correlation of the initial (dry) surveys.

6.5.3 Tracer Tests

Major flow channel fluids were sampled at locations: A) 750 mm, B) 1600 mm, and C) 3100 mm along the x-axis of Figure 6.12 and Figure 6.13 for tracer test analysis (plot of relative locations on Figure 7.1). Figure 6.14 shows normalized tracer concentration versus time at A, B, and C. Tracers include cesium (Cs) and chloride (Cl) providing non-conservative (sorbing) and conservative (non-sorbing) tracers, respectively. Figure 6.14 shows the greatest concentration of tracer at location B, with C being a close second (near the center of the survey area). Concentration at A is significantly less. Additionally, bimodal behavior is seen at B and C but a single event for location A. At B and C, concentrations increase sharply and are followed by long tailings. These results indicate that the tracers are dispersive and transport channeling does occur. Lack of a bimodal event in channel A may be due to dispersion or other factors beyond the scope of this experiment. See Garner (2007) for details of tracer tests from this experiment and how channeling affects transport in fractures. An interpretation of flow path geometry from this experiment is shown in Chapter 7, Figure 7.1.

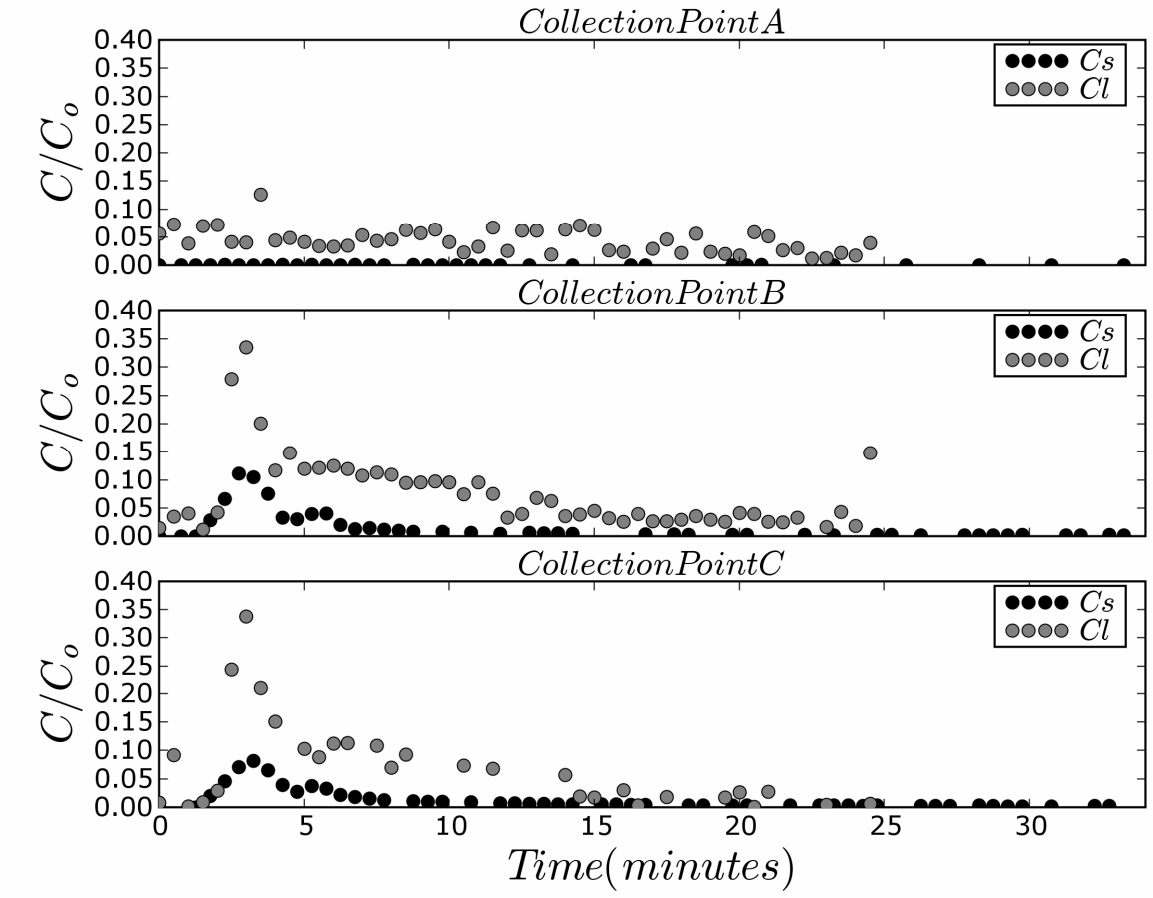

Figure 6.14 Plots of normalized tracer concentration over time at locations A, B, and C. Tracers include cesium (Cs) and chloride (Cl) for reactive and conservative tracers respectively.

6.6 CONCLUSIONS

This study demonstrated the applicability of GPR to evaluate flow in fractured rock in a field setting. Spatial variations in concentration are controlled by fluid channel geometry. Channeling of liquid rather than a plume of liquid or sheet flow is clearly evident in the GPR data. Transport channeling or channeling of tracers within water filled channels is also apparent. Changes in radar reflections can be quantitatively associated with changes in fracture filling material (air, fresh water, low salinity tracer, and high

salinity tracer). Mapping these changes throughout the survey area reveals the geometry of the flow path of each injected liquid. Low and high salinity tracers take relatively the same path for the concentrations used in this experiment. Independent tracer test results confirm transport channeling and that the tracers are concentrated near the center of the survey area, where fracture apertures are large.

Chapter 7: Conclusions

7.1 Summary of Goals and Questions

Estimates of fracture parameters are of interest in both reservoir characterization for hydrocarbon production and in subsurface pathway description for groundwater flow and contaminant migration studies. This study employs two different types of field experiments designed to estimate fracture parameters. One study uses 2D multicomponent seismic data and has the goal of observing the influence of fractures on seismic wave speeds (seismic anisotropy) and relating observed effects to fracture orientation, density, and filling material. The second study employs ground penetrating radar (GPR) data to provide direct images of fractures and details of their aperture and fluid flow geometry. The field experiments using multicomponent seismic data and GPR conducted in this research improve characterization of fracture parameters in their natural setting.

General scientific questions that motivated this work included the following: What are the fracture parameters of the Edwards limestone in this area? What is the connection between fractures from field measurements in outcrop and seismic observations, which are at very different scales? What are the similarities and differences between the three-component (3C), sledgehammer data and the nine-component (9C), Vibroseis data? What wave types are useful in characterizing fractures? What value is there in multicomponent receivers and sources? Do results from the seismic field experimental confirm results from lab and theoretical studies? What are the fracture and flow parameters at the Buchanan site? Is radar a useful tool for in situ experiments of natural fracture flow? What strategies for radar studies, such as geometry and data processing, are useful?

7.2 SEISMIC EXPERIMENT

I independently developed a successful multicomponent seismic field testing program. This development included: making connections with the City of Austin for permission and access to Stoneledge Quarry, organizing and conducting the field work for both the sledgehammer and Vibroseis surveys, collecting fracture data from field scan line measurements, and multicomponent data processing and analysis. This experiment measures seismic velocities for body (P, SV, and SH) and Rayleigh waves and yields more information about the subsurface than traditional methods and previous research. A summary of all seismic velocity values from both experiments and other anisotropy measurements are shown in Table 7.1 and Table 7.2, respectively. Vibroseis data velocities for P, SV and SH are from the matched components. Rayleigh wave velocities are from the vertical source, vertical receiver component. Depth to the water table is the average of depths from intercept time calculations. Vp/Vs, Poisson's ratio, and fracture density are calculated from half-space velocities.

Table 7.1 Summary of seismic velocity values.

		Layer	Sledgehammer Source	Vibroseis Source
Line 1 N13W	**Direct P-Wave Velocity (m/s)**	1	1399	1397
	P-Wave Refractor Velocity (m/s)	2	5740	5739
	SV-Wave Refractor Velocity (m/s)	2	3026	3049
	SH-Wave Refractor Velocity (m/s)	2	n/a	3031
	Rayleigh Wave Velocity (m/s)	1: near-offsets	n/a	n/a
	Rayleigh Wave Velocity (m/s)	2: far-offsets	2121	2100
Line 2 N88E	**Direct P-Wave Velocity (m/s)**	1	1606	1616
	P-Wave Refractor Velocity (m/s)	2	5700	5700
	SV-Wave Refractor Velocity (m/s)	2	3095	3088
	SH-Wave Refractor Velocity (m/s)	2	n/a	3162
	Rayleigh Wave Velocity (m/s)	1: near-offsets	878	887
	Rayleigh Wave Velocity (m/s)	2: far-offsets	1920	1931
Line 3 N30E	**Direct P-Wave Velocity (m/s)**	1	2004	2011
	P-Wave Refractor Velocity (m/s)	2	5733	5729
	SV-Wave Refractor Velocity (m/s)	2	3175	3176
	SH-Wave Refractor Velocity (m/s)	2	n/a	3017
	Rayleigh Wave Velocity (m/s)	1: near-offsets	960	960
	Rayleigh Wave Velocity (m/s)	2: far-offsets	1834	1835

Table 7.2 Additional measurements from velocity anisotropy analyses.

	Hammer Data	Vibroseis Data
Water Table Depth (m)	27.4	27.2
Vp/Vs	1.81	1.80
Poisson's Ratio	0.28	0.28
Fracture Density	0.044	0.047

Results indicate that the orientation of the primary fracture set is at N39E and is roughly parallel to the orientation of acquisition Line 3. Results demonstrate that the seismic data respond to anisotropy caused by regional faulting. Groundwater flow direction has been observed by others to be across this fault trend and parallel to a secondary fracture orientation at the site. Seismic data do not show evidence of this secondary fracture set. This may be because the flow experiments by others simply measure a deeper portion of the Edwards Aquifer. Geophone azimuth was found to be

more sensitive to shear wave polarizations than acquisition line azimuth. It is useful to understand that when estimating fracture orientation from shear wave velocity anisotropy, precise orientation of the geophones is more critical in the Alford rotation analysis than azimuth of the acquisition line.

Depth to the water table has been estimated as the depth at which P velocity increases significantly using conventional refraction methods. This is inferred to be the water table depth, though it may also, or in addition, correspond to a change in lithologic properties. Some variability in lithologic properties is evident laterally, as indicated by the absence of the very low speed (~900 m/s) Rayleigh wave along Line 1. Some variation in the vertical might also be expected, possibly due to variations in weathering and dissolution in the unsaturated zone, relative to deeper more frequently saturated regions. P-wave velocities are expected from theory to be greatly affected by water-filled fractures. However, in this case, the increase in P velocity with depth is larger than anticipated from fracture theory. Examples given in Chapter 3 suggest P velocity might increase by 15% from dry to saturated fractures (at 5% fracture density for 0^{o} incidence angle with the fracture normal), while an increase of nearly 3 to 4 times from the unsaturated low speed layer to the half-space is observed in this case. Presumably some of the increase is associated with the water table. However, the very low velocities measured suggest that the top layer is not only unsaturated, but also more weathered or otherwise altered. Shear waves are expected to be unaffected by the transition from dry to saturated fractures. Thus, the presence of a very slow Rayleigh wave associated with the upper layer is consistent with the view that lithologic and weathering variations, rather than just a transition from dry to wet conditions, is the cause of the rapid Vp increase with depth. For the half-space, Vp/Vs and Poisson's ratio from seismic data indicate a

dolomite lithology, which agrees with Stoneledge Quarry being in the dolomitic member of the Edwards Group.

Techniques used to average measurements of fracture density in the field are not standard and there may be biases resulting from the particular choices in the measurements. Furthermore, the scan lines were measured along deeply excavated surfaces, and may not reflect at all the properties of the nearer surface, lower speed layer seen in the seismic data. Fracture density from scan lines is estimated to be about 1%. A one standard deviation confidence interval (containing about 2/3 of the total number of measurements) is estimated to be approximately 0.2% to 5%. To relate these observations to seismic data, a first point is that the theory of fracture density effects on seismic data is based on several assumptions such as crack shape that may not be representative of actual conditions. Additionally, fracture density as measured from seismic waves in this study does not account for porosity within the matrix, which may be as high as 30%. However, fracture density estimates from the seismic data are around 5% and consistent with the high end of the confidence interval from scan line data. The high values from the seismic data may be due to the incorporation of matrix porosity measured with seismic waves. Fractures are observed in outcrop at the millimeter to meter scale and the seismic anisotropy they induce is measured by wavelengths at meter to tens of meters scale. This is undoubtedly a major source of differences in estimates.

Results are consistent for Vibroseis and sledgehammer sources. However, the Vibroseis data show much better signal-to-noise ratios than the hammer data. Additionally, 9C Vibroseis data contain more information than 3C hammer data, specifically SH arrivals. Matched source components contain useful information due to their higher signal to noise ratios. P, SV, SH and Rayleigh waves are the effective wave types in these components. Unmatched source and receiver components added

information by confirming arrival picks, providing additional confirmation of velocities from arrivals. P wave velocity variations due to anisotropy may be small for small fracture densities under saturated conditions. Constraining velocities using other components adds confidence to these subtle variations. The hammer data contain a broader range of frequencies but each source provided similar results. Results from this field experimental generally agree with results from lab and theoretical studies.

This study shows that relatively simple seismic experiments may be used to gain a general understanding of fracture parameters in areas where in situ measurements may not be possible. Additionally, seismic methods allow characterization over a broader area and at deeper depths than typical point measurements from well or outcrop data. Seismic waves are useful for characterizing subsurface fracture parameters of orientation, density and filling-material. Fracture orientation influences flow direction and fracture density is related to porosity leading to flow volume. These are important hydraulic parameters for natural resources like oil and gas from reservoir characterization and groundwater from aquifer characterization.

Additional investigations that might extend the understanding of the seismic data in this case include 1) further theory of velocity anisotropy that includes matrix porosity, and 2) Rayleigh and other modal surface wave velocity variations with azimuth in the presence of fractures.

7.3 GPR EXPERIMENT

This experiment demonstrated that GPR could be effective in delineating flow path geometry and in estimating fracture aperture. Understanding path geometry leads to more accurate estimates of spatial variations in concentration and measures of aperture lead to estimates of flow volume. These parameters are important for understanding solute transport. This experiment was developed in collaboration with Hydrogeologist,

Terence Garner, to integrate goals of parallel research on characterizing transport properties in fractures. My contribution included development of the radar survey to meet the joint goals of the radar experiment and the tracer tests. I also performed the GPR and Total Station data acquisition, processing, and interpretation independently. Terence provided the tracer test results and his interpretation of channel geometry from the GPR results is shown in Figure 7.1. Parameters of fracture aperture and radar velocity in the Buchanan Dam granite found from this experiment are shown in Table 7.3.

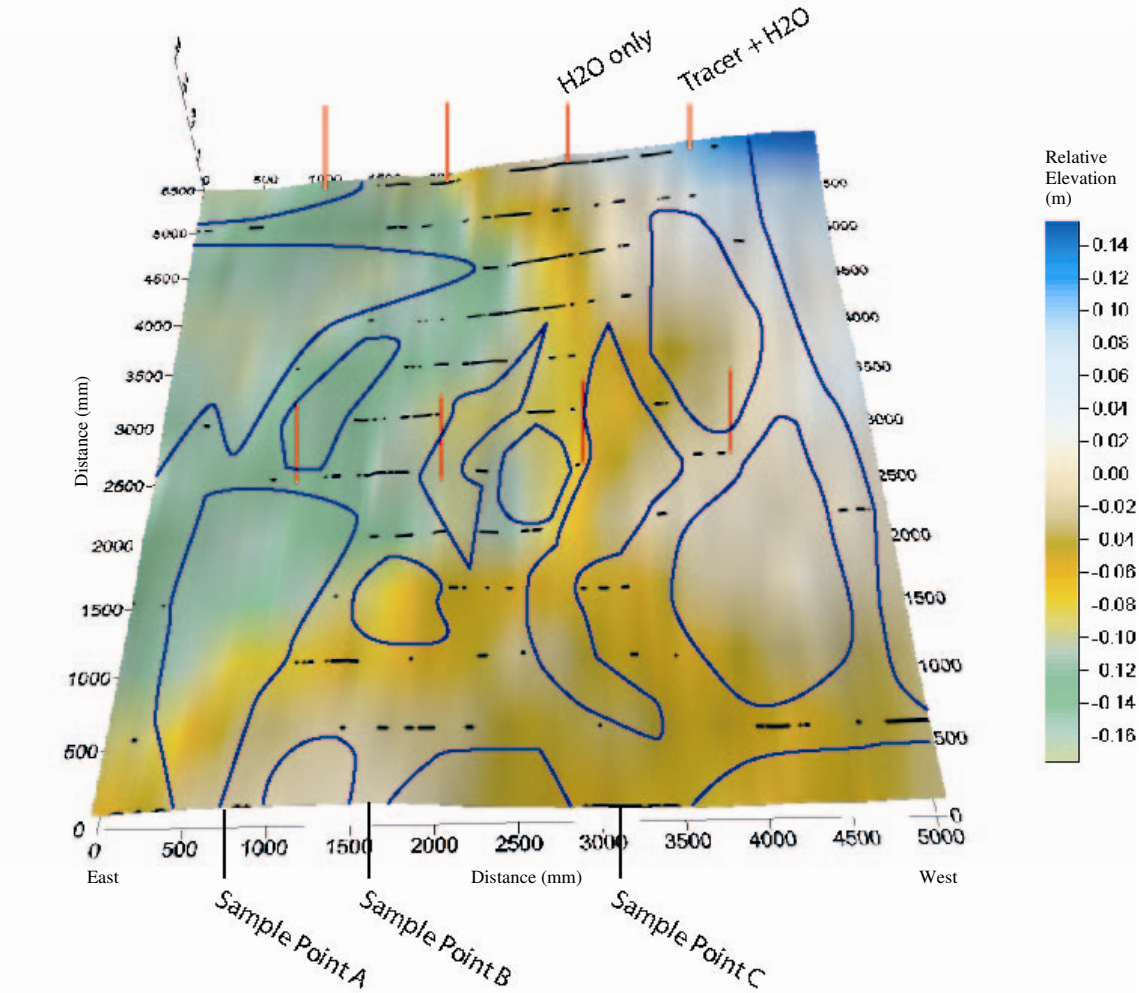

Figure 7.1 One interpretation of flow channeling from GRP results for water only injections. x- and y-axes are in mm. Color bar is relative elevation in m. Borehole locations (red lines) and relative tracer sample points are indicated.

Table 7.3 Parameters found from this experiment.

Aperture Range (mm)	0 - 30
Granite Velocity (m/ns)	0.12

GPR has proven to be an effective tool for in situ experiments of natural fractures as shown by this experiment and other studies. When conducting high frequency experiments such as this, attention must be paid to accurate survey geometry and details of data processing. Survey parameters based on results of equations given in Sensors &

Software (1992) proved applicable at the high frequencies used in this experiment. Additionally, choosing optimal system response parameters as specified by the manufacturer provided good results. Profile direction was perpendicular to the dominant direction of expected flow and antennas were positioned parallel to this direction to give greatest reflection from the fluids.

Spatial variations in concentration are controlled by fluid channel geometry, as demonstrated in this experiment. The GPR results show clear evidence of both flow and transport channeling. For the high frequencies used in this experiment, amplitude changes alone are not diagnostic of fracture-filling fluid as with other studies using lower frequencies. However, changes in radar signal are quantitatively associated with changes in fracture filling material (air, fresh water, low salinity tracer, and high salinity tracer) through the innovative technique using correlation of signals. Because all parameters except filling fluid remain the same from one GPR pass to another, poor correlations in signal indicate changes in filling fluid. Therefore, data processing techniques using correlations prove to be successful for identifying fluid changes. Also, the geometry of the flow path of each injected liquid is revealed by mapping correlation changes throughout the survey area. Transport channeling and concentration of tracer towards the center of the survey area where fracture apertures are large was confirmed by independent tracer test results. Additionally, results indicate that the low and high concentration tracers used in this experiment travel along the same general flow paths.

Fracture aperture can be calculated by estimating the velocity of the waves in the liquid provided the fracture is completely saturated. Calculations of aperture from GPR data at locations of known aperture do not agree with physical measurements. Therefore, the fracture is not saturated and an air gap exists above the fluid in the fracture. These results indicate that aperture estimates from these data cannot be determined accurately.

However, GPR data should give accurate estimates of fracture aperture provided wavelengths within the fracture are small relative to aperture.

Appendix A: Scan line Data and Analyses

Measurements of fracture spacing, orientation, and aperture were taken along 3 scan lines on the quarry wall and floor. The first line (not to be confused with seismic acquisition lines) was 3.6 m long on a quarry wall, another line was 4.54 m on the quarry floor and a final line was 2.41 m on the quarry floor. The values from the scan line data are shown in Tables A.1 through A.3 corresponding to scan lines 1 through 3, respectively. When dip could be measured, it was vertical or near-vertical.

Table A.1 Measurements made on scan line 1, collected on the quarry wall.

Line 1 Spacing (m)	Aperture (mm)	Distance (m)	Strike (degrees)
0	0	0.5100	35.0000
0.0200	0.9500	0.5300	40.0000
0.0500	0	0.5800	55.0000
0.0300	0.5500	0.6100	90.0000
0.1900	0.3500	0.8000	85.0000
0.0600	1.0000	0.8600	30.0000
0.1000	0.2000	0.9600	55.0000
0.0700	0	1.0300	40.0000
0.0700	0.0400	1.1000	80.0000
0.2500	0.2000	1.3500	25.0000
0.3500	0	1.7000	55.0000
0.0400	1.0000	1.7400	45.0000
0.1100	0	1.8500	40.0000
0.0500	0.1500	1.9000	-65.0000
0.0300	0.4000	1.9300	55.0000
0.0500	0.4000	1.9800	-69.0000
0.0200	0	2.0000	39.0000
0.0200	0.4500	2.0200	25.0000
0.0400	0.2000	2.0600	35.0000
0.0200	0.6000	2.0800	30.0000
0.1000	0.2000	2.1800	26.0000
0.0200	0.2500	2.2000	10.0000
0.0800	0.2000	2.2800	40.0000
0.0700	0.1000	2.3500	35.0000

0.1800	0.7500	2.5300	50.0000
0.0100	0.7500	2.5400	50.0000
0.0900	0.4500	2.6300	36.0000
0.0500	0	2.6800	29.0000
0.0800	0.3000	2.7600	20.0000
0.0100	2.0000	2.7700	45.0000
0.0100	2.0000	2.7800	30.0000
0.0200	0.2000	2.8000	-70.0000
0.1500	0	2.9500	30.0000
0.0300	0.8500	2.9800	45.0000
0.0300	0.8500	3.0100	35.0000
0.1900	0.3000	3.2000	25.0000
0.0500	3.0000	3.2500	85.0000
0.0900	0.6000	3.3400	30.0000
0.1700	0.2000	3.5100	40.0000
0.0900	1.0000	3.6000	20.0000

Table A.2 Measurements made on scan line 2, collected on the quarry floor.

Line 2 Spacing (m)	**Aperture (mm)**	**Distance (m)**	**Strike (degrees)**
0	0.7500	9.0940	23.0000
0.0050	0.4000	9.0990	30.0000
0.0110	0.2700	9.1100	47.0000
0.0400	1.4000	9.1500	40.0000
0.1160	0.5000	9.2660	18.0000
0.0570	0.9500	9.3230	28.0000
0.0190	1.1500	9.3420	20.0000
0.1780	0.7500	9.5200	22.0000
0.1800	2.6500	9.7000	4.0000
0.2800	1.7500	9.9800	12.0000
0.1800	2.1500	10.1600	22.0000
0.1140	0.5000	10.2740	18.0000
0.5360	0.6200	10.8100	54.0000
0.0360	0.4000	10.8460	42.0000
0.0060	0.5000	10.8520	29.0000
0.0480	2.6500	10.9000	9.0000
0.0880	0.5000	10.9880	32.0000
0.0090	0.5000	10.9970	50.0000
0.1740	0.6200	11.1710	39.0000
0.6290	1.4000	11.8000	28.0000
0.0620	0.7500	11.8620	43.0000

0.1140	0.9500	11.9760	34.0000
0.2180	0.2700	12.1940	28.0000
0.1640	0.4000	12.3580	52.0000
0.2530	1.7500	12.6110	46.0000
0.0320	1.4000	12.6430	44.0000
0.3480	0.1800	12.9910	96.0000
0.1990	0.7500	13.1900	45.0000
0.0620	0.1200	13.2520	45.0000
0.1920	0.6200	13.4440	42.0000
0.1290	0.6200	13.5730	40.0000
0.0560	0.5000	13.6290	44.0000

Table A.3 Measurements made on scan line 2, collected on the quarry floor.

Line 3			
Spacing (m)	**Aperture (mm)**	**Distance (m)**	**Strike (degrees)**
0	0.6200	1.1600	65.0000
0.0800	1.4000	1.2400	72.0000
0.0700	0.7500	1.3100	52.0000
0.0800	0.0400	1.3900	57.0000
0.0040	0.0400	1.3940	32.0000
0.0070	0.0400	1.4010	29.0000
0.0200	0.0400	1.4210	-5.0000
0.0690	1.0000	1.4900	37.0000
0.0420	0.5000	1.5320	14.0000
0.1020	1.5000	1.6340	54.0000
0.0500	0.1000	1.6840	10.0000
0.0020	0.1000	1.6860	15.0000
0.1340	0.0100	1.8200	28.0000
0.1660	0.0100	1.9860	15.0000
0.0100	0.0100	1.9960	22.0000
0.0940	0.1000	2.0900	-17.0000
0.0220	0.0500	2.1120	10.0000
0.1730	5.0000	2.2850	20.0000
0.0180	0.0400	2.3030	30.0000
0.0470	0.1000	2.3500	38.0000
0.0660	0.0400	2.4160	35.0000
0.0300	1.0000	2.4460	33.0000
0.0550	0.5000	2.5010	33.0000
0	0.5000	2.5010	-75.0000
0.0500	0.5000	2.5510	-5.0000
0.1510	0.5000	2.7020	-5.0000

0.0470	0.1000	2.7490	40.0000
0.1030	4.0000	2.8520	29.0000
0.0350	0.1000	2.8870	22.0000
0.0600	1.0000	2.9470	23.0000
0.0840	0.5000	3.0310	14.0000
0.0180	0.5000	3.0490	25.0000
0.0190	1.0000	3.0680	-84.0000
0.0860	0.5000	3.1540	18.0000
0.1090	6.0000	3.2630	33.0000
0.0310	1.5000	3.2940	27.0000
0.0080	0.1000	3.3020	28.0000
0.2680	0.1000	3.5700	57.0000

The mean aperture from all scan lines is 0.72 mm and the mean spacing is 0.0912 m. Thus the mean spatial frequency is 10.96 fractures/m, implying a mean fracture density is the product frequency (fractures/m) times aperture (m/fracture). This is equal to 0.0079, slightly less than 1% fracture density (or equivalently porosity) in this simple analysis.

A second simple estimate comes from the sum of all fracture apertures in all scan lines divided by the sum of all scan line lengths. The sum of apertures on all 3 lines is 79.1 mm and the sum of all line lengths is 10.55 m. Therefore, the average is 7.49 mm/m or 0.0075 effective fracture porosity, again, just below 1%. A summary of fracture strikes for all 3 lines is given in Figure A.1.

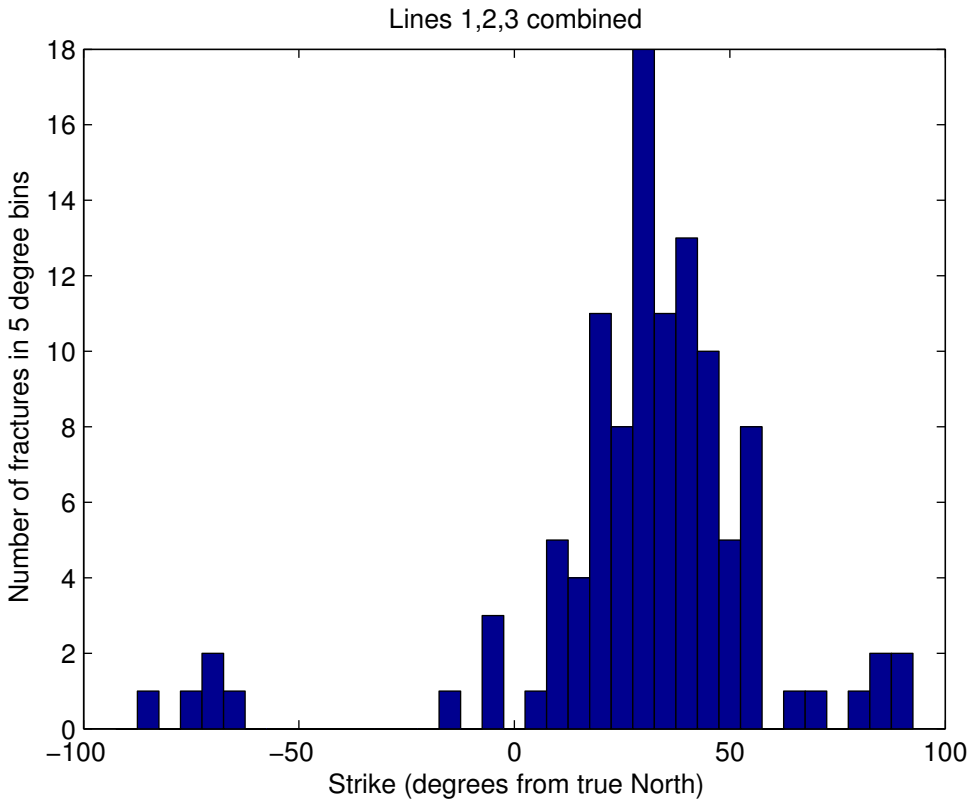

Figure A.1 Summary of fracture strikes for all 3 lines.

Fracture strikes are dominantly in the range 0 to 60 and the histogram suggests a normal distribution of strike for the main set of fractures. The mean of all strikes in this range (0 to 60) is 30.65 degrees and the mode of the histogram (with 18 counts) is the bin centered on 30 degrees. There are few fractures outside this range (0 to 60) and, as Figure A.2 shows, these few are relatively small in aperture. The largest apertures tend to cluster at a strike around 30 degrees.

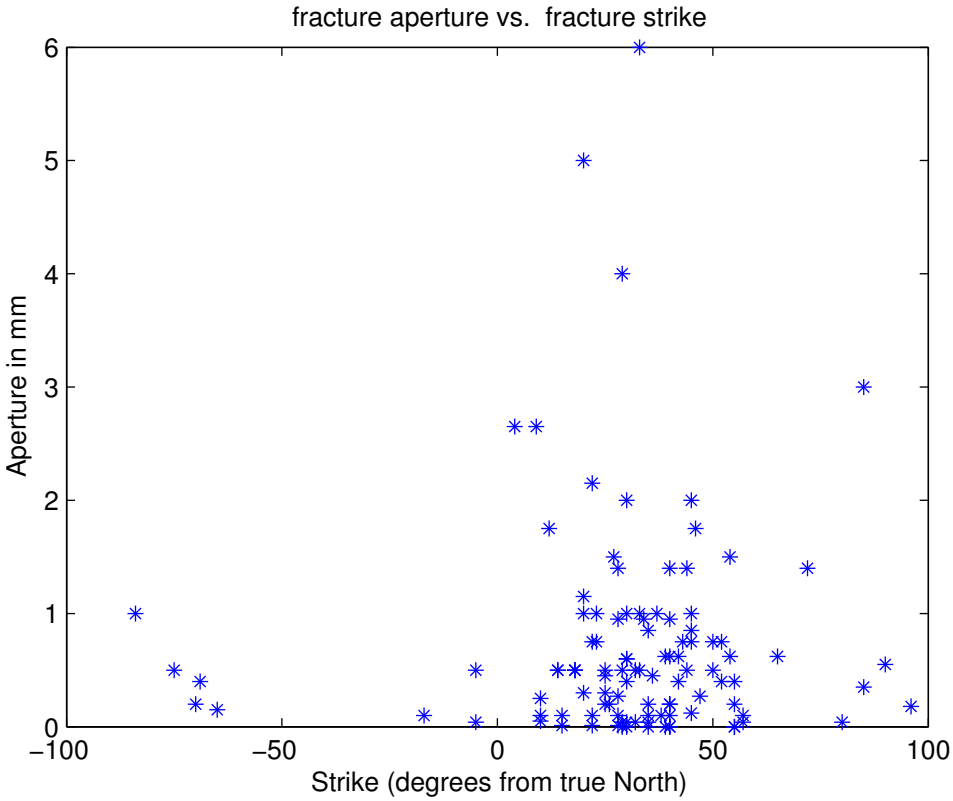

Figure A.2 Fracture aperture versus fracture strike from all three scan lines.

Thus, the field evidence indicates that the principal fractures that are likely to influence seismic wave speeds are those oriented at N30E. The small numbers at other strikes tend to have small apertures and presumably would not dominate seismic anisotropy.

Finally, I address the question of finding the distribution of fracture density, the parameter used in anisotropy theory. As noted above, two simple estimates are slightly below 1% (0.0079 is the product of reciprocal of mean fracture spacing and mean fracture aperture and 0.0075 is from the sum of all apertures divided by scan line lengths). Fracture spacing and aperture are random variables, so fracture density will be as well. The central limit theorem predicts that the sum of independent random variables

will tend to be normally distributed. It can be extended to predict the distribution of the product of random variables by observing that the logarithm of a product is the sum of the logs of the factors. Therefore, the log of a product of random variables that take only positive values tends to have a normal distribution. The product itself has a log-normal distribution.

This proposal can be tested by forming the product of aperture and fracture frequency for each fracture and taking the logarithm. At each fracture, fracture density is fracture aperture multiplied by the reciprocal of average distance to the two adjacent fractures. Each fracture then provides a realization of the random variable and I examine the distribution of this as well as its logarithm. The histogram of this variable is shown in Figure A.3. The log base 10 of this has the histogram shown in Figure A.4, which has a Gaussian (normal) appearing distribution.

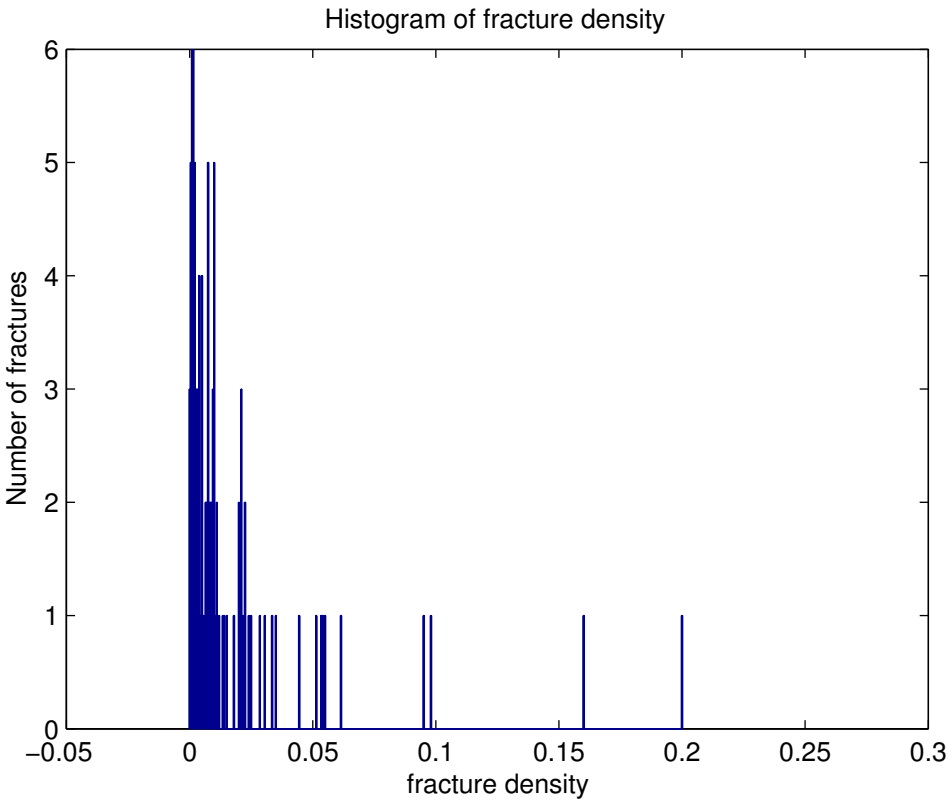

Figure A.3 Histogram of fracture density.

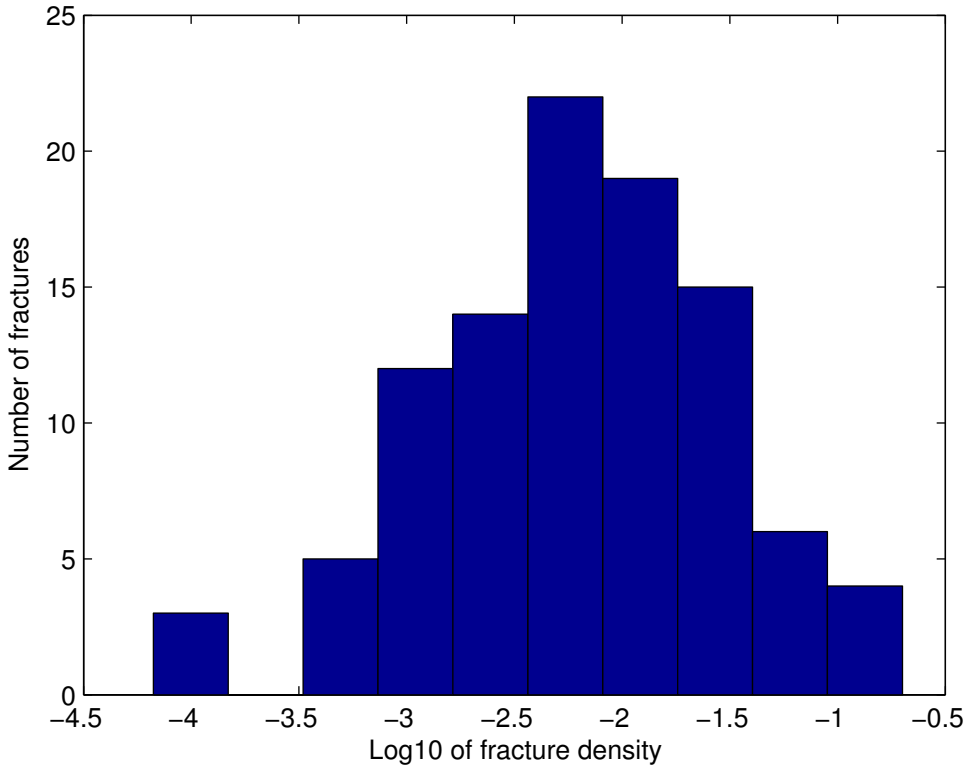

Figure A.4 The log base 10 histogram of Figure A.3 above.

The conclusion is that fracture density (equivalent to fracture porosity) is about 0.01 (around 1%), consistent with the mean estimates above. I can estimate a one standard deviation confidence interval from the four central bins, which together hold about 75% of the total number of measurements (a true 1 standard deviation is 68%, so this is only approximate). The range is -2.75 to -1.3 or raising 10 to these powers I get a confidence interval of (approximately) 0.2% to 5%. These provide a range of values to compare with anisotropy theory.

Appendix B: Anisotropy and Synthetic Seismograms

B.1 ANISOTROPIC ELASTICITY TENSOR

Anisotropy of a medium can be expressed using the elastic coefficient or stiffness matrix (C), which describes the relation between stress and strain within the medium from modified Hooke's Law relating the six independent components of the stress tensor to the 6 components of the strain tensor. This matrix contains 36 elements but is reduced to 21 independent coefficients due to symmetry as shown in Equation B.1.

$$\mathbf{C} = \begin{bmatrix} c_{11} & c_{12} & c_{13} & c_{14} & c_{15} & c_{16} \\ c_{12} & c_{22} & c_{23} & c_{24} & c_{25} & c_{26} \\ c_{13} & c_{23} & c_{33} & c_{34} & c_{35} & c_{36} \\ c_{14} & c_{24} & c_{34} & c_{44} & c_{45} & c_{46} \\ c_{15} & c_{25} & c_{35} & c_{45} & c_{55} & c_{56} \\ c_{16} & c_{26} & c_{36} & c_{46} & c_{56} & c_{66} \end{bmatrix} \qquad \text{B.1}$$

These 21 coefficients can further be reduced in number for special cases. One common example is a transversely isotropic (TI) medium. A TI medium is isotropic in a direction transverse to a symmetry axis but may be anisotropic in other directions. This type of symmetry is common in the earth. Horizontal bedding, aligned fractures or cracks, and oblate grains with similar orientation like clay are observed to behave as TI media. If the axis of symmetry is horizontal as in a vertically fractured material, the medium is known as HTI, meaning that at the surface, wave speeds vary with azimuth. For a vertical axes of symmetry (example: horizontal bedding planes), the medium is known as VTI. TI media have only 5 independent elastic coefficients as shown in Equation B.2.

$$\mathbf{C}=\begin{bmatrix} c_{11} & c_{11}-2c_{66} & c_{13} & 0 & 0 & 0 \\ c_{11}-2c_{66} & c_{11} & c_{13} & 0 & 0 & 0 \\ c_{13} & c_{13} & c_{33} & 0 & 0 & 0 \\ 0 & 0 & 0 & c_{44} & 0 & 0 \\ 0 & 0 & 0 & 0 & c_{44} & 0 \\ 0 & 0 & 0 & 0 & 0 & c_{66} \end{bmatrix} \qquad \text{B.2}$$

Velocity can be calculated from these elastic coefficients using the equations below, which are expanded from Chapter 3.

$$\rho V_p^2(\theta)=\frac{1}{2}\left[C_{33}+C_{44}+(C_{11}-C_{33})\sin^2\theta+D(\theta)\right] \qquad \text{B.3}$$

$$\rho V_{SV}^2(\theta)=\frac{1}{2}\left[C_{33}+C_{44}+(C_{11}-C_{33})\sin^2\theta-D(\theta)\right] \qquad \text{B.4}$$

$$\rho V_{SH}^2(\theta)=C_{66}\sin^2\theta+C_{44}\cos^2\theta \qquad \text{B.5}$$

where ρ is lithologic density, θ is incidence angle, and D(θ) is compact notation for the expression in Equation B.6.

$$D(\theta)\equiv\begin{Bmatrix}(C_{33}-C_{44})^2+2\left[2(C_{13}+C_{44})^2-(C_{33}-C_{44})(C_{11}+C_{33}-2C_{44})\right]\sin^2\theta \\ +\left[(C_{11}+C_{33}-2C_{44})^2-4(C_{13}+C_{44})^2\right]\sin^4\theta\end{Bmatrix}^{1/2} \qquad \text{B.6}$$

From effective medium theory and following Schoenberg and Douma (1988), the elastic coefficient matrix is estimated in the long wavelength limit for a model of long, thin, parallel fractures in a homogeneous isotropic background. The material filling the fractures is considered to be much more compliant than the surrounding material. The model can be conveyed as averages of elastic moduli for each section of material between fractures, weighted by the distance between fractures and is found by taking the limit as these parameters jointly go to zero.

The assumptions of the long wavelength limit concern stresses on the fractures and material between fractures (sections). The assumptions are: 1) stress components acting on surfaces parallel to the fracture planes are the same in all sections and 2) over many sections, the sections move jointly, which signifies that strain components acting

on surfaces parallel to the fracture planes are the same in all sections. Other stress and strain components may vary from one section to another. In each section, the stress and strain component is the average over the width of the section. Therefore, some stress and strain components depend on the section they are in and some are independent of the section.

Schoenberg and Douma (1988) rewrite Hooke's Law in terms of three, 3x3 submatrices of C from Equation B.1 for the effective medium of parallel fractures. These submatrices are

$$\mathbf{M}_i = \begin{bmatrix} c_{11i} & c_{12i} & c_{16i} \\ c_{12i} & c_{22i} & c_{26i} \\ c_{16i} & c_{26i} & c_{66i} \end{bmatrix}, \mathbf{N}_i = \begin{bmatrix} c_{33i} & c_{34i} & c_{35i} \\ c_{34i} & c_{44i} & c_{45i} \\ c_{35i} & c_{45i} & c_{55i} \end{bmatrix}, \text{ and } \mathbf{P}_i = \begin{bmatrix} c_{13i} & c_{14i} & c_{15i} \\ c_{23i} & c_{24i} & c_{25i} \\ c_{36i} & c_{46i} & c_{56i} \end{bmatrix} \quad \text{B.7}$$

where the subscript i refers to a particular section. For VTI media, the submatrices in Equation B.7 reduce to

$$\mathbf{M}_i = \begin{bmatrix} c_{11i} & c_{11i} - 2c_{66i} & 0 \\ c_{11i} - 2c_{66i} & c_{11i} & 0 \\ 0 & 0 & c_{66i} \end{bmatrix}, \quad \mathbf{N}_i = \begin{bmatrix} c_{33i} & 0 & 0 \\ 0 & c_{44i} & 0 \\ 0 & 0 & c_{44i} \end{bmatrix}, \text{ and} \quad \text{B.8}$$

$$\mathbf{P}_i = \begin{bmatrix} c_{13i} & 0 & 0 \\ c_{13i} & 0 & 0 \\ 0 & 0 & 0 \end{bmatrix}$$

Fracture parameters are contained within N, so there are 6 or fewer independent fracture parameters in an anisotropic medium and only 2 for a VTI medium. Strain components in the fractures are large because the fractures are soft. Therefore, strain components can be approximated by the component of total slip displacement across all fractures in a given interval of a given length normalized by that length. Schoenberg and Douma (1988) termed this approximation the "fracture system compliance matrix", Z. This approximation is used rather than the exact solution because the exact solution may

cause elements of the matrix to become large or undefined for small slip or diminishing components, where Z components become very small or zero.

For a VTI fracture system, Z has the form

$$\mathbf{Z} = \begin{bmatrix} Z_N & 0 & 0 \\ 0 & Z_T & 0 \\ 0 & 0 & Z_T \end{bmatrix} \qquad \text{B.9}$$

where subscripts N and T are for normal and tangential compliances, respectively, of an average fracture of a given length or stress. For stability, Z_N and Z_T must be non-negative if the fractured medium is transversely isotropic. The submatrices of C now take on the form

$$\mathbf{M}_e = \begin{bmatrix} c_{11} & c_{11}-2c_{66b} & 0 \\ c_{11}-2c_{66b} & c_{11} & 0 \\ 0 & 0 & c_{66b} \end{bmatrix}, \quad \mathbf{N}_e = \begin{bmatrix} \dfrac{c_{33b}}{1+E_N} & 0 & 0 \\ 0 & \dfrac{c_{44b}}{1+E_T} & 0 \\ 0 & 0 & \dfrac{c_{44b}}{1+E_T} \end{bmatrix},$$

$$\text{and } \mathbf{P}_e = \begin{bmatrix} \dfrac{c_{13b}}{1+E_N} & 0 & 0 \\ \dfrac{c_{13b}}{1+E_N} & 0 & 0 \\ 0 & 0 & 0 \end{bmatrix} \qquad \text{B.10}$$

for the effective medium, where

$$c_{11} = c_{11b} - \frac{c_{13b}^2}{c_{33b}}\left[1 - \frac{1}{1+E_N}\right], \quad E_N \equiv c_{33b}Z_N, \quad \text{and} \quad E_T \equiv c_{44b}Z_T .$$

The subscript b represents the component for the background medium. E_N and E_T are the normal and tangential dimensionless compliances, respectively, that represent the fracture system compliances with respect to the compliances of the background medium. The effective elastic coefficient matrix for the entire system with an isotropic background can

be represented by only 4 parameters; background shear modulus, μb, background Lame's constant, λb, E_N, and E_T. μ and λ are related to P-wave (Vp) and S-wave (Vs) velocities, which are two parameters commonly measured from seismic data. The components in Equation B.10 are related to shear modulus and Lame's constant and in turn Vp and Vs by $c_{11b} = c_{33b} = \lambda_b + 2\mu_b = V_p^2\rho$, $c_{44b} = c_{66b} = \mu_b = V_s^2\rho$, and $c_{13b} = \lambda_b = V_p^2\rho - 2V_s^2\rho$ where ρ is lithologic density.

Following Hudson's (1981) examples for fluid-filled fractures as described in Schoenberg and Douma (1988), E_N and E_T can be calculated. Assuming no shear stress, zero tangential displacement on the interior fracture surface, and welded normal displacement across the fracture (because the aperture is small or only tangential displacement across the fracture, which is non-welded),

$$E_T = \frac{16}{3(3-2\gamma_b)}e \text{ and } E_N = 0. \qquad \text{B.11}$$

e is the fracture density equal to the number of fractures per unit volume times a^3 and $\gamma_b = \mu_b/(\lambda_b + 2\mu_b)$. a is the mean fracture radius and γ_b is the ratio of V_s^2 to V_p^2. For dry fractures, with zero normal and tangential displacements on the interior fracture surface and sufficiently large aperture to permit non-welded normal displacement across the fracture,

$$E_T = \frac{16}{3(3-2\gamma_b)}e \quad \text{and} \quad E_N = \frac{4}{3\gamma_b(1-\gamma_b)}e. \qquad \text{B.12}$$

From these relationships, the effective elastic coefficient matrix can be determined and used to model results of the full seismic waveform in anisotropic media. The only parameters needed to create synthetic seismograms for such a model are: Vp, Vs, ρ, and e. These parameters may be estimated from seismic data and field (outcrop) observations.

B.2 SYNTHETIC SEISMOGRAMS

Synthetic seismograms have been calculated using a program, which utilizes the theory described above. The input parameters and single trace results are presented below. Full seismic profiles are presented throughout the main body of this dissertation.

A half-space model is used to test the behavior and choose input parameters for the reflectivity synthetic seismogram program, Anivec™. This program determines the vector components of displacement as a function of time and distance from a point source directed along any of three coordinate directions. The software implements the effective medium theory in the long wavelength limit in each layer of a layer stack over a half-space. Each layer is allowed to have separate anisotropic parameters, but in this initial test, all layers are identical to create a half-space. The medium symmetry axis (vertical by default) is first rotated 90° to describe vertical fractures. Fracture densities of 0% (unfractured), 1% and 10% fractures are examined. Input parameters used to calculate effective elastic coefficient matrices are shown in Table B.1. The effective elastic coefficient matrices calculated for the half-space model are shown in Table B.12.

Table B.1 Input parameters used to calculate the effective elastic coefficient matrices.

Layer	**P-wave Velocity (V_p) (m/s)**	**S-wave Velocity (V_s) (m/s)**	**Lithologic Density (ρ) (kg/m^3)**	**Fracture Density (%)**	**Saturation**
1	5767	3183	2650	0, 1, & 10	Unsaturated & Saturated

Table B.2 Input parameters used to plot the synthetic seismic data.

Layer	**Effective Elastic Coefficient (*C*) Matrix (10^9 N/m^2)**	**Lithologic Density (ρ) (kg/m^3)**	**Thickness (m)**
1	$\begin{bmatrix} 88.134 & 34.438 & 34.438 & 0.000 & 0.000 & 0.000 \\ 34.438 & 88.134 & 34.438 & 0.000 & 0.000 & 0.000 \\ 34.438 & 34.438 & 88.134 & 0.000 & 0.000 & 0.000 \\ 0.000 & 0.000 & 0.000 & 26.848 & 0.000 & 0.000 \\ 0.000 & 0.000 & 0.000 & 0.000 & 26.848 & 0.000 \\ 0.000 & 0.000 & 0.000 & 0.000 & 0.000 & 26.848 \end{bmatrix}$	2650	Half-space (infinite)

Synthetic seismograms are generated from these parameters after selecting parameters for the calculation, including source-receiver offset, trace spacing, frequency range, and phase velocity range. Anivec™ uses frequency-wave number integration as described by Mallick and Frazer (1990). Like other reflectivity modeling programs, Anivec™ calculates plane-wave reflection coefficients for single frequency-single wavenumber plane waves. In a general layered material, these are dependent on angle of incidence and wavelength (or frequency) of plane waves, though not in the case of a half-space in the long-wavelength limit. Plane waves are added together to form spherical waves associated with a point source. Anivec™ accommodates anisotropy by using more complex boundary conditions than traditional reflectivity modeling programs. The input parameters for the unfractured medium are shown in Table B.2. Other parameters used in the program are shown in Table B.3.

Table B.3 Other parameters used in the Anivec™ program.

Frequency Range (Hz)	5-300
Sampling Rate (s)	0.001
Number of Wavenumbers	900
Minimum Phase Velocity (m/s)	750
Offset Range (m)	5-300
Receiver Spacing (m)	5

To demonstrate the proper functionality of Anivec™ and choice of input parameters, theoretical seismograms for a vertical point source on an elastic half-space (originally determined by Lamb, 1904) can be used for comparison. Lamb's solution demonstrated the relative amplitudes and nature of P, S, and Rayleigh waves. The P wave is the first arrival, a smaller amplitude S wave arrives later and precedes the Rayleigh wave, which has the largest amplitude. Some numerical solutions for Lamb's problem have been published (Mooney, 1974) and Figure B.1 shows an example.

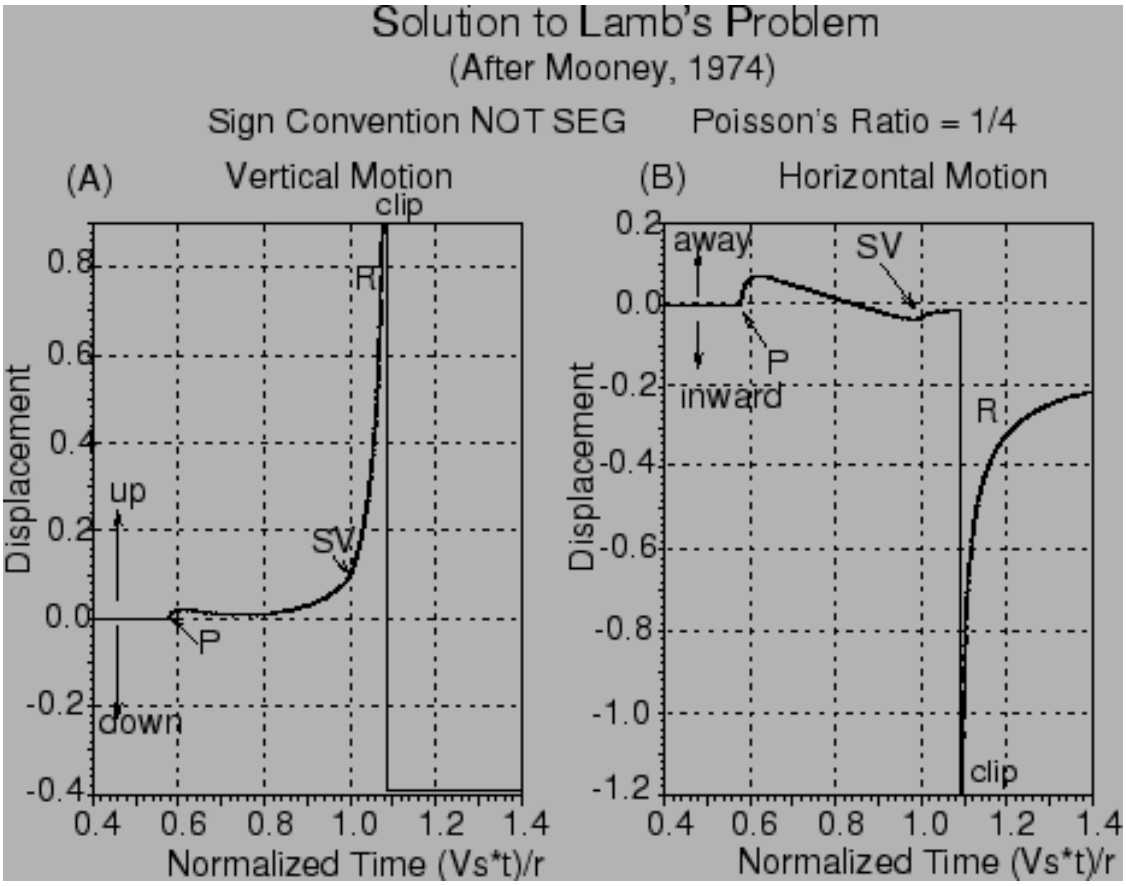

Figure B.1 Examples of numerical solutions for Lamb's problem.

Vertical source seismic traces predicted by Anivec™ for a homogeneous, unfractured half-space are shown in Figure B.2 at an offset of 300 m. Figure B.2 was constructed using input parameters from Table B.1, corresponding to a Poisson's ratio (unfractured material) of 0.28. Part a) is the vertical source, vertical receiver component. Part b) is the vertical source, inline (horizontal) component. The P wave arrival is at about 0.052 s, the S wave arrives at 0.94 and is precursor to the large amplitude Rayleigh wave that dominates the signal. The Rayleigh wave shows opposite polarity for the vertical and inline receiver components in Figure B.2, consistent with Figure B.1. Details of the seismogram waveforms are not directly comparable because the Lamb solution

employs a step-function source. To select the input parameters, the number of wavenumbers was set at 300 and increased in increments of 300 until no further changes were evident at 900. The frequency and offset ranges were set to be similar to observed seismograms. A Q value of 100 was chosen as representative of sedimentary rocks.

(a)

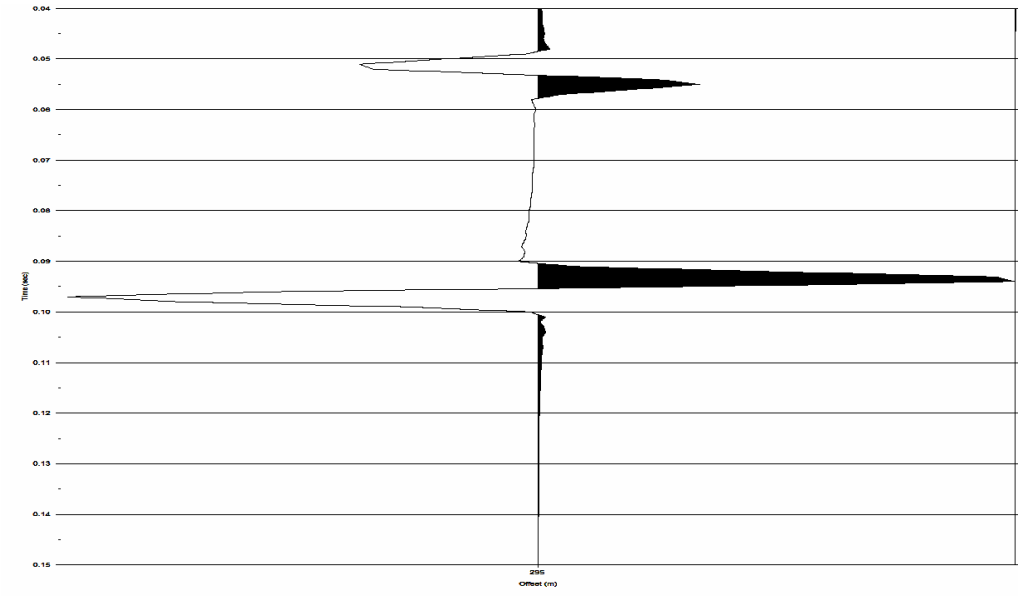

(b)

Figure B.2 The seismic trace for a homogeneous, unfractured half-space with a Poisson's ratio of 0.28. a) vertical source, vertical receiver component. b) vertical source, inline horizontal receiver component. The x-axis is time from 0 ms to 0.15 ms in 0.01 ms increments. The y-axis is the offset of 300 m.

Appendix C: Details of Data Processing of Fracture Pseudo-Surface

To perceive the fracture plane orientation precisely, surface elevation effects must be taken into account. Relative surface elevation data were collected over the survey area using a Total Station. The spacing of surface elevation points was 0.5 m in both across-slope and down-slope directions. Surface elevation data were plotted using Surfer (Golden Software, Inc). A 3D surface of the relative ground surface elevation was created in Surfer by interpolating z-coordinate values at x-y locations between input coordinates. A simple kriging algorithm was used to calculate statistically unbiased z-coordinate values from the input data values.

First breaks, first deflection in amplitude above background noise, were picked in Seismic Processing Workshop (SPW) for the ground surface reflection event and the fracture surface reflection event on all profiles from one of the background data sets. Trace number (or offset) and two-way travel time for both the surface and fracture reflection are recorded providing x-z coordinates along the length of each across-slope profile. The location of the profile corresponds to the y-coordinate. Picks on down-slope profiles provide y-z coordinates and profile locations provide x-coordinates. XYZ-coordinates were plot in Surfer to obtain a 3D surface for both the ground surface reflection and the fracture reflection.

For each x-y coordinate, the surface reflection time picked in SPW was set equal to the relative surface elevation calculated in meters from the Total Station data. The surface reflection time was subtracted from the fracture reflection time for each profile for each trace number. This difference in travel time was converted to distance using an estimated velocity of granite of 0.12 m/ns, which is within the range obtained by Davis and Annan (1989) and Reynolds (1997). This distance is the depth to the fracture below

the ground surface. A 3D surface of the fracture plane was created in Surfer by plotting z-coordinates at surface elevations minus calculated depths. This accounts for effects of surface elevation and displays the fracture orientation accurately.

Appendix D: Details of Channel Geometry Data Processing

Processing GPR data for channel geometry was done using Matlab by The Mathworks, Inc. As with processing of GPR profiles, this required resampling of original data to give each profile the same number of traces. Resampling assigns each trace to a particular spatial location in the across-slope direction. All profiles were converted to 5000 traces by linearly remapping trace numbers so the last trace in a profile is trace 5000. If fewer than 5000 traces were present in a profile, gaps were filled by averaging traces immediately before and after the gap. If more than 5000 traces were present in a profile, two traces were averaged to occupy one trace location. Next, the average value along the length of each trace in time was removed so the mean amplitude is about zero.

Data from the background GPR surveys were compared with surveys during liquid injection. Background surveys were averaged to obtain the average background GPR response for the site. Close inspection of GPR profiles reveals slight variations in arrival times of ground surface reflections due to variations in instrument location or other effects. Arrival times must be aligned to average the two data sets. Ground surface reflection arrival times were aligned by correlating the two background surveys over the ground surface reflection event. Each trace in the first background survey was correlated with the corresponding trace in the second background survey. Next, an average background data set was created from the two background surveys by averaging the two corresponding traces from each survey. Figure D.1 through Figure D.3 show traces from background surveys BG1 and BG2 before alignment, after alignment, and after averaging (Avg BG), respectively. These traces are from location (4300, 5424) in the survey area. The ground surface reflection event is the first event and occurs around 2 ns. The portions

of the trace outside the ground surface reflection event and the fracture reflection event are considered noise.

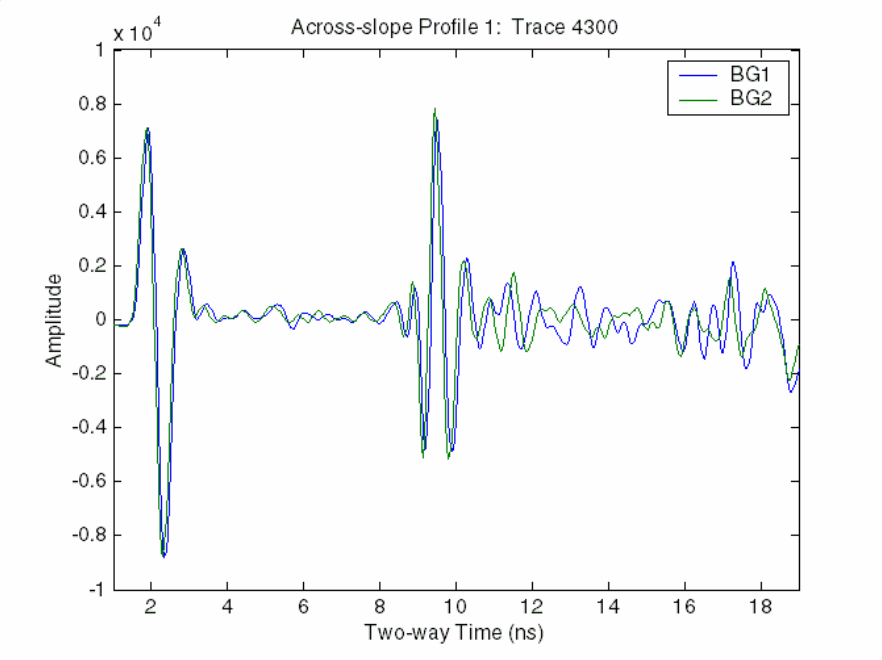

Figure D.1 An example of traces from the background surveys, BG1 and BG2, before ground surface reflection event arrival time alignment.

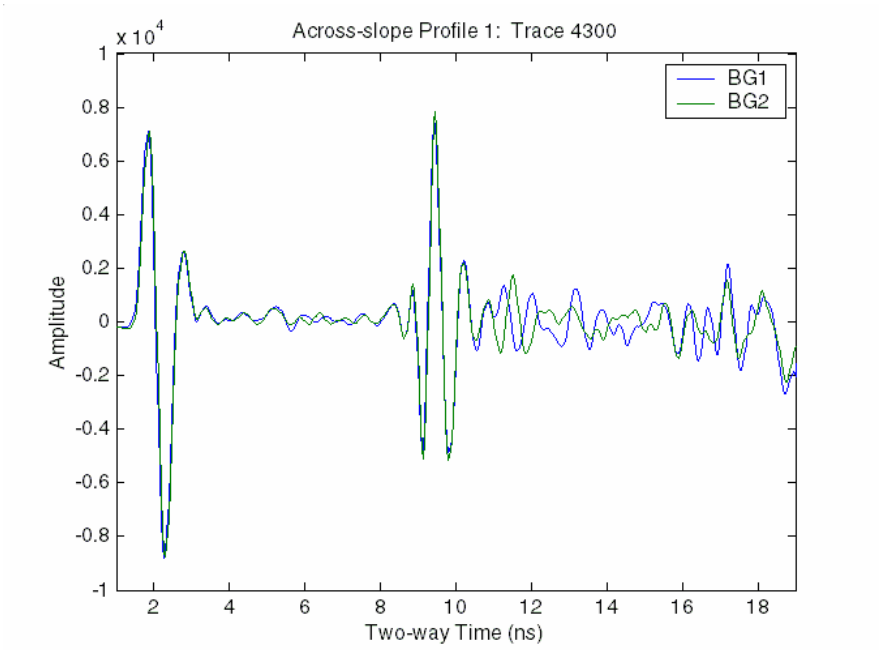

Figure D.2 An example of traces from the background surveys, BG1 and BG2, after ground surface reflection event arrival time alignment.

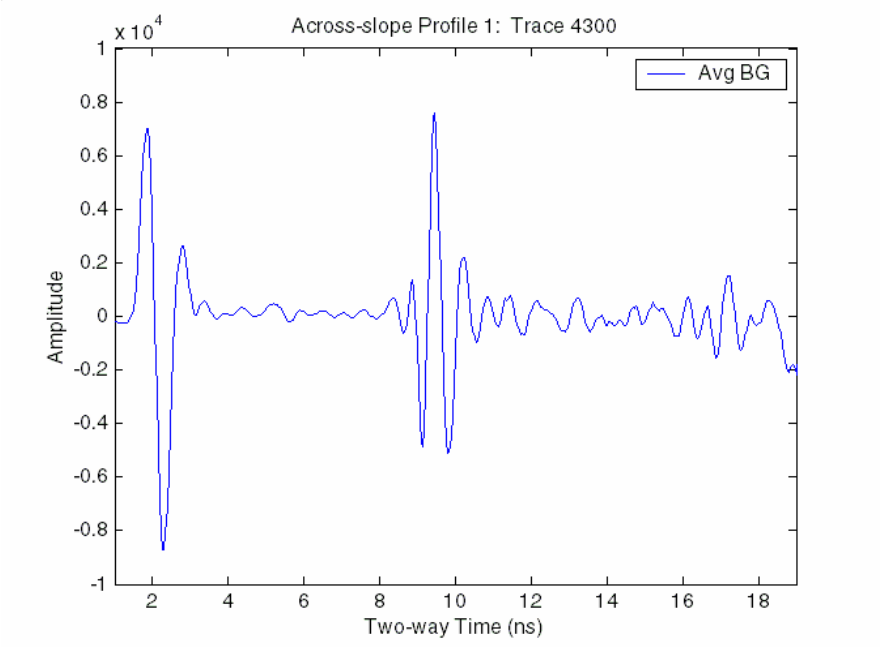

Figure D.3 An example of traces from the background surveys, BG1 and BG2, after averaging the two background GPR surveys, Avg BG.

Variations in ground surface reflection arrival times may cause misinterpretation of signal response among different GPR surveys. Therefore, as with aligning the background surveys, arrival times for the remaining surveys were aligned to that of the average background data set. Figure D.4 shows traces from all GPR surveys a) before alignment, and b) after alignment. These traces are from location (100, 4000) in the survey area. The ground surface reflection event is the first event at around 2 ns. In the legend, Avg BG is a trace from the average of the two background surveys, Water is a trace from the water only survey, Low Salinity is a trace from the water and low salinity tracer survey, and High Salinity is a trace from the water and high salinity tracer survey.

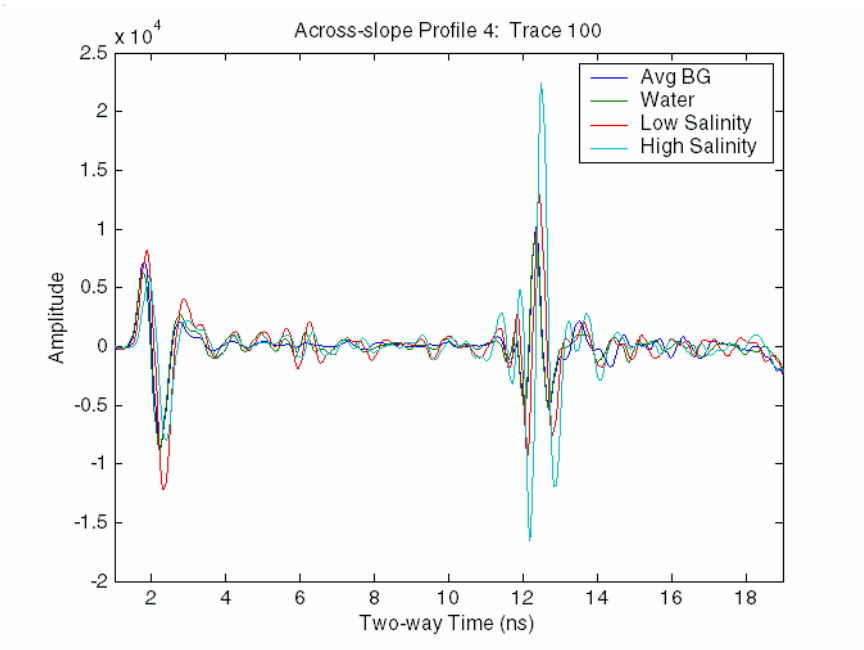

(a)

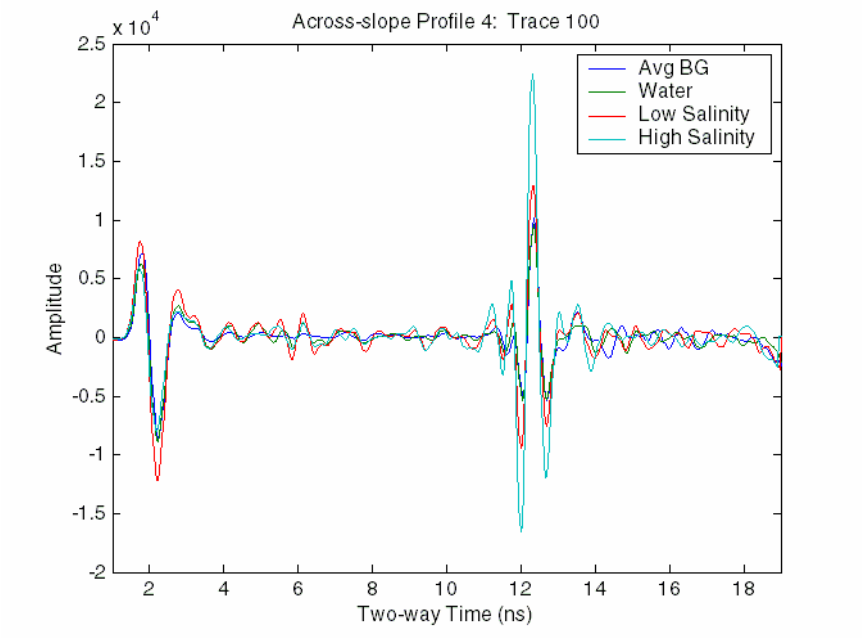

(b)

Figure D.4 An example of traces from all GPR surveys a) before ground surface reflection arrival time alignment, and b) after alignment.

Data from each survey were re-correlated using aligned ground surface reflection arrival times. This second correlation was over the fracture reflection event to determine the degree to which a trace from a fluid injection survey correlates with the corresponding tracer in the average background data set. As shown in the results of the numerical modeling experiment, amplitude is not a diagnostic factor of fluid type for the aperture range expected at this field site. Therefore, correlation between GPR surveys was used to identify changes in signal response from one survey to another. Signal changes should be due to changes in fluid in the fracture since all other factors remain constant. Traces that correlated well with the background data were assumed to record the GPR signal response equal to the background response, or the response due to air filling the fracture. Traces that did not correlate well to the background data were assumed to record signal response due to the presence of liquid (water, low concentration saline tracer, or high concentration saline tracer) being injected at the time the survey was acquired. Therefore, traces with poor correlation to the corresponding traces from the average background data set relate to locations where injected liquid was present in the fracture.

Figure D.5 shows traces from all GPR surveys that correlate well with the average background data set. These traces are from locations: a) (1000, 5424) and b) (600, 0). The fracture reflection event is the second event and occurs around a) 14 ns and b) 3 ns. Figure D.6 shows traces from all GPR surveys that have poor correlation with the average background data set. These traces are from locations: a) (3761, 5424) and b) (3100, 0). The fracture reflection event is the second event and occurs around a) 10 ns and b) 4 ns. In the legend, Avg BG is the average of the two background traces, Water is a trace from the water only survey, Low Salinity is a trace from the water and low salinity tracer survey, and High Salinity is a trace from the water and high salinity tracer survey.

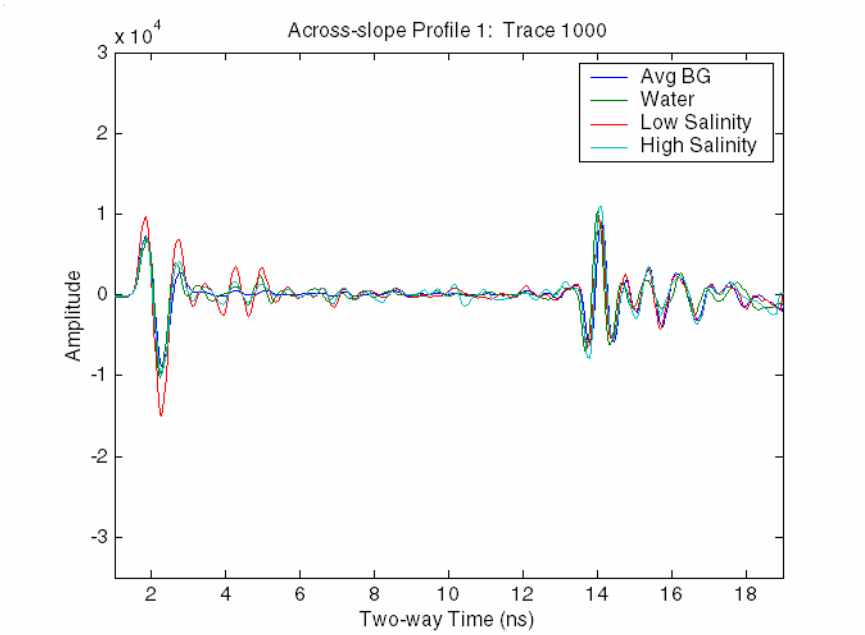

(a)

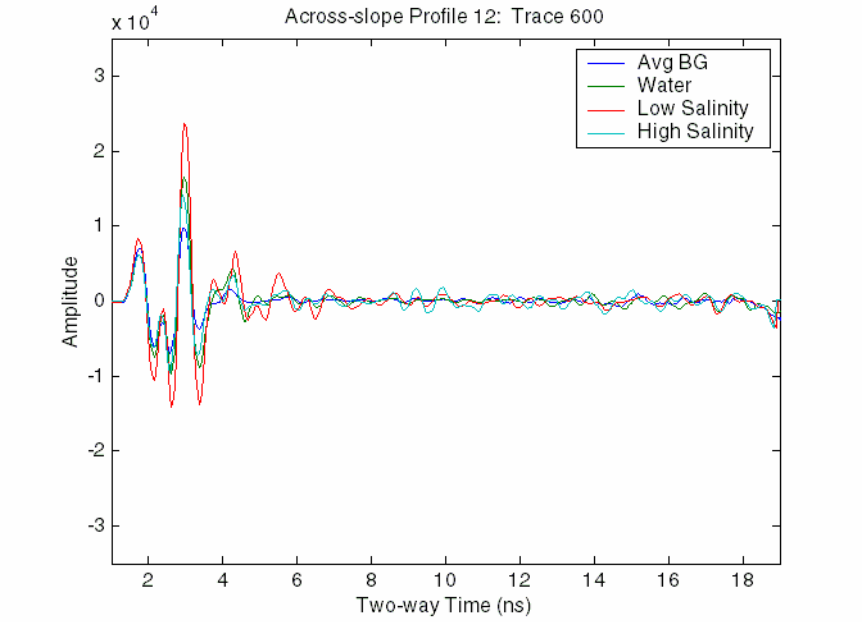

(b)

Figure D.5 Plots of traces from all GPR surveys that correlate well with the average background data set. These traces are from locations: a) (1000, 5424) and b) (600, 0).

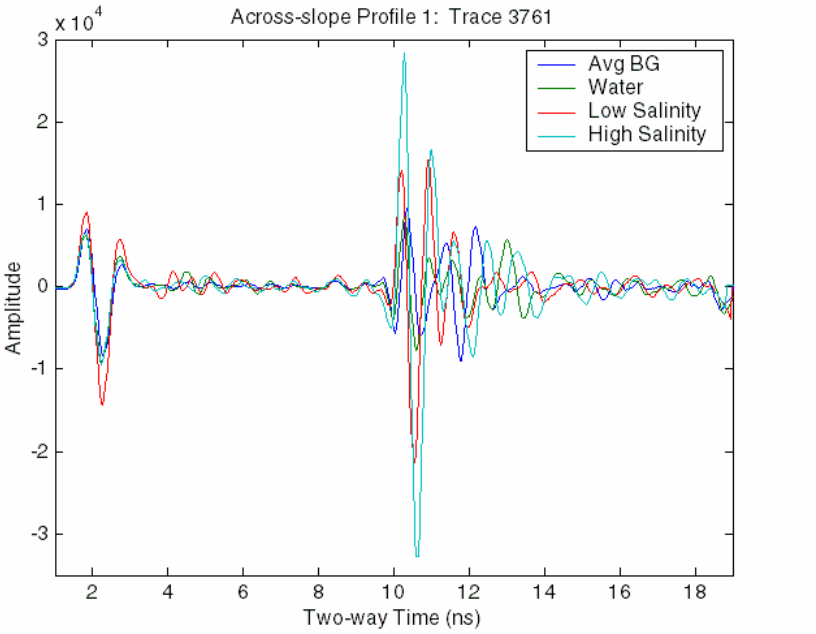

(a)

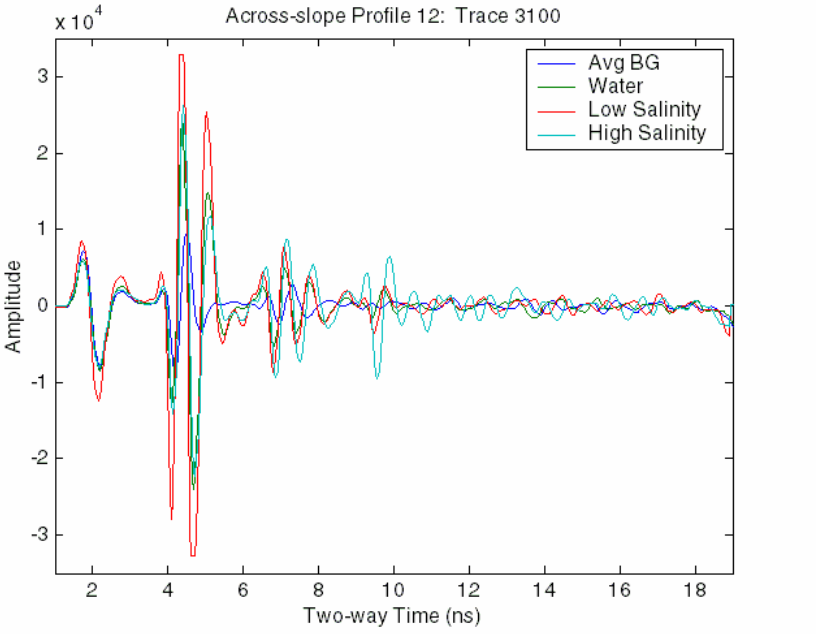

(b)

Figure D.6 Plots of traces from all GPR surveys that correlate poorly with the average background data set. These traces are from locations: a) (3761, 5424) and b) (3100, 0).

Figure D.7 shows the absolute value of correlation coefficients for a couple of the across-slope profiles. The correlations between the two background surveys are almost 1 for all profiles except Profile 12. Background correlations for Profiles 1 through 11 indicate good data repeatability. Profile 12 may not be well correlated due to a greater ground surface slope at this end of the survey area. Data acquisition was more difficult on Profile 12 and variations in antenna location and orientation due slight antenna slippage may have occurred. Results from Profile 12 may not be accurate. Poor correlations in Figure D.7a) indicate locations where fluid is present in the fracture.

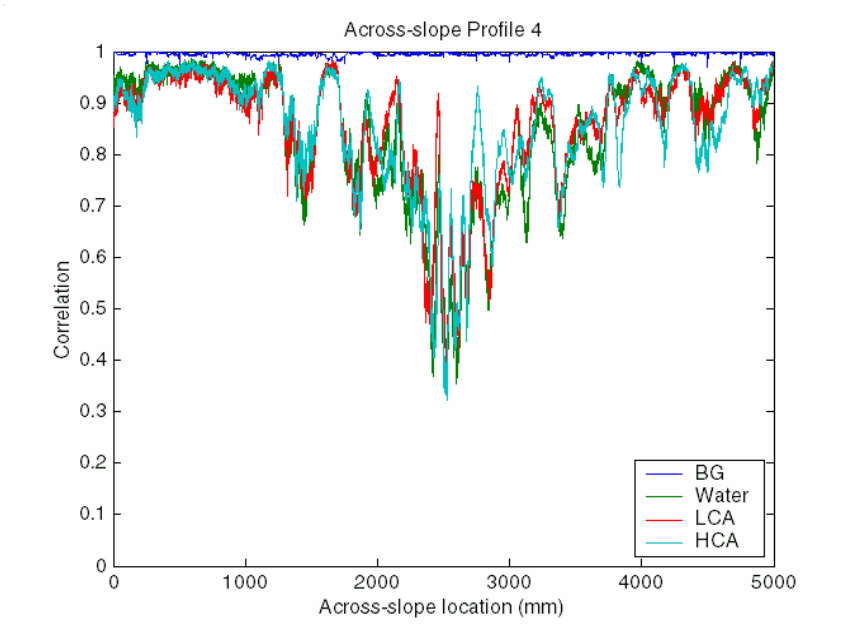

(a)

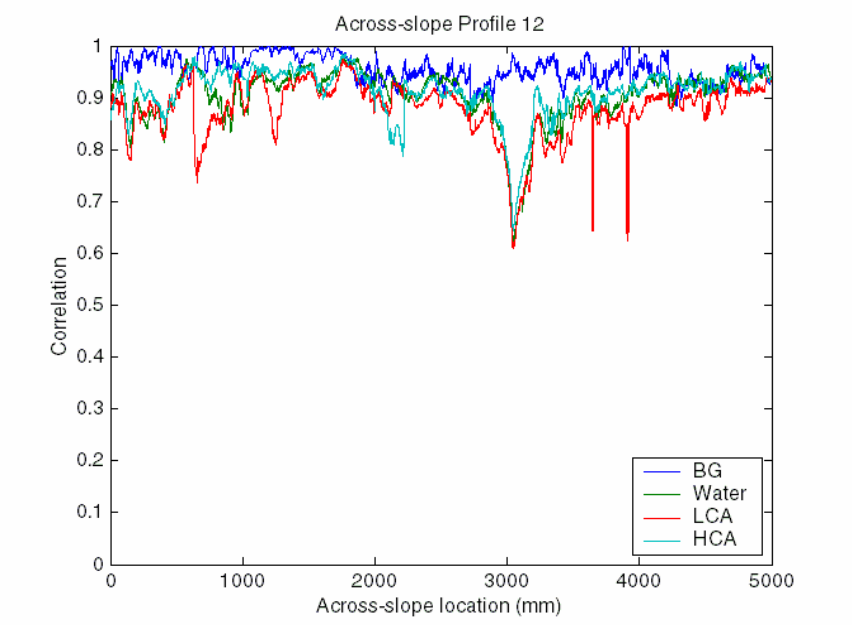

(b)

Figure D.7 Plots of correlation coefficients for (a) Profile 4 and (b) Profile 12.

To determine the geometry of the tracer within the water channels, the low and high salinity data sets were correlated with the water only data set. Traces that correlated well with the water only survey recorded the GPR signal response equal to the response due to liquid in the fracture. Traces that did not correlate well to the water only survey correspond to the signal response to the tracer. These poor correlations were used to plot the channeling of low salinity and high salinity tracer within the water channels. Traces of good and poor correlation between tracer and water are shown in Figure D.8 and Figure D.9, respectively. Good correlation between traces from the water only survey and traces from the water and tracer surveys indicate the presence of water in each survey. Poor correlation between traces from the water only survey and traces from the water and tracer surveys indicate the presence of tracer in the tracer survey. The traces in Figure D.8 and Figure D.9 are enlarged to show details of the fracture reflection event. The ground surface reflection event is not shown.

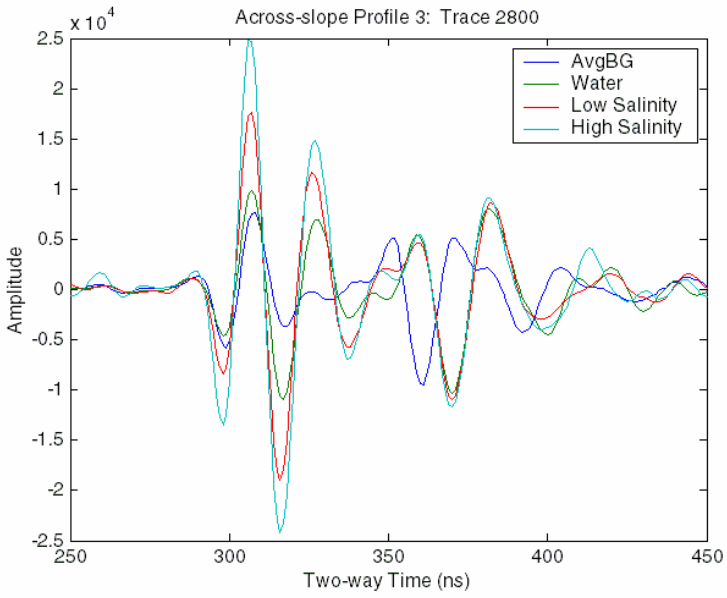

(a)

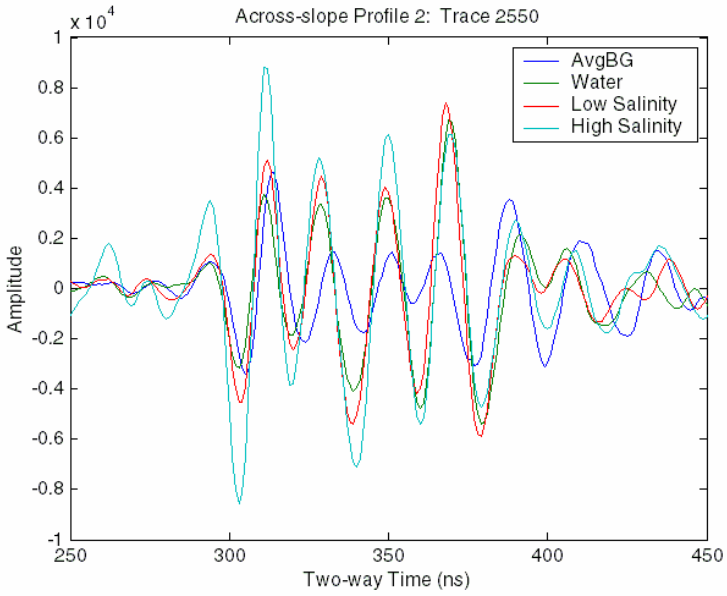

(b)

Figure D.8 Plots of traces from water only, low salinity tracer, and high salinity tracer surveys for good correlation to water only survey but poor correlation to dry background survey indicating the fluid signal present is from water. (a) Profile 3, trace location 2800 and (b) Profile 2, trace location 2550.

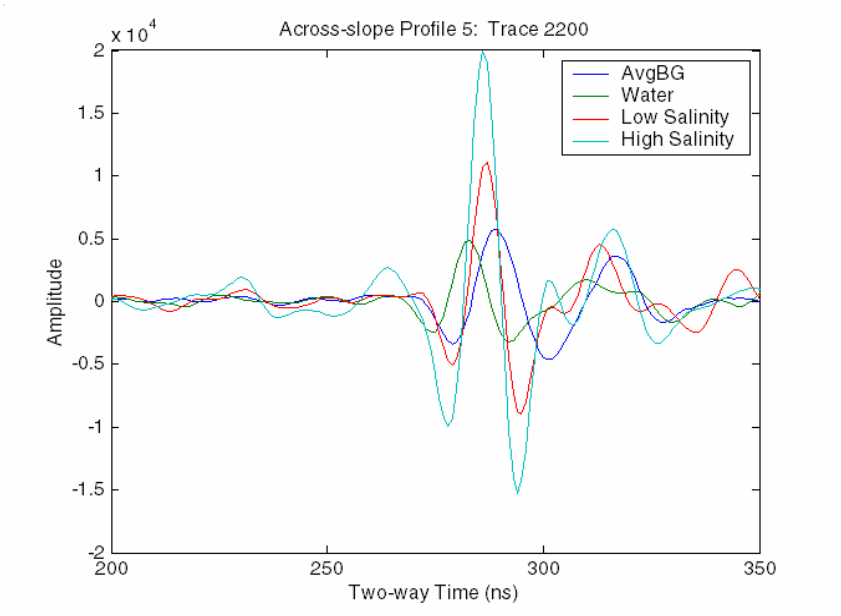

(a)

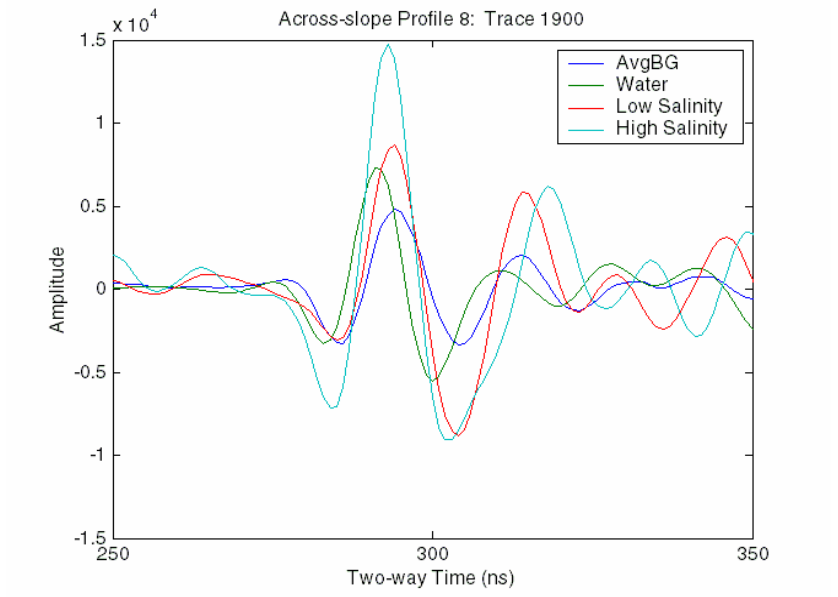

(b)

Figure D.9 Plots of traces from water only, low salinity tracer, and high salinity tracer surveys for a) and b) poor correlation to both water only and dry background surveys indicating the fluid signal present is from the tracer. (a) Profile 5, trace location 2200 and (b) Profile 8, trace location 1900.

References

Alford, R. M., 1986, Shear data in the presence of azimuthal anisotropy: SEG International Exposition and Fifty-Sixth Annual Meeting, p. 476-479.

Annan, A. P., 2005, Ground-penetrating radar, in D. K. Butler, ed., Near-Surface Geophysics, v. 13: Tulsa, Society of Exploration Geophysicists, p. 357-438.

Ass'ad, J. M., R. H. Tatham, and J. A. McDonald, 1992, A physical model study of microcrack-induced anisotropy: Geophysics, v. 57, p. 1562-1570.

B.S.E.A.C.D., 2002, Summary of groundwater dye tracing studies (1996-2002), Barton Springs segment of the Edwards Aquifer, Texas, Barton Springs/Edwards Aquifer Conservation District, Austin, Texas.

Bakulin, A., V. Grechka, and I. Tsvankin, 2000, Estimation of fracture parameters from reflection seismic data - Part I: HTI model due to a single fracture set: Geophysics, v. 65, p. 1788-1802.

Bamford, D., 1977, Pn velocity anisotropy in a continental upper mantal: Geophysical Journal of the Royal Astronomical Society, v. 49, p. 29-48.

Bamford, D., and K. R. Nunn, 1979, In situ seismic measurements of crack anisotropy in the carboniferous limestone of Northwestern England: Geophysical Prospecting, v. 27, p. 322-338.

Beaty, K. S., and D. R. Schmitt, 2003, Case History: Repeatability of multimode Rayleigh-wave dispersion studies: Geophysics, v. 68, p. 782-790.

Beckham, W. E., 1996, Seismic anisotropy and natural fractures from VSP and borehole sonic tools – A field study: Geophysics, v. 61, p. 456-466.

Bradford, J. H., 2002, Depth characterization of shallow aquifers with seismic reflection, Part I – The failure of NMO velocity analysis and quantitative error prediction: Geophysics, v. 67, p. 89-97.

Cheadle, S. P., R. J. Brown, and D. C. Lawton, 1991, Orthorhombic anisotropy: A physical modeling study: Geophysics, v. 56, p. 1603-1613.

Corrigan, D., J. D. Justice, and E. B. Neitzel, 1986, Estimate of shear-wave anisotropy using multicomponent seismic data: 56th Annual International Meeting, Society of Exploration Geophysicists, Expanded Abstracts, p. 389-391.

Daley, P. F., and F. Hron, 1977, Reflection and Transmission Coefficients for Transversely Isotropic Media: Bulletin of the Seismological Society of America, v. 67, p. 661-675.

Daniels, J. J., R. Roberts, and M. Vendl, 1995, Ground penetrating radar for the detection of liquid contaminants: Journal of Applied Geophysics, v. 33, p. 195-207.

Davis, J. L., and A. P. Annan, 1989, Ground penetrating radar for high-resolution mapping of soil and rock stratigraphy: Geophysical Prospecting, v. 37, p. 531-551.

Davis, T. L., and C. Lewis, 1990, Reservoir characterization by 3-D, 3-C seismic imaging, Silo Field, Wyoming: Leading Edge, v. 9, p. 22-25.

Day-Lewis, F. D., J. W. Lane, J. M. Harris, and S. M. Gorelick, 2003, Time-lapse imaging of saline-tracer transport in fractured rock using difference-attenuation radar tomography: Water Resources Research, v. 39, p. 1290-1303.

Domenico, S. N., 1983, Sandstone and limestone porosity determination from shear and compressional wave velocity: Bulletin of the Australian Society of Exploration Geophysicists, v. 14, p. 81-90.

Domenico, S. N., 1984, Rock lithology and porosity determination from shear and compressional wave velocity: Geophysics, v. 49, p. 1188-1195.

Douma, J., H. D. Rooijen, and F. Schokking, 1990, Anisotropy detected in shallow clays using shear-wave splitting in a VSP survey: Geophysical Prospecting, v. 38, p. 983-998.

Ewing, M. W., W. S. Jardetsky, and F. Press, 1957, Elastic Waves in Layered Media: International Series in the Earth Sciences, (equation 4-202).

Gardner, L. W., 1939, An areal plan of mapping subsurface structure by refraction shooting: Geophysics, v. 4, p. 247-259.

Garner, T. T., 2007, Characterization of Transport Properties in Granitic Fractures with Skins, Ph.D. Thesis, The University of Texas at Austin.

Gledhill, K. R., 1993a, Shear waves recorded on close-spaced seismographs: I. Shear-wave splitting results: Canadian Journal of Exploration Geophysics, v. 29, p. 285-298.

Gledhill, K. R., 1993b, Shear waves recorded on close-spaced seismographs: II. The complex anisotropic structure of the Wellington Peninsula, New Zealand: Canadian Journal of Exploration Geophysics, v. 29, p. 299-314.

Google, 2005, Aerial photograph of Stoneledge Quarry. www.maps.google.com.

Google, 2006, Map: Location of Buchanan Dam relative to Austin, Texas. www.maps.google.com.

Graham, G., and S. Crampin, 1993, Shear-wave splitting from regional earthquakes in Turkey: Canadian Journal of Exploration Geophysics, v. 29, p. 371-379.

Grant, F. S., and G. F. West, 1965, Interpretation Theory in Applied Geophysics: Toronto, McGraw-Hill Education, 582 p.

Hauwert, N. M., 2004, Personal communication.

Hill, R. T., and T. W. Vaughan, 1896, The Geology of the Edwards Plateau and Rio Grande Plain adjacent to Austin and San Antonio, Texas, with references to the occurrence of underground waters, US Geological Survey 18th Annual Report, pt. 2-B, p. 321.

Hollender, F., and S. Tillard, 1998, Modeling ground-penetrating radar wave propagation and reflection with the Jonscher parameterization: Geophysics, v. 63, p. 1933-1942.

Hudson, J. A., 1980, Overall properties of a cracked solid: Mathematical Proceedings of the Cambridge Philosophical Society, p. 371-384.

Hudson, J. A., 1981, Wave speeds and attenuation of elastic waves in material containing cracks: Geophysical Journal of the Royal Astronomical Society, v. 64, p. 133-150.

Hudson, J. A., E. Liu, and S. Crampin, 1996, The mechanical properties of materials with interconnected cracks and pores: Geophysical Journal International, v. 124, p. 105-112.

Keller, G. V., 1987, Rock and mineral properties, in M. N. Nabighian, ed., Electromagnetic methods in applied geophysics - Theory, v. 1, SEG, p. 131-311.

Kolb, R., Alan, 1981, Geology of the Signal Hill Quadrangle, Hays and Travis Counties, Texas, Ph.D. Thesis, University of Texas, Austin.

Krasny, J., and J. M. Sharp, 2007, Hydrology of fractured rocks from particular fractures to regional approaches: State-of-the-art and future challenges (preface, 30p.), in J. Krasny, and J. M. Sharp, eds., Groundwater in Fractured Rock, IAH Selected Papers on Hydrology, v. 9, Taylor & Francis, p. 665.

Lamb, H., 1904, On the propagation of tremors over the surface of an elastic solid: Philosophical Transactions of the Royal Society of London, Series A, v. 203, p. 1-42.

Lane, J. W., M. L. Buursink, F. P. Haeni, and R. J. Versteeg, 2000, Evaluation of ground-penetrating radar to detect free-phase hydrocarbons in fractured rocks - Results of numerical modeling and physical experiments: Ground Water, v. 38, p. 929-938.

Lane, J. W., D. L. Wright, and F. P. Haeni, 1999, Borehole radar tomography using saline tracer injections to image fluid flow in fractured rock: U.S. Geological Survey Toxic Substances Hydrology Program - Proceedings of the Technical Meeting, p. 747-756.

Lawton, D. C., 1990, A 9-component refraction seismic experiment: Canadian Journal of Exploration Geophysics, v. 26, p. 7-16.

Lewis, C., T. L. Davis, and C. Vuillermoz, 1991, Three-dimensional multicomponent imaging of reservoir heterogeneity, Silo Field, Wyoming: Geophysics, v. 56, p. 2048-2056.

Li, X.-Y., and M. C. Mueller, 1997, Case studies of multicomponent seismic data for fracture characterization: Austin Chalk examples: Carbonate Seismology, Society of Exploration Geophysicists, p. 337-372.

Li, X.-Y., M. C. Mueller, and S. Crampin, 1993, Case studies of shear-wave splitting in reflection surveys in South Texas: Canadian Journal of Exploration Geophysics, v. 29, p. 189-215.

Liu, Y., D. C. Booth, S. Crampin, R. Evans, and P. Leary, 1993a, Shear-wave polarizations and possible temporal variations in shear-wave splitting at Parkfield: Canadian Journal of Exploration Geophysics, v. 29, p. 380-390.

Liu, E., S. Crampin, J. H. Queen, and W. D. Rizer, 1993b, Velocity and attenuation anisotropy caused by microcracks and macrofractures in a multiazimuth reverse VSP: Canadian Journal of Exploration Geophysics, v. 29, p. 177-188.

Lynn, H. B., 1991, Field measurements of azimuthal anisotropy: First 60 meters, San Francisco Bay area, CA, and estimation of horizontal stresses' ratio from Vs1/Vs2: Geophysics, v. 56, p. 822-832.

Lynn, H. B., and L. A. Thomsen, 1990, Reflection shear-wave data collected near the principal axes of azimuthal anisotropy: Geophysics, v. 55, p. 147-156.

Mallick, S., and L. N. Frazer, 1990, Computation of synthetic seismograms for stratified azimuthally anisotropic media: Journal of Geophysical Research, v. 95, p. 8513-8526.

Martinez, A., and A. P. Byrnes, 2001, Modeling dielectric-constant values of geologic materials: An aid to ground-penetrating radar data collection and interpretation: Current Research in Earth Sciences, v. Bulletin 247, part 1, p. 1-16.

Mooney, H. M., 1974, Some numerical solutions for Lamb's problem: Bulletin of the Seismological Society of America, v. 64, n. 2, p. 473-491.

Mueller, M. C., 1991, Prediction of lateral variability in fracture intensity using multicomponent shear-wave surface seismic as a precursor to horizontal drilling in the Austin Chalk: Geophysical Journal International, v. 107, p. 409-415.

Mueller, M. C., 1992, Using shear waves to predict lateral variability in vertical fracture intensity: The Leading Edge, v. 11, p. 29-35.

Nur, A., and G. Simmons, 1969, Stress-induced velocity anisotropy in rock: An experimental study: Journal of Geophysical Research, v. 74, p. 6667-6674.

Ohanian, V., and W. E. Beckham, 1992, Depth-variant fracture orientation from multicomponent VSP data: 62nd Internat. Mtg., Expanded Abstracts, p. 177-180.

Potters, J. H. H. M., H. J. J. Groenendaal, S. J. Oates, J. H. Hake, and A. B. Kalden, 1999, The 3D shear experiment over the Natih field in Oman. Reservoir geology, data acquisition and anisotropy analysis: Geophysical Prospecting, v. 47, p. 637-662.

Pratt, R. G., W. J. McGaughey, and C. H. Chapman, 1993, Anisotropic velocity tomography: A case study in a near-surface rock mass: Geophysics, v. 58, p. 1748-1763.

Rai, C. S., and K. E. Hanson, 1988, Shear-wave velocity anisotropy in sedimentary rocks: A laboratory study: Geophysics, v. 53, p. 800-806.

Rathore, J. S., E. Fjaer, R. M. Holt, and L. Renlie, 1994, P- and S-wave anisotropy of a synthetic sandstone with controlled crack geometry: Geophysical Prospecting, v. 43, p. 711-728.

Reynolds, J. M., 1997, An introduction to applied and environmental geophysics: New York, John Wiley & Sons.

Rowlands, H. J., D. C. Booth, and J.-M. Chiu, 1993, Shear-wave splitting from microearthquakes in the New Madrid seismic zone: Canadian Journal of Exploration Geophysics, v. 29, p. 352-362.

Schoenberg, M., and J. Douma, 1988, Elastic wave propagation in media with parallel fractures and aligned cracks: Geophysical Prospecting, v. 36, p. 571-590.

Sensors & Software, 1992, Ground penetrating radar survey design, Mississauga, ON, Sensors & Software, Inc., p. 17.

Sharp, J. M., 1993, Fractured aquifers/reservoirs: approaches, problems and opportunities: Memoires of the XXIVth Congress of IAH, p. 23-38.

Sharp, J. M., 2003, A glossary of hydrogeological terms: Austin, Texas, Department of Geological Sciences, The University of Texas, 52 p.

Sheriff, R. E., 2002, Encyclopedic dictionary of applied geophysics, 4th ed., Society of Exploration Geophysicists, 429 p.

Sheriff, R. E., and L. P. Geldart, 1995, Theory of seismic waves: Exploration Seismology, 592 p.

Shuck, E. L., T. L. Davis, and R. D. Benson, 1996, Multicomponent 3-D characterization of a coalbed methane reservoir: Geophysics, v. 61, p. 315-330.

Talley, J., G. S. Baker, M. W. Becker, and N. Beyrle, 2005, Four dimensional mapping of tracer channelization in subhorizontal bedrock fractures using ground penetrating radar: Geophysical Research Letters, v. 32, p. L04401.

Tatham, R. H., M. D. Matthews, K. K. Sekharan, C. J. Wade, and L. M. Liro, 1992, A physical model study of shear-wave splitting and fracture intensity: Geophysics, v. 57, p. 647-652.

Tatham, R. H., and M. D. McCormack, 1991, Multicomponent Seismology in Petroleum Exploration, Society of Exploration Geophysicists, 13-40 and 74-84 p.

Thomsen, L., 1986, Weak elastic anisotropy: Geophysics, v. 51, p. 1954-1966.

Thomsen, L., 1988, Reflection seismology over azimuthally anisotropic media: Geophysics, v. 53, p. 304-313.

Thomsen, L., 1995, Elastic anisotropy due to aligned cracks in porous rock: Geophysical Prospecting, v. 43, p. 805-829.

Thomsen, L., 2002, Understanding Seismic Anisotropy in Exploration and Exploitation:

Tsoflias, G. P., T. Halihan, and J. M. J. Sharp, 2001, Monitoring pumping test response in a fractured aquifer using ground-penetrating radar: Water Resources Research, v. 37, p. 1221-1229.

Tsoflias, G. P., and A. Hoch, 2006, Investigating multi-polarization GPR wave transmission through thin layers: Implications for vertical fracture characterization: Geophysical Research Letters, v. 33, L20401.

Tsoflias, G. P., and J. M. J. Sharp, 1998, Three-dimensional hydrogeologic characterization of fractured carbonate aquifers using ground-penetrating radar: Transactions - Gulf Coast Association of Geological Societies, v. 48, p. 439-447.

Vernik, L., and X. Liu, 1997, Velocity anisotropy in shales: A petrophysical study: Geophysics, v. 62, p. 521-532.

Vlahovic, G., M. Elkibbi, and J. A. Rial, 2002, Shear-wave splitting and reservoir crack charaterization: the Coso geothermal field: Journal of Volcanology and Geothermal Research, v. 120, p. 123-140.

Ward, S. H., and G. W. Hohmann, 1987, Electromagnetic theory for geophysical applications, in M. N. Nabighian, ed., Electromagnetic methods in applied geophysics - Theory, v. 1, SEG, p. 131-311.

West, M., and W. Menke, 2001, Fluid-induced changes in shear velocity from surface waves, CD-ROM p.1-11: Annual Meeting SAGEEP.

Winterstein, D. F., and B. N. P. Paulsson, 1990, Velocity anisotropy in shale determined from crosshole seismic and vertical seismic profile data: Geophysics, v. 55, p. 470-479.

Xiong, Y., C. Yao, and P. Wang, 1993, The features of shear-wave splitting in Lulong, northern China, and its seismic implications: Canadian Journal of Exploration Geophysics, v. 29, p. 332-340.

Yao, C., P. Wang, Y. Lu, and Y. Chen, 1993, Interpretation of shear-wave splitting in Datong area, northern China: Canadian Journal of Exploration Geophysics, v. 29, p. 341-351.

Yao, C., and Y. Xiong, 1993, Shear-wave splitting from local earthquakes modeled by synthetic seismograms: Canadian Journal of Exploration Geophysics, v. 29, p. 324-331.

Vita

Nedra Danielle Bonal was born in Pasadena, Texas on September 14, 1975, the daughter of Rebecca Ann Alexander and Truman Ray Alexander. After completing her work at Oak Ridge High School, Conroe, Texas, in 1994, she attended classes at North Harris County Community College while working full-time. In August of 1997, she entered New Mexico Institute of Mining and Technology in Socorro, New Mexico where she received her Bachelor of Science in May of 2000. During the following years she was employed as a project geophysicist at Fugro South, Inc. in Houston, Texas. In January 2002, she entered the graduate program in the Department of Geological Sciences at The University of Texas at Austin.

Permanent Address: 2728 Tramway Circle NE, Albuquerque, New Mexico 87122

This dissertation was typed by the author.